

THE UNIVERSITY OF CALGARY

High Quality Factor Asymmetric-slope Band-pass Filters

by

Peyman Ahmadi

A THESIS

SUBMITTED TO THE FACULTY OF GRADUATE STUDIES IN PARTIAL  
FULFILLMENT OF THE REQUIREMENTS FOR THE DEGREE OF  
MASTER OF SCIENCE

DEPARTMENT OF ELECTRICAL AND COMPUTER ENGINEERING

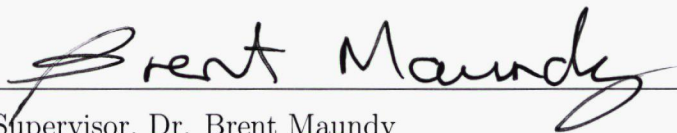
CALGARY, ALBERTA

AUGUST, 2011

© Peyman Ahmadi 2011

**THE UNIVERSITY OF CALGARY**  
**FACULTY OF GRADUATE STUDIES**

The undersigned certify that they have read, and recommend to the Faculty of Graduate Studies for acceptance, a thesis entitled "High Quality Factor Asymmetric-slope Band-pass Filters" submitted by Peyman Ahmadi in partial fulfillment of the requirements for the degree of Master of Science.



Supervisor, Dr. Brent Maundy  
Department of Electrical and Computer Engineering



Co-supervisor, Dr. Leonid Belostotski  
Department of Electrical and Computer Engineering



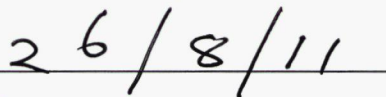
Dr. Ed Nowicki  
Department of Electrical and Computer Engineering



Dr. Svetlana Yanushkevich  
Department of Electrical and Computer Engineering



Dr. Jeroen Stil  
Department of Physics and Astronomy



Date

## ABSTRACT

This thesis presents new techniques for designing continuous-time band-pass filters with high quality factors and asymmetric slope characteristics based on the concept of fractional-order filters. The techniques are centered around the realization of non-conventional transfer functions which include a non-integer-order Laplacian operator  $s^\alpha$ ;  $0 < \alpha < 1$ . Two types of asymmetric-slope band-pass filters are presented and the symmetry in the relationship of one transfer function to the next is highlighted. Possible circuit realizations for second-order and fourth order asymmetric band-pass filters; based on Frequency Dependent Negative Resistor, inductor and Multiple Amplifier Biquad are given and verified using SPICE and experimentally for the proposed transfer functions. In addition, a Field Programmable Analog Array realization is also tested and verified.

## ACKNOWLEDGEMENTS

This thesis is a result of support and guidance of many people. I thank first and most ever, my supervisor, Dr. Brent Maundy for introducing this field to me and giving me the chance to complete my research in this field. I would also like to thank my co-supervisor, Dr. Leonid Belostotski for both his support and valuable guidance which helped me a lot during my research. I thank them for all their time and encouragement.

My thanks also to Dr. Ahmed Elwakil from department of Electrical and Computer Engineering at the University of Sharjah for his guidance and reviewing my publications.

I would also like to thank Dr. Roghoyeh Salmeh who supported my decision and helped me to continue my graduate studies at the University of Calgary.

Last but not the least, I would like to give my heartfelt thanks to my parents and sister, Pantea who kindly supported and encouraged me to continue my graduate studies. Thank you for standing beside me during all parts of my life.

For my mother

Thank you.

## TABLE OF CONTENTS

<b>Abstract</b>	<b>ii</b>
<b>Acknowledgments</b>	<b>iii</b>
<b>Dedication</b>	<b>iv</b>
<b>Table of Contents</b>	<b>v</b>
<b>List of Tables</b>	<b>viii</b>
<b>List of Figures</b>	<b>ix</b>
<b>List of Abbreviations</b>	<b>xvii</b>
<b>1 Introduction</b>	<b>1</b>
1.1 Integer-Order Filters . . . . .	1
1.2 Band-pass Filters . . . . .	2
1.3 Fractional Capacitor . . . . .	4
1.4 Fractional-Order Filters . . . . .	6
1.5 High Quality Factor Asymmetric-Slope Band-Pass Filters . . . . .	7
1.6 Thesis layout . . . . .	9
<b>2 Asymmetric-Slope Band-pass Filters</b>	<b>11</b>
2.1 Passive Prototypes . . . . .	11
2.1.1 Type I FDNR-Based Asymmetric-Slope Band-pass Filter . . .	15
2.1.2 Type II Inductor-Based Asymmetric-Slope Band-pass Filter .	21
2.1.3 Type I Inductor-Based Asymmetric-Slope Band-Pass Filter . .	25
2.1.4 Type II FDNR-Based Asymmetric-Slope Band-Pass Filter . .	27
2.2 Possible Designs . . . . .	29
2.2.1 Type I Filter Realizations . . . . .	29
2.2.2 Type II Filter Realizations . . . . .	32

<b>3</b>	<b>Simulation and Experimental Results</b>	<b>36</b>
3.1	Using Discrete Components . . . . .	36
3.1.1	Type I Filters . . . . .	36
3.1.2	Type II Filters . . . . .	39
3.2	FPAA realization . . . . .	44
3.2.1	Field Programmable Analog Array Implementation . . . . .	44
3.2.2	FPAA Realization of Non-Integer Laplacian Operator . . . . .	45
3.2.3	FPAA Realization of Type I Band-pass Filter . . . . .	46
3.2.4	FPAA Realization of Type II Band-pass Filter . . . . .	50
<b>4</b>	<b>Non-Ideal Effects</b>	<b>53</b>
4.1	Lossy Elements . . . . .	53
4.1.1	Type I FDNR-Based Circuit . . . . .	53
4.1.2	Type I Inductor-Based Circuit . . . . .	54
4.1.3	Type II Inductor-Based Circuit . . . . .	56
4.1.4	Type II FDNR-Based Circuit . . . . .	57
4.1.5	The Non-ideal Fractional Capacitor . . . . .	59
4.2	Finite Gain Bandwidth Product . . . . .	60
4.2.1	Type I FDNR-Based Circuit . . . . .	60
4.2.2	Type I MAB-Based Circuit . . . . .	62
4.2.3	Type I Inductor-based Circuit . . . . .	62
4.2.4	Type II Inductor-Based Circuit . . . . .	65
4.2.5	Type II MAB-Based Circuit . . . . .	66
4.3	Voltage and Current Tracking Errors . . . . .	70
4.3.1	Type II FDNR-Based Circuit . . . . .	70
<b>5</b>	<b>Higher-Order Asymmetric-Slope Band-Pass Filters</b>	<b>73</b>
5.1	Higher-Order Normal Band-pass Filters . . . . .	73
5.2	Asymmetric-Slope Band-pass Passive Prototypes . . . . .	75
5.2.1	Type I Asymmetric-Slope Band-pass Passive Prototypes . . . . .	76
5.2.2	Type II Asymmetric-Slope Band-pass Passive Prototypes . . . . .	79
5.3	Fourth-Order Asymmetric-Slope Band-pass Filter . . . . .	82
5.3.1	Fourth-Order Type I FDNR-Based Filter . . . . .	82
5.3.1.1	Passive Prototype . . . . .	82
5.3.1.2	Simulation and Experimental Results . . . . .	84
5.3.2	Fourth Order Type I inductor-Based Filter . . . . .	88
5.3.2.1	Passive Prototype . . . . .	88

5.3.2.2	Simulation and Experimental Results . . . . .	89
5.3.3	Fourth Order Type II Inductor-Based Filter . . . . .	91
5.3.3.1	Passive Prototype . . . . .	91
5.3.3.2	Simulation and Experimental Results . . . . .	94
5.3.4	Fourth Order Type II FDNR-based Filter . . . . .	97
5.3.4.1	Passive Prototype . . . . .	97
5.3.4.2	Simulation and Experimental Results . . . . .	99
<b>6</b>	<b>Conclusions and future work</b>	<b>102</b>
6.1	Conclusion . . . . .	102
6.2	Contribution . . . . .	103
6.3	Future Work . . . . .	104
	<b>BIBLIOGRAPHY</b>	<b>106</b>
<b>A</b>	<b>Approximated Fractional Capacitor Realization</b>	<b>113</b>
<b>B</b>	<b>Alternative Second-order Type II Inductor-based Circuit</b>	<b>121</b>
<b>C</b>	<b>Percentage Variability of Center Frequency and Quality Factor for Type I FDNR-Based Filter</b>	<b>124</b>
<b>D</b>	<b>Non-ideal Transfer Function of Type I MAB-based Circuit</b>	<b>127</b>
<b>E</b>	<b>Non-ideal Transfer Function of Type I Inductor-based Circuit</b>	<b>129</b>
<b>F</b>	<b>Non-ideal Transfer Function of Type II MAB-based Circuit</b>	<b>131</b>

## LIST OF TABLES

2.1	Slopes and phase responses for the Type I asymmetric-slope band-pass filter. . . . .	15
2.2	Slopes and phase responses for the Type II asymmetric-slope band-pass filter. . . . .	16
3.1	Values of components used in SPICE simulation and experimental test for $C_\alpha = 1\mu F$ , $\alpha = 0.5$ . . . . .	37
3.2	Values of components used in SPICE simulation and experimental test for $C_\alpha = 3.7\mu F$ , $\alpha = 0.5$ . . . . .	42
4.1	Percentage variation in (a) center frequency $\omega_o$ and (b) $Q$ for all Type I active filter realizations with $\alpha = 0.5$ and $b = 1$ . . . . .	66
4.2	Percentage variation in (a) center frequency $\omega_o$ and (b) $Q$ for Type II inductor-based and MAB-based realizations with $\alpha = 0.5$ , $b = 1$ . . . . .	70
5.1	Slopes for $m^{th}$ order Type I asymmetric-slope band-pass filter. . . . .	77
5.2	Slopes for Type II $m^{th}$ order asymmetric-slope band-pass filter. . . . .	80

## LIST OF FIGURES

1.1	Ideal transmission characteristics of the (a) low-pass and (b) high-pass filter. . . . .	2
1.2	Ideal transmission characteristics of the (a) band-pass and (b) band-stop filter. . . . .	3
1.3	(a) Silicon-based fractional capacitors using photolithographic fractal structure on silicon and (b) tree fractal structure of the capacitors fabricated in [11,12]. . . . .	5
1.4	Response of $5 + \alpha$ proposed fractional-order low-pass filter in [17,18].	7
2.1	First order RC and RL lowpass filters. . . . .	11
2.2	Band-pass filters obtained using $s \rightarrow \frac{s^2 + \omega_0^2}{Bs}$ transformation on lowpass filters. . . . .	12
2.3	Band-pass filters obtained using $s \rightarrow \frac{s^2 + \omega_0^2}{Bs}$ transformation on lowpass filters. . . . .	13
2.4	Passive prototype models of the Type I asymmetric-slope band-pass filters. . . . .	14
2.5	Passive prototype models of the Type II asymmetric-slope band-pass filters. . . . .	14
2.6	Magnitude and phase responses of the proposed Type I FDNR-based asymmetric-slope band-pass filter in (1.5) to various values of $\alpha$ . . . .	17
2.7	Stable and unstable regions in the new $W$ -plane. . . . .	18
2.8	Relationship between poles, center frequency and quality factor. . . .	18
2.9	Roots of the transfer function (1.5) with $\alpha = 0.5$ , $k_1 = 1$ , $a = 0.01$ and $b = 1$ in (a) $W$ -plane and (b) $s$ -plane. . . . .	20
2.10	Quality factor versus $a$ at $b = 1$ for various values of $\alpha$ for Type I and Type II transfer functions in (1.5) and (1.7). . . . .	21
2.11	Step response of the Type I FDNR based filter in (1.5) at $a = 0.2$ , $b = 1$ and $\alpha = 0.5$ . . . . .	22

2.12	Magnitude and phase responses of the proposed Type II inductor-based asymmetric-slope band-pass filter in (1.7) to various values of $\alpha$ . . . .	23
2.13	Step response of the Type II inductor based filter in (1.7) at $a = 0.2$ , $b = 1$ and $\alpha = 0.5$ . . . . .	24
2.14	Magnitude and phase responses of the proposed Type I inductor-based asymmetric-slope band-pass filter in (1.6) to various values of $\alpha$ . . . .	26
2.15	Quality factor versus $a$ at $b = 1$ for various values of $\alpha$ for Type I inductor-based and Type II FDNR-based realizations. . . . .	27
2.16	Magnitude and phase responses of the proposed Type II FDNR-based asymmetric-slope band-pass filter in (1.8) to various values of $\alpha$ . . . .	28
2.17	Grounded FDNR based on Antonio's General Impedance Converter, whose input impedance is $Z_{in} = 1/RC^2s^2$ used in Type I FDNR-based asymmetric-slope band-pass filter. . . . .	30
2.18	Possible realizations of the Type I asymmetric-slope band-pass filter realizing the transfer function in (1.5); (a) using an FDNR and (b) using a multiple amplifier biquad. . . . .	31
2.19	Floating inductor based on Riordan technique, whose input impedance is $Z_i = RR_2R_3C_1s/R_1$ used in Type I inductor-based asymmetric-slope band-pass filter. . . . .	32
2.20	Possible realization of the Type I inductor-based asymmetric-slope band-pass filter realizing the transfer function in (1.6). . . . .	32
2.21	Grounded inductor based on Antonio's General Impedance Converter, whose input impedance is $Z_{in} = R_1R_2Cs$ used in Type II inductor-based asymmetric-slope band-pass filter. . . . .	33
2.22	Possible realizations of the Type II asymmetric-slope band-pass filter realizing the transfer function in (1.7); (a) using an inductor and (b) using a multiple amplifier biquad. . . . .	34
2.23	(a) Floating FDNR using current conveyors, whose input impedance is $Z_i = C_1C_2R_1R_2/(R_3s^2)$ . (b) $CCII-$ is realized using two $CCII+$ s. . . . .	35
2.24	Possible realization of the Type II FDNR-based asymmetric-slope band-pass filter realizing the transfer function in (1.8). . . . .	35
3.1	Approximation of $C_\alpha$ based on Carlson's method. . . . .	36
3.2	SPICE and experimental results of the Type I FDNR-based asymmetric-slope band-pass filter in Figure 2.18(a). . . . .	37

3.3	SPICE and experimental results of the filter in Figure 2.18(b); (a) showing the asymmetrical output at $V_{out}$ and (b) showing the symmetrical output at $V_{out1}$ . . . . .	38
3.4	Measured transient response of the Type I band-pass filter in Figure 2.18(a) confirming stability at $\alpha = 0.5$ . . . . .	39
3.5	SPICE and experimental results of the Type I band-pass filter in Figure 2.20. . . . .	40
3.6	Measured transient response of the Type I band-pass filter in Figure 2.20 confirming stability at $\alpha = 0.5$ . . . . .	40
3.7	SPICE and experimental results of the filter in Figure 2.22(a). . . . .	41
3.8	SPICE and experimental results of the filter in Figure 2.22(b); (a) showing the asymmetrical output at $V_{out}$ and (b) showing the symmetrical output at $V_{out1}$ . . . . .	41
3.9	Measured transient response of the Type II inductor-based band-pass filter in Fig. 2.22(a) for $\alpha = 0.5$ . . . . .	42
3.10	SPICE and experimental results of the filter in Figure 2.24. . . . .	43
3.11	Measured transient response of the Type II FDNR-based band-pass filter in Figure 2.24 confirming stability at $\alpha = 0.5$ . . . . .	43
3.12	AN231E04 FPAA development kit from Anadigm. . . . .	45
3.13	Approximated Type I asymmetric-slope band-pass filter in (3.2) implementation using gain, bilinear and biquadratic filter CAMs of the AnadigmDesigner tools for implementation on the AN231E04 FPAA. . . . .	46
3.14	Parameters setup environment of the AnadigmDesigner tools for the (a) bilinear and (b) biquadratic filter CAMs. . . . .	47
3.15	Internal switched capacitor circuits on the FPAA to realize the (a) pole/zero bilinear and (b) low-pass biquadratic transfer functions. . . . .	48
3.16	Experimental results using an FPAA for Type I asymmetric filter in 1.5 with $\alpha = 0.5, Q = 47.64$ . . . . .	49
3.17	Experimental results using an FPAA for Type I asymmetric filter in 1.5 with $\alpha = 0.1, Q = 45.1$ . . . . .	49
3.18	Approximated Type II asymmetric-slope band-pass filter in (3.3) implementation using gain, bilinear and biquadratic filter CAMs of the AnadigmDesigner tools for implementation on the AN231E04 FPAA. . . . .	51
3.19	Experimental results using an FPAA for Type II asymmetric filter in (1.7) with $\alpha = 0.5, Q = 39$ . . . . .	51

3.20	Experimental results using an FPAA for Type II asymmetric filter in (1.7) with $\alpha = 0.1, Q = 37.52$ . . . . .	52
4.1	Non-ideal model of the Type I FDNR-based filter accounting for the lossy FDNR as shown by the dashed line. . . . .	53
4.2	Plot of ratio $\frac{Q}{Q_I}$ versus $Q_D$ for Type I FDNR-based filter. $Q_I$ is the ideal quality factor of the filters with ideal elements and $Q$ is the observed quality factor of the filters with lossy elements. . . . .	54
4.3	Non-ideal model of the Type I inductor-based filter accounting for the lossy inductor as shown by the dashed line. . . . .	55
4.4	Plot of ratio $\frac{Q}{Q_I}$ versus $Q_L$ for Type I inductor-based filter. $Q_I$ is the ideal quality factor of the filters with ideal elements and $Q$ is the observed quality factor of the filters with lossy elements. . . . .	55
4.5	Non-ideal model of the Type II inductor-based filter accounting for the lossy inductor as shown by the dashed line. . . . .	56
4.6	Plot of ratio $\frac{Q}{Q_I}$ versus $Q_L$ for Type II inductor-based filter. $Q_I$ is the ideal quality factor of the filters with ideal elements and $Q$ is the observed quality factor of the filters with lossy elements. . . . .	57
4.7	Non-ideal model of the Type II FDNR-based filter accounting for the lossy FDNR as shown by the dashed line. . . . .	57
4.8	Plot of ratio $\frac{Q}{Q_I}$ versus $Q_D$ for Type II FDNR-based filter. $Q_I$ is the ideal quality factor of the filters with ideal elements and $Q$ is the observed quality factor of the filters with lossy elements. . . . .	58
4.9	The non-ideal fractional capacitor is modeled by an ideal fractional capacitor $C_\alpha$ in parallel with resistor $r$ . . . . .	59
4.10	Plot of the ratio of the actual $Q$ of the fractional capacitor to the ideal quality factor $Q_I$ versus $r$ for $C_\alpha = 1F$ and various values of $\alpha$ . . . . .	60
4.11	3D plots of (a) $\Delta\omega_o/\omega_o$ for $\alpha = [0.005, 1], a = [0.005, 1]$ and (b) $\Delta Q/Q$ for $\alpha = [0.005, 1], a = [0.005, 1]$ both for the FDNR-based Type I realization. . . . .	61
4.12	3D plots of (a) $\Delta\omega_o/\omega_o$ for $\alpha = [0.005, 1], a = [0.005, 1]$ and (b) $\Delta Q/Q$ for $\alpha = [0.005, 1], a = [0.005, 1]$ both for the MAB-based Type I realization. . . . .	63
4.13	3D plots of (a) $\Delta\omega_o/\omega_o$ for $\alpha = [0.005, 1], a = [0.005, 1]$ and (b) $\Delta Q/Q$ for $\alpha = [0.005, 1], a = [0.005, 1]$ both for the inductor-based Type I realization. . . . .	64

4.14	Plot of the amplitude response of the ideal transfer function of 1.5 compared to the non-ideal transfer functions of Figures 2.18(a) and (b) and 2.20 for $\tau_1 = \tau_2 = \tau = 100/\omega_t$ , $\tau_3 = 1$ , $\omega_t = 1000\omega_o$ and $b = 1$ .	65
4.15	3D plots of (a) $\Delta\omega_o/\omega_o$ for $\alpha = [0.005, 1]$ , $a = [0.005, 1]$ and (b) $\Delta Q/Q$ for $\alpha = [0.005, 1]$ , $a = [0.005, 1]$ both for the inductor-based Type II realization.	67
4.16	3D plots of (a) $\Delta\omega_o/\omega_o$ for $\alpha = [0.005, 1]$ , $a = [0.005, 1]$ and (b) $\Delta Q/Q$ for $\alpha = [0.005, 1]$ , $a = [0.005, 1]$ both for the Type II MAB-based realization.	69
4.17	Normalized plot of the amplitude response of the ideal transfer function of 1.7 compared to the non-ideal transfer functions of Figures 2.22(a) and 2.22(b) for $\alpha = 0.5$ , $a = 0.2$ , $\tau_1 = \tau_2 = \tau = 100/\omega_t$ , $\omega_t = 1000\omega_o$ and $b = 1$ .	71
4.18	Plot of the amplitude response of the ideal transfer function of (1.8) compared to the non-ideal transfer function of Figure 2.24 when current and voltage tracking errors of <i>CCII+</i> 's are considered. For all curves $\varepsilon_I = \varepsilon_V = 0.001$ , $\alpha = 0.5$ , $a = 0.2$ and $b = 1$ .	72
5.1	$m^{th}$ order RC and RL low-pass filters.	73
5.2	$m^{th}$ order band-pass filters schematics obtained by the $s \rightarrow \frac{s^2 + \omega_a^2}{Bs}$ transformation on low-pass filters in Figure 5.1.	74
5.3	$m^{th}$ order band-pass filters schematics, where $m$ is an integer.	75
5.4	$m^{th}$ order passive prototype models of Type I asymmetric-slope band-pass filter.	76
5.5	$\omega_o$ , $\omega_3$ and $\omega_4$ in the Type I asymmetric-slope band-pass filters.	78
5.6	$m^{th}$ order passive prototype models of Type II asymmetric-slope band-pass filter.	79
5.7	$\omega_o$ , $\omega_3$ and $\omega_4$ in the Type II asymmetric-slope band-pass filters.	81
5.8	Passive prototype model of a fourth order Type I FDNR-based filter using one fractional capacitor.	82
5.9	Magnitude response of the proposed fourth-order Type I filter in (5.18) to various values of $\alpha$ .	83
5.10	Step response of the fourth order FDNR based filter in (5.19) at $a = b = d = 2$ , $c = e = 1$ and $\alpha = 0.5$ .	84
5.11	Possible realization of fourth-order Type I FDNR-based asymmetric-slope band-pass filter.	85

5.12	SPICE and experimental results of the filter in Figure 5.11. . . . .	85
5.13	Measured transient response of the fourth order Type I FDNR-based band-pass filter in Figure 5.11 confirming stability at $\alpha = 0.5$ . . . . .	86
5.14	Approximated fourth order Type I band-pass filter in (5.20) using four biquadratic filter CAMs. . . . .	87
5.15	Experimental result using an FPAA for fourth order Type I asymmetric-slope filter in (5.19) with $\alpha = 0.1, Q = 30.5$ . . . . .	87
5.16	Experimental result using an FPAA for fourth order Type I asymmetric-slope filter in (5.19) with $\alpha = 0.1, Q = 30.5$ . . . . .	88
5.17	Passive prototype model of fourth order Type I inductor-based filter using one fractional capacitor. . . . .	89
5.18	Magnitude response of the proposed fourth-order Type I filter in (5.21) to various values of $\alpha$ . . . . .	90
5.19	Possible realization of fourth-order Type I inductor-based asymmetric-slope band-pass filter. . . . .	90
5.20	SPICE and experimental results of the filter in Figure 5.19. . . . .	91
5.21	Measured transient response of the fourth order Type I inductor-based band-pass filter in Figure 5.19 confirming stability at $\alpha = 0.5$ . . . . .	92
5.22	Passive prototype model of fourth order Type II inductor-based filter using one fractional capacitor. . . . .	92
5.23	Magnitude response of the proposed fourth-order Type II filter in (5.23) to various values of $\alpha$ . . . . .	93
5.24	Step response of the fourth order inductor based filter in (5.24) at $a = b = d = 2, c = e = 1$ and $\alpha = 0.5$ . . . . .	93
5.25	Possible realization of fourth-order Type II inductor-based asymmetric-slope band-pass filter. . . . .	94
5.26	SPICE and experimental results of the filter in Figure 5.25. . . . .	95
5.27	Measured transient response of the fourth order Type II inductor-based band-pass filter in Figure 5.25 confirming stability at $\alpha = 0.5$ . . . . .	95
5.28	Approximated fourth order Type II band-pass filter in (5.25) using four biquadratic filter CAMs. . . . .	96
5.29	Experimental result using an FPAA for fourth order Type II asymmetric-slope band-pass filter in (5.24) with $\alpha = 0.1, Q = 32$ . . . . .	97
5.30	Experimental result using an FPAA for fourth order Type II asymmetric-slope band-pass filter in (5.24) with $\alpha = 0.5, Q = 42$ . . . . .	98

5.31	Passive prototype model of fourth order Type II FDNR-based asymmetric band-pass filter using one fractional capacitor. . . . .	98
5.32	Magnitude response of the proposed fourth-order Type II filter in (5.26) to various values of $\alpha$ . . . . .	99
5.33	Possible realization of fourth-order Type II FDNR-based asymmetric-slope band-pass filter. . . . .	100
5.34	SPICE and experimental results of the filter in Figure 5.33. . . . .	100
5.35	Measured transient response of the fourth order Type II FDNR-based asymmetric-slope band-pass filter in Figure 5.33 confirming stability at $\alpha = 0.5$ . . . . .	101
A.1	Comparison between magnitude responses of the approximated fractional capacitor and ideal fractional capacitor at $C = 1\mu F$ and $\alpha = 0.75$ . . . . .	114
A.2	RC tree to realize fourth order approximated fractional Laplacian operator based on Carlson's approximation technique. . . . .	115
A.3	Comparison between the magnitude and phase responses of the approximated and ideal fractional capacitors with the impedance of $Z_{c_\alpha}(j\omega) = \frac{1}{1\mu F(j\omega)^{0.5}}$ centered around $1kHz$ . . . . .	116
A.4	Comparison between the magnitude and phase responses of the approximated and ideal fractional capacitors with the impedance of $Z_{c_\alpha}(j\omega) = \frac{1}{3.7\mu F(j\omega)^{0.5}}$ centered around $10kHz$ . . . . .	117
A.5	Maple code to generate component values for the RC ladder network of a fractional capacitor $Z_{c_\alpha}(j\omega) = \frac{1}{1\mu F(j\omega)^{0.5}}$ at a center frequency of $1kHz$ . . . . .	120
B.1	Grounded inductor whose input impedance is $Z_{in} = RR_1C_1s$ used in second order Type II inductor-based asymmetric-slope band-pass filter and (b) Possible realization of the Type II asymmetric-slope band-pass filter realizing (1.7). . . . .	122
B.2	SPICE and experimental results of the filter in Figure B.1(b). . . . .	123
C.1	The Matlab Code used to find the percentage variability of $\Delta\omega_o/\omega_o$ shown in Figure 4.11(a). . . . .	125
C.2	The Matlab Code used to find the percentage variability of $\Delta Q/Q$ shown in Figure 4.11(b). . . . .	126
D.1	The non-ideal transfer function of Type I MAB based circuit of Figure 2.18(b). . . . .	128

E.1	The non-ideal transfer function of Type I Inductor based circuit of Figure 2.20. . . . .	130
F.1	The non-ideal transfer function of Type II MAB based circuit of Figure 2.22(b). . . . .	132

## Glossary

Acronom	Definition
Q	Quality Factor
FDNR	Frequency Dependent Negative Resistor
MAB	Multiple Amplifier Biquad
opamp	Operational Amplifier
FPAA	Field Programmable Analog Array
CAM	Configurable Analog Module

# CHAPTER 1

## Introduction

### 1.1 Integer-Order Filters

In Electrical Engineering, a filter is a frequency-selective circuit that passes a specified band of frequencies and blocks or attenuates signals of frequencies outside this band. These signals are usually voltages. An ideal filter has a frequency band over which the magnitude of transmission is unity (the filter passband) and a frequency band over which the transmission is zero (the filter stopband). Figures 1.1 and 1.2 show the ideal transmission characteristics of the four major filter types: low-pass in Figure 1.1(a), high-pass in Figure 1.1(b), band-pass in Figure 1.2(a) and band-stop in Figure 1.2(b). These idealized characteristics, by virtue of their vertical edges, are known as brick-wall responses [1–4].

Filter design is one of the very few areas of electrical engineering for which a complete design theory exists [1–4]. The classical linear circuit theory upon which electronic circuits are designed today is based on integer-order differential equations which reflect the behavior of the well-known elements: the resistor, the capacitor, the inductor and the memresistor<sup>1</sup> in the time domain. Via Laplace transforms, integer-order algebraic equations in the complex frequency  $s$ -domain can be used to describe linear dynamical systems. Accordingly, electronic filters are traditionally classified as 1st-order, 2nd-order or  $n^{\text{th}}$ -order circuits where  $n$  is an integer number. The circuit

---

<sup>1</sup>Memresistor is a passive two-terminal circuit element in which there is a functional relationship between charge and magnetic flux linkage.

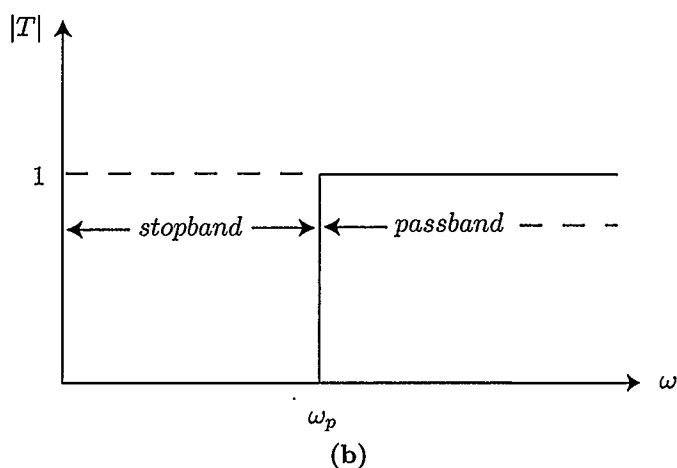
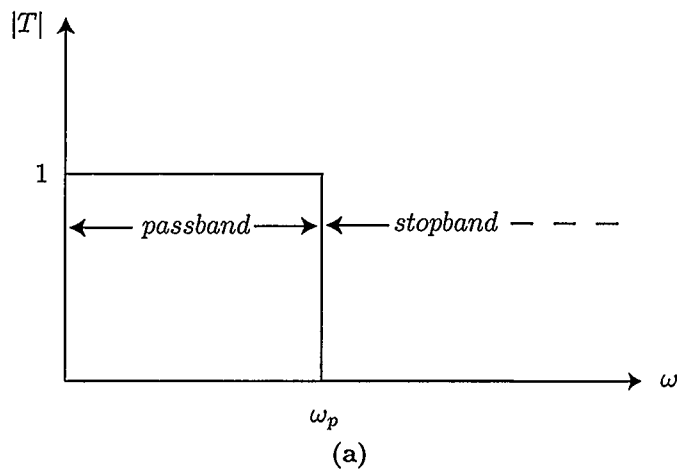


**Figure 1.1:** Ideal transmission characteristics of the (a) low-pass and (b) high-pass filter.

order is directly proportional to the number of energy storage elements in the circuit. The describing transfer function of the integer-order filters are usually of the form  $T(s) = N(s)/D(s)$  where  $N(s)$  and  $D(s)$  are polynomials in the Laplacian operator  $s$  raised to an integer exponent; i.e  $s$ ,  $s^2$  or  $s^n$ .

## 1.2 Band-pass Filters

Whether passive or active, band-pass filters are indispensable parts in electronic circuit applications [1–5]. Several methods have been introduced for designing continuous-time integer-order band-pass filters over the years [1, 2, 5, 6]. A band-pass filter is a

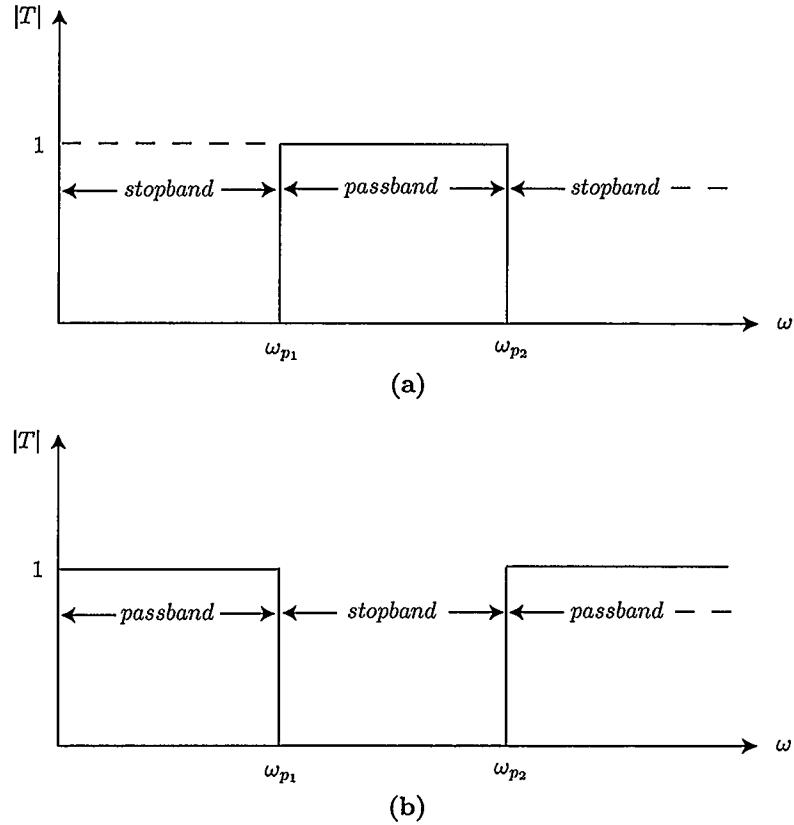


**Figure 1.2:** Ideal transmission characteristics of the (a) band-pass and (b) band-stop filter.

device that passes frequencies within a certain range and rejects or attenuates frequencies outside that range. Bandwidth is defined as the frequency range between two specified frequency cut-off points, that are 3dB below the maximum centre or resonant peak while attenuating or weakening the others outside of these two points. An ideal band-pass filter would have a completely flat passband and would completely attenuate all frequencies outside the passband. In practice, no band-pass filter is ideal. The filter does not attenuate all frequencies outside the desired frequency range completely; in particular, there is a region just outside the intended passband where frequencies are attenuated, but not rejected.

### 1.3 Fractional Capacitor

Works [7] and [8] introduce new methods to approximate a fractional capacitor whose impedance is  $Z_{c_\alpha} = \frac{1}{C_\alpha s^\alpha}$ , where  $C_\alpha$  is the capacitance and  $\alpha$  ( $0 < \alpha < 1$ ) is its order. If a sinusoidal current  $I(t) = I_o \sin(\omega t)$  is used to excite a fractional capacitor, the voltage developed across it can be shown to be given by [9]

$$V(t) = L^{-1}[s^\alpha I(s)] = I_o \omega^\alpha \left[ \sin_\alpha(\omega t) \cos\left(\frac{\alpha\pi}{2}\right) + \cos_\alpha(\omega t) \sin\left(\frac{\alpha\pi}{2}\right) \right], \quad (1.1)$$

where  $\sin_\alpha(\omega t)$  and  $\cos_\alpha(\omega t)$  are respectively given by

$$\sin_\alpha(\omega t) = \sum_{k=0}^{\infty} e_{k-\alpha}^{\omega t} \sin(k - \alpha) \frac{\pi}{2}, \quad (1.2)$$

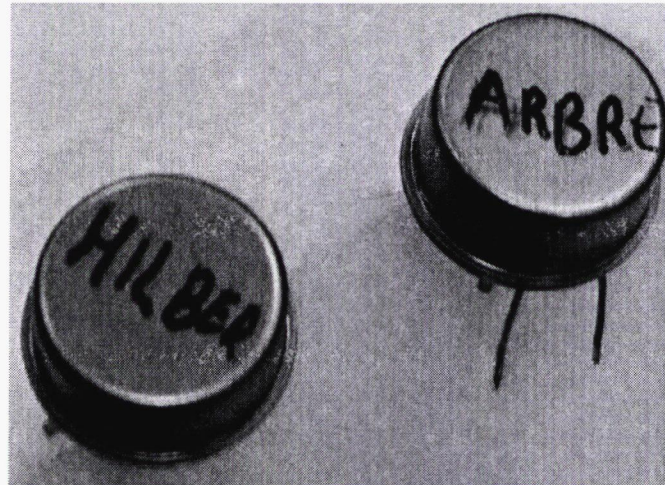
and

$$\cos_\alpha(\omega t) = \sum_{k=0}^{\infty} e_{k-\alpha}^{\omega t} \cos(k - \alpha) \frac{\pi}{2}. \quad (1.3)$$

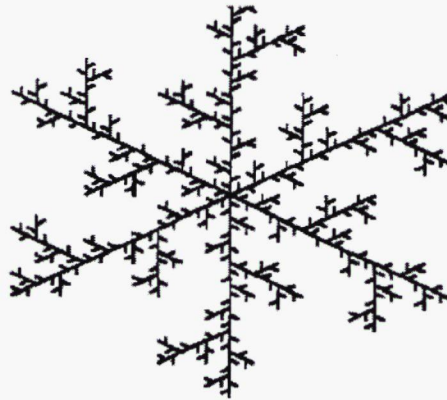
The fractional capacitor approximations have been appealing only to those seeking to experiment with fractional-order circuits to prove a concept but have never been appealing to real-world circuit designers. The reason is economics since several capacitors are needed just to approximate one capacitor with a non-integer-order.

The authors of [10] proposed a capacitive probe fabricated in such a way that it displays a metal-insulator-liquid interface when placed into a liquid. The proposed capacitive probe has a fractional-order impedance and  $\alpha$  varies with the amount of liquid immersion. The proposed capacitive probe is bulky and cannot be applied to the real circuits. But it shows that further work in material properties are needed in order to fabricate a commercial device.

Silicon-based fractional capacitors were proposed, fabricated and tested in [11,12].



(a)



(b)

**Figure 1.3:** (a) Silicon-based fractional capacitors using photolithographic fractal structure on silicon and (b) tree fractal structure of the capacitors fabricated in [11,12].

The idea was to use of fractal geometry to lithographically implement a capacitor using a standard silicon process. The fractional-order of the capacitor  $\alpha$  is related to the geometry of the fractal pattern used. The authors in [11,12] built a Hilbert-type capacitor with the capacitance of  $C_\alpha = 7.5nF$  and  $\alpha = 0.5$  and a Arbre-type capacitor with  $C_\alpha = 1.5nF$  and  $\alpha = 0.5$ . Figure 1.3 shows the Hilbert-Type and Arbre-Type fractional capacitor using photolithographic fractal structure on silicon and their tree fractal structure.

All the circuits in this work require a single fractional capacitor. As of the time of this writing, there are no commercial fractional capacitors and therefore we use an approximation based on Carlson's method [7] to mimic the fractional capacitor. The overhead of using an emulation of the fractional capacitor is still acceptable given the complexity of other techniques.

#### 1.4 Fractional-Order Filters

The classical linear circuit theory upon which electronic circuits are designed today is based on integer-order differential equations. However, using fractional calculus, filters can also be represented by more general fractional-order differential equations in which case integer-order filters are only a subset of fractional-order filters. The Riemann–Liouville definition of a fractional derivative of order  $\alpha$  is given by

$$\frac{d^\alpha}{dt^\alpha} f(t) = \frac{1}{\Gamma(m-\alpha)} \frac{d^m}{dt^m} \int_0^t \frac{f(\tau)}{(t-\tau)^{\alpha+1-m}} d\tau \quad (1.4)$$

where  $\Gamma(\cdot)$  is the gamma function,  $m$  is an integer and  $m-1 < \alpha < m$  [13,14].

The authors in [15–17] were the first to generalize first and second-order low-pass filters to the fractional domain showing some clear benefits. The stopband attenuation of integer-order filters is  $-20n \text{ dB/dec}$  while the attenuation of the proposed fractional-order filters in [15–17] is  $-20n(n+\alpha) \text{ dB/dec}$  which allows for stepping the attenuation very precisely. In addition, the filters magnitude and phase responses, cut off frequency and quality factor are functions of fractional order  $\alpha$ . The authors in [17] and [18] worked on the realization of higher-order fractional step filters with maximally-flat response. Figure 1.4 shows a plot of the magnitude response of the proposed fractional-order low-pass filter in [17] and [18] of order  $5 + \alpha$ .

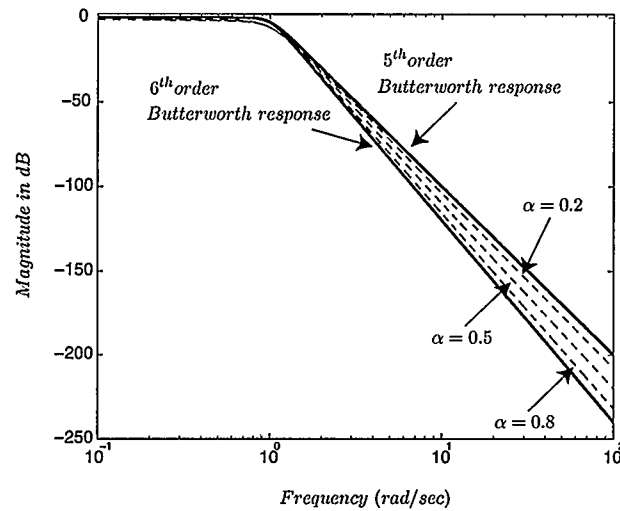


Figure 1.4: Response of  $5 + \alpha$  proposed fractional-order low-pass filter in [17,18].

### 1.5 High Quality Factor Asymmetric-Slope Band-Pass Filters

High selectivity and low pass-band insertion loss of microwave band-pass filters are needed for many applications, such as the rapidly expanding area of mobile communications networks [19–21]. These requirements are imposed to conserve the valuable frequency spectrum and improve the performance of the systems. Generally, band-pass filters can obtain a higher selectivity by increasing the degree of poles, i.e. the number of resonators. However, because of finite quality factor of the resonators, the insertion loss of the band-pass filter is increased as the number of resonators increases. Therefore, there is always a trade-off between obtaining a higher selectivity and the insertion loss in the band-pass filters. In addition, some applications of band-pass filters may need a higher selectivity on only one side of the pass band, but less or none on the other side [19–21]. It would be desirable to use a filter with asymmetric frequency characteristics in such cases. This is because a symmetric frequency-response band-pass filter requires a larger number of resonators which results in a higher insertion loss in the passband, a larger size and a higher cost.

All available techniques that have been proposed up until now for the design of

such filters were microwave-based techniques that have only been verified using micro-strip based circuits [19–22]. High selective-slope band-pass filters with asymmetric-slope characteristics are needed in the receive filter of some personal communication networks [19–21]. Several methods have been introduced for designing asymmetric-slope band-pass filters over the years [20–22]. In [20], cross-coupled open-loop resonators were introduced to show asymmetric frequency characteristics in a micro-strip trisection band-pass filter. In [21], an asymmetric synthesis method based on flexibility in placing the transmission zeros was used to increase the skirt selectivity of one side of a band-pass filter. In [22], band-pass filters with asymmetric-slope characteristics were realized using low-loss ceramic resonators. The selectivity of one side of the band-pass filter was improved by using a capacitively coupled network with finite transmission zeros.

On the other hand, obtaining high quality factors with such filters is not an easy task. In order to have a large quality factor ( $Q$ ), at least one pair of poles should be located very close to the stability boundary.

In this thesis, we propose new methods for designing continuous-time asymmetric-slope band-pass filters which can also achieve high quality factors. These methods are centered around the realization of the new transfer functions

$$H_I(s) = k_1 \frac{as^\alpha}{s^2 + as^\alpha + b} \quad (1.5)$$

$$H_{II}(s) = k_2 \frac{as^{1-\alpha}}{s^2 + as^{1-\alpha} + b} \quad (1.6)$$

which we refer to as Type I second-order asymmetric-slope band-pass filter transfer functions and the units of the constant  $a$  are  $(rad/sec)^{2-\alpha}$  and  $(rad/sec)^{1+\alpha}$ , respectively. Similarly, we refer to the transfer functions below as the Type II second-order asymmetric-slope band-pass filter transfer functions.

$$H_{III}(s) = k_3 \frac{as^{1+\alpha}}{s^2 + as^{1+\alpha} + b} \quad (1.7)$$

$$H_{IV}(s) = k_4 \frac{as^{2-\alpha}}{s^2 + as^{2-\alpha} + b} \quad (1.8)$$

The units of the constant  $a$  are  $(rad/sec)^{1-\alpha}$  and  $(rad/sec)^\alpha$ , respectively and the unit of the constant  $b$  for the four new proposed transfer functions is  $(rad/sec)^2$ . Here,  $s^\alpha = (j\omega)^\alpha = \omega^\alpha [\cos(\frac{\alpha\pi}{2}) + j \sin(\frac{\alpha\pi}{2})]$  and  $0 < \alpha < 1$  [15]. These second-order band-pass filter transfer functions are different from the one studied in [16] and given by

$$H(s) = k \frac{as^\alpha}{s^{2\alpha} + as^\alpha + b} \quad (1.9)$$

which represents a symmetrical-only fractional-order band-pass filter of order  $2\alpha$ . As will be shown later in Chapter 2, an advantage of filters proposed in this work is that they can achieve high quality factors by selecting  $\alpha$  appropriately. The practical realization of fractional filters on a Field Programmable Analog Array (FPAA) was recently reported in [23]. Here, we also validate our designed high- $Q$  asymmetrical filters using an FPAA in addition to implementing six discrete circuits for second-order filters; two based on a Frequency Dependent Negative Resistor (FDNR), two based on an inductor and two based on Multiple Amplifier Biquads (MABs). The techniques extend to higher order filters and four circuits for two types of fourth-order asymmetric-slope band-pass filter which are proposed, simulated in SPICE and verified experimentally using discrete components and FPAA technique as well.

## 1.6 Thesis layout

This thesis is divided into two basic areas of research focus. First, new techniques for design and implementation of high quality factor second-order asymmetric-slope band-pass filters are presented. Second, these techniques are used to generate higher

order asymmetric-slope band-pass filters.

Chapter 2 looks at passive prototypes of second-order asymmetric-slope band-pass filters and their equivalency. Two types of second-order asymmetric-slope band-pass filters are presented and the symmetry in the relationship of one transfer function to the next is highlighted. Exact expressions for  $\omega_o$  and two different slopes, and approximate expressions for the  $Q$  of each filter are presented. Circuit designs are also presented in Chapter 2.

Chapter 3 provides simulation results for the proposed second-order asymmetric-slope band-pass filters. Furthermore, the approach is verified experimentally using discrete components and FPAA technique.

The non-ideal effects of the second-order asymmetric-slope band-pass filters are presented in Chapter 4. Four non-ideal transfer functions using lossy elements are given and discussed in Chapter 4. The effects of finite gain band-width product in operational amplifiers and the current and voltage tracking errors in non-ideal current conveyors are also discussed in Chapter 4.

The techniques to design second order band-pass filters are used to generate higher order asymmetric-slope band-pass filters in Chapter 5. This chapter looks at passive prototypes of  $m^{th}$  order asymmetric-slope band-pass filters and their equivalency, and evaluates expressions for two different slopes and phases. Possible designs and simulation and experimental results using discrete components and FPAA technique are also presented in Chapter 5.

Chapter 6 provides conclusions of this thesis and suggests improvements for future work.

## CHAPTER 2

### Asymmetric-Slope Band-pass Filters

#### 2.1 Passive Prototypes

Consider the lowpass filters in Figures 2.1(a) and (b). The filters can be transformed into normal integer order band-pass filters using the  $s \rightarrow \frac{s^2 + \omega_o^2}{Bs}$  transformation where  $\omega_o$  is center frequency and  $B$  is the bandwidth of the band-pass filter. Now consider the band-pass filters in Figures 2.2(a) and (b), obtained by applying this transformation on the corresponding lowpass filters, respectively. In other words, a lowpass filter can be transformed into band-pass filter circuit by replacing the capacitor  $C$  with a

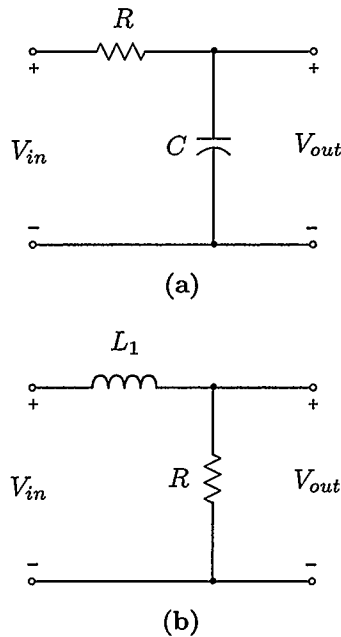


**Figure 2.1:** First order RC and RL lowpass filters.

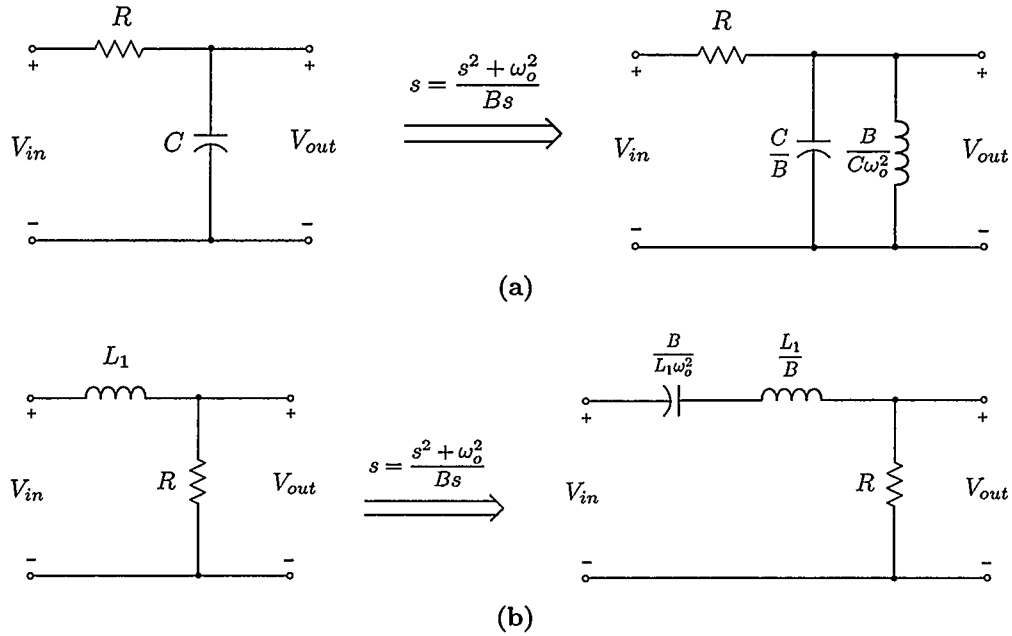
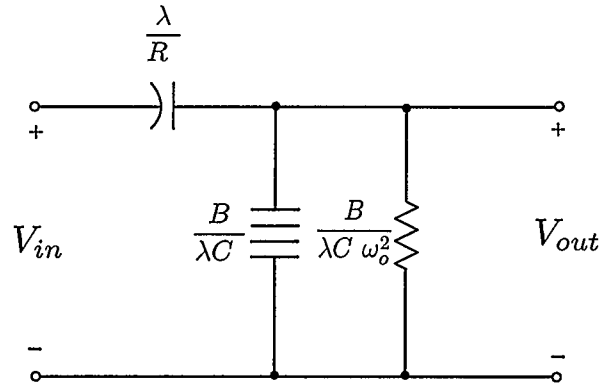


**Figure 2.2:** Band-pass filters obtained using  $s \rightarrow \frac{s^2 + \omega_o^2}{Bs}$  transformation on lowpass filters.

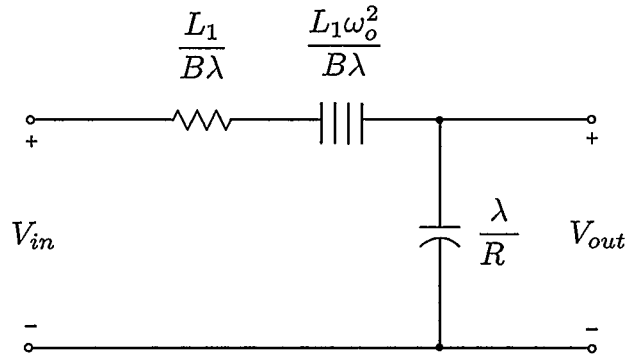
parallel combination of capacitor and inductor of values  $\frac{C}{B}$  and  $\frac{B}{C\omega_o^2}$ , respectively and replacing the inductor  $L$  with a series combination of capacitor and inductor of values  $\frac{B}{L\omega_o^2}$  and  $\frac{L}{B}$ , respectively.

Now consider the multiplication of each element of the circuits in Figures 2.2(a) and (b) by a scaling factor  $1/\lambda s$  where  $\lambda$  is a constant of dimension  $sec^{-1}$ . The resulting circuits are shown in Figures 2.3(a) and (b). This transformation is referred to as Bruton  $RLC : CRD$  transformation [24]. Continuous-time second-order asymmetric-slope band-pass filters can be obtained from integer-order band-pass filters in Figures 2.2 and 2.3 by replacing the resistors in Figure 2.2 and the capacitors in Figure 2.3 with fractional order capacitors.

Consider the passive prototype Type I and Type II filters shown in Figures 2.4 and 2.5, respectively. Each employs a fractional-order capacitor  $C_{\alpha_i}$  ( $i = 1, 2, 3, 4$ ) whose impedance is  $1/C_{\alpha_i} s^{\alpha_i}$  where  $C_{\alpha}$  is the value of the capacitor and  $0 < \alpha < 1$ . Figures 2.4(a) and (b) realize Type I transfer functions in (1.5) and (1.6) and Figures



(a)



(b)

**Figure 2.3:** Band-pass filters obtained using  $s \rightarrow \frac{s^2 + \omega_o^2}{Bs}$  transformation on lowpass filters.

2.5(a) and (b) realize Type II transfer functions in (1.7) and (1.8), respectively if  $\alpha_1 = \alpha_2 = \alpha_3 = \alpha_4 = \alpha$  and  $k_1 = k_2 = k_3 = k_4 = 1$ . The equivalence between the two circuits of Figures 2.4(a) and 2.5(a) can be easily seen if one considers the multiplication of each element of the Type II filter in Figures 2.5(a) by a scaling factor  $1/\lambda s$  where  $\lambda$  is a constant of dimension  $sec^{-1}$ . For circuits in Figures 2.4(a) and 2.5(a) it follows then that  $R_1 \equiv L/\lambda$ ,  $D \equiv \lambda C_1$  and  $C_{\alpha_1} \equiv \lambda C_{\alpha_3}$  where  $\alpha_1$  and  $\alpha_3$  would be related by  $\alpha_1 = 1 + \alpha_3$ . Similarly, Type II filter in Figure 2.5(b) can be obtained from Type I in Figure 2.4(b) if one considers the multiplication of each element of the Type I circuit by a scaling factor  $1/\lambda s$ . The passive prototype Type II in Figure 2.5(b) is equivalent to Type I in Figure 2.4 (b) for  $R \equiv L/\lambda$ ,  $D \equiv \lambda C$

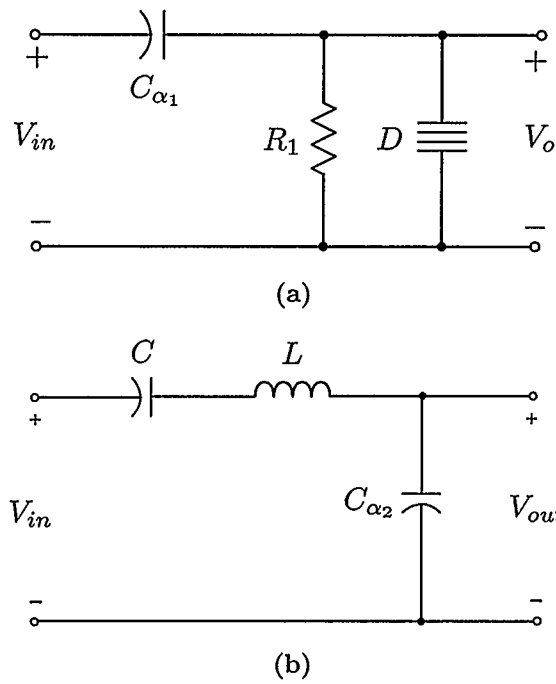


**Figure 2.4:** Passive prototype models of the Type I asymmetric-slope band-pass filters.

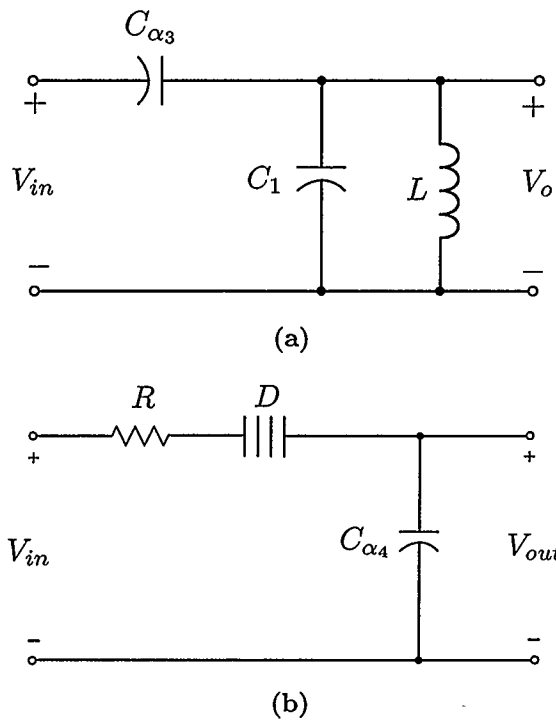


**Figure 2.5:** Passive prototype models of the Type II asymmetric-slope band-pass filters.

Frequency	Type I FDNR-based	
	Slope (dB/dec)	$\phi$
$\omega \ll \omega_o$	$0 < 20\alpha < 20$	$\frac{\alpha\pi}{2}$
$\omega \gg \omega_o$	$20 < 20(2 - \alpha) < 40$	$\pi \left( \frac{\alpha}{2} - 1 \right)$

(a)

Frequency	Type I inductor-based	
	Slope(dB/Dec)	$\phi$
$\omega \ll \omega_o$	$0 < 20(1 - \alpha) < 20$	$\frac{(1-\alpha)\pi}{2}$
$\omega \gg \omega_o$	$20 < 20(1 + \alpha) < 40$	$-(1 + \alpha) \frac{\pi}{2}$

(b)

**Table 2.1:** Slopes and phase responses for the Type I asymmetric-slope band-pass filter.

and  $C_{\alpha_4} \equiv \lambda C_{\alpha_2}$ , where  $\alpha_2$  and  $\alpha_4$  would be related by  $\alpha_4 = 1 + \alpha_2$ . The Type I and Type II filters in Figures 2.4(a) and 2.5(a) are related through the  $C_{\alpha_3}LC_1 : C_{\alpha_1}R_1D$  transformation and the relationship between Type I and Type II filters in Figures 2.4(b) and 2.5(b) can be explained by the  $C_{\alpha_2}LC : C_{\alpha_4}RD$  transformation which are analogous to the Bruton  $RLC : CRD$  transformation [24]. The equivalence between the four transfer functions, interesting enough, results in having different filter slopes and phases which are complimentary as illustrated in Tables 2.1 and 2.2. Here  $\omega_o$  is the center frequency of the particular filter and the slopes are given in  $dB/dec$ .

### 2.1.1 Type I FDNR-Based Asymmetric-Slope Band-pass Filter

Now with reference to (1.5), the magnitude and phase functions for Type I FDNR-based circuit shown in Figure 2.4(a) are respectively given by

$$|H_I(j\omega)| = \frac{k_1}{\sqrt{1 + 2x \cos(\alpha\pi/2) + x^2}} \quad (2.1a)$$

$$\angle H_I(j\omega) = \frac{\alpha\pi}{2} - \tan^{-1} \frac{\sin(\alpha\pi/2)}{x + \cos(\alpha\pi/2)} \quad (2.1b)$$

Frequency	Type II inductor-based	
	Slope (dB/dec)	$\phi$
$\omega \ll \omega_o$	$20 < 20(1 + \alpha) < 40$	$(1 + \alpha) \frac{\pi}{2}$
$\omega \gg \omega_o$	$0 < 20(1 - \alpha) < 20$	$\pi \left( \frac{\alpha-1}{2} \right)$

(a)

Frequency	Type II FDNR-based	
	Slope(dB/Dec)	$\phi$
$\omega \ll \omega_o$	$20 < 20(2 - \alpha) < 40$	$(2 - \alpha) \frac{\pi}{2}$
$\omega \gg \omega_o$	$0 < 20\alpha < 20$	$-\frac{\alpha\pi}{2}$

(b)

**Table 2.2:** Slopes and phase responses for the Type II asymmetric-slope band-pass filter.

where  $x = (b - \omega^2)/a\omega^\alpha$ . The frequency  $\omega_o$  at which the magnitude response has its maximum is given by

$$\omega_o = e^{y_1/\alpha} \quad (2.2)$$

where  $y_1$  is a root of the equation

$$2y + \alpha \left[ y - \ln \left( be^y + ae^{2y} \cos \frac{\alpha\pi}{2} \right) \right] = 0 \quad (2.3)$$

which can be found numerically. For  $a \ll b$ , it can be easily shown that  $\omega_o \approx \sqrt{b}$ . Figure 2.6 shows the magnitude and phase responses for the Type I FDNR-based asymmetric band-pass filter shown in Figure 2.4(a) at  $k_1 = 1$ ,  $a = 0.01$ ,  $b = 1$ .

From a stability point of view, (1.5), (1.6), (1.7) and (1.8) are stable if  $a > 0$  and  $0 < \alpha < 1$ . (1.5) and (1.8) become unstable for  $\alpha = 0$  and  $\alpha > 1$  while the transfer functions in (1.6) and (1.7) are unstable for  $\alpha \geq 1$ , respectively [25]. However, to find the quality factor  $Q$  of Type I FDNR-based filter governed by (1.5) we need to find the poles in the so-called  $W$ -plane defined as  $W = s^\alpha$  [25]. The poles of the transfer

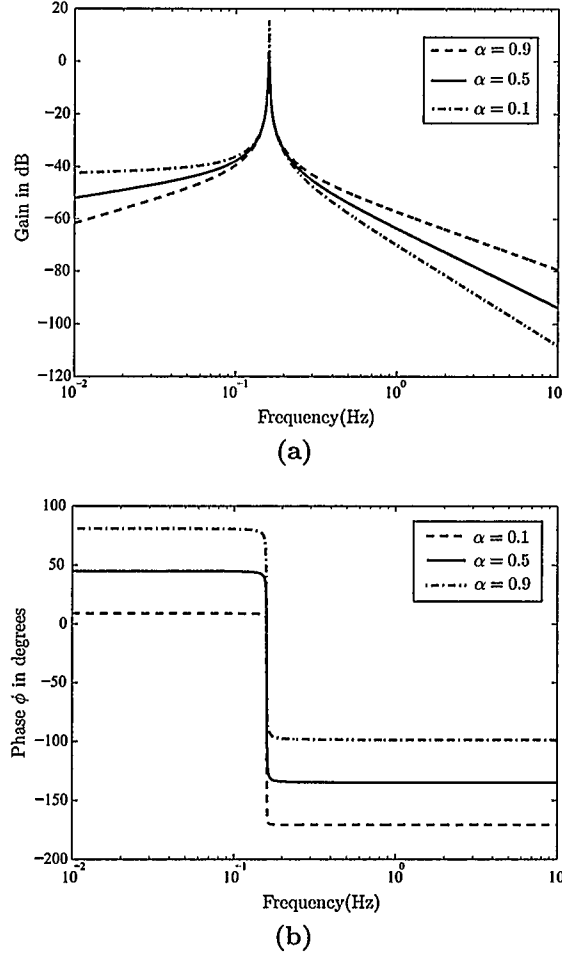


**Figure 2.6:** Magnitude and phase responses of the proposed Type I FDNR-based asymmetric-slope band-pass filter in (1.5) to various values of  $\alpha$ .

function in (1.5) can be obtained by solving the equation below.

$$W^{2/\alpha} + aW + b = 0 \quad (2.4)$$

It should be noted that all the poles should be located in the stable region ( $|\theta_\omega| > \frac{\alpha\pi}{2}$ ) to have a stable system. Note that the transfer function in (1.5) approaches the normal integer-order band-pass transfer function for  $\alpha = 1$ . In the case of  $\alpha = 1$ , the stability border will be ( $|\theta_\omega| = \frac{\pi}{2}$ ), which is the same as the stability border in the  $s$ -plane. Figure 2.7 shows the stable region in the  $W$ -plane. It is clear from

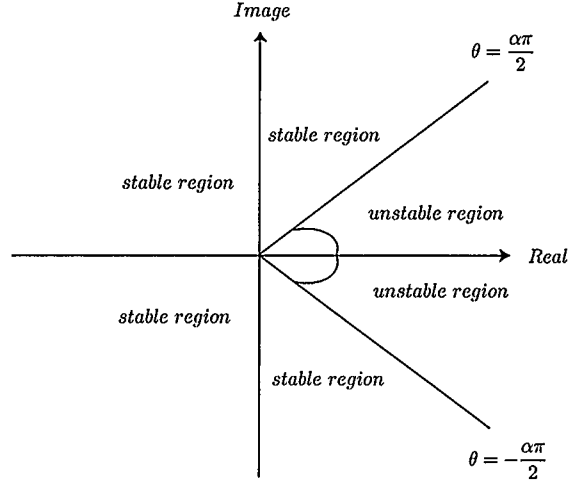


Figure 2.7: Stable and unstable regions in the new  $W$ -plane.

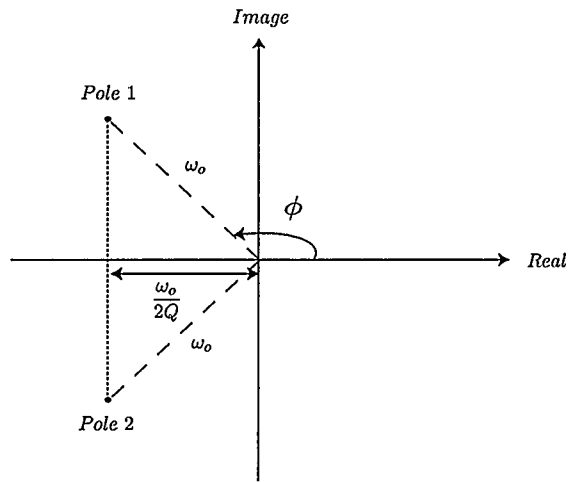


Figure 2.8: Relationship between poles, center frequency and quality factor.

Figure 2.7 that the region of instability in the  $W$ -plane is smaller than in  $s$ -plane. Another feature of this new plane is that the stable region in the  $W$ -plane decreases as  $\alpha$  increases.  $Q$  can then be calculated by converting the pair of poles closest to the stability boundary (i.e. the ones with corresponding angle  $\theta$  closest to the value  $\alpha\pi/2$ ) back to the  $s$ -plane ( $s = W^{1/\alpha}$ ). Figure 2.8 shows the relationship between poles, center frequency and quality factor in  $s$ -plane. Quality factor can be calculated by the equation below

$$Q = -\frac{1}{2\cos(\phi)} \quad (2.5)$$

As an example, here we find the quality factor of Type I filter in (1.5) with  $\alpha = 0.5$ ,  $k_1 = 1$ ,  $a = 0.01$  and  $b = 1$ . The corresponding characteristic equation in the  $W$ -plane is,

$$W^4 + 0.01W + 1 = 0 \quad (2.6)$$

The equation has four roots in  $p_{1,2} = -0.707 \pm 0.704i$  and  $p_{3,4} = 0.707 \pm 0.709i$  with respective angles of  $\theta_{\omega_{1,2}} = \pm 135.12^\circ$  and  $\theta_{\omega_{3,4}} = \pm 45.08^\circ$ . There is no pole in the unstable region ( $-45^\circ < \theta_w < 45^\circ$ ) and therefore the system is stable. Converting the pair of poles closest to the stability boundary ( $p_{3,4} = 0.707 \pm 0.709i$ ) back using the equation ( $s = W^2$ ) results in  $\widehat{p}_{3,4} = -0.0035 \pm 1.0035i$  in the  $s$ -plane. For this pole pair, the angle is  $\phi = 90.2$  degrees and the quality factor is  $Q = 143.35$  using equation (2.5). Figure 2.9(a) and (b) show the place of roots in the  $W$  and  $s$ -planes.

The previous example shows that for a fixed  $\alpha$  ( $0 < \alpha < 1$ ) and for  $a \ll b$ , at least one pair of poles is located close to the stability boundary and results in a very large  $Q$ . Note that depending on the value of  $\alpha$  multiple poles may exist in the  $W$ -plane. The stable region in the  $W$ -plane gets smaller as  $\alpha$  increases and for  $\alpha > 1$  at least one pair of poles exists in the unstable region, resulting in an unstable system. Figure (2.10) shows the values of  $Q$  versus  $a$  when  $b = 1$  for five different values of  $\alpha$ . It is clear that large  $Q$  values are obtained for small  $\alpha$  (Type I FDNR-based) and small values of  $a$ . Numerically, the following approximate relationship was found for the Type I FDNR-based filter response,

$$\frac{1}{Q} \approx \alpha \cdot \left[ \frac{a}{b^{(1-0.5\alpha)}} \right]^{0.8686} \quad (2.7)$$

The step response of the filter can be obtained by substituting for the non-integer Laplacian operator  $s^\alpha$  with the second-order approximation

$$s^\alpha \approx \frac{(\alpha^2 + 3\alpha + 2)s^2 + (8 - 2\alpha^2)s + (\alpha^2 - 3\alpha + 2)}{(\alpha^2 - 3\alpha + 2)s^2 + (8 - 2\alpha^2)s + (\alpha^2 + 3\alpha + 2)} \quad (2.8)$$

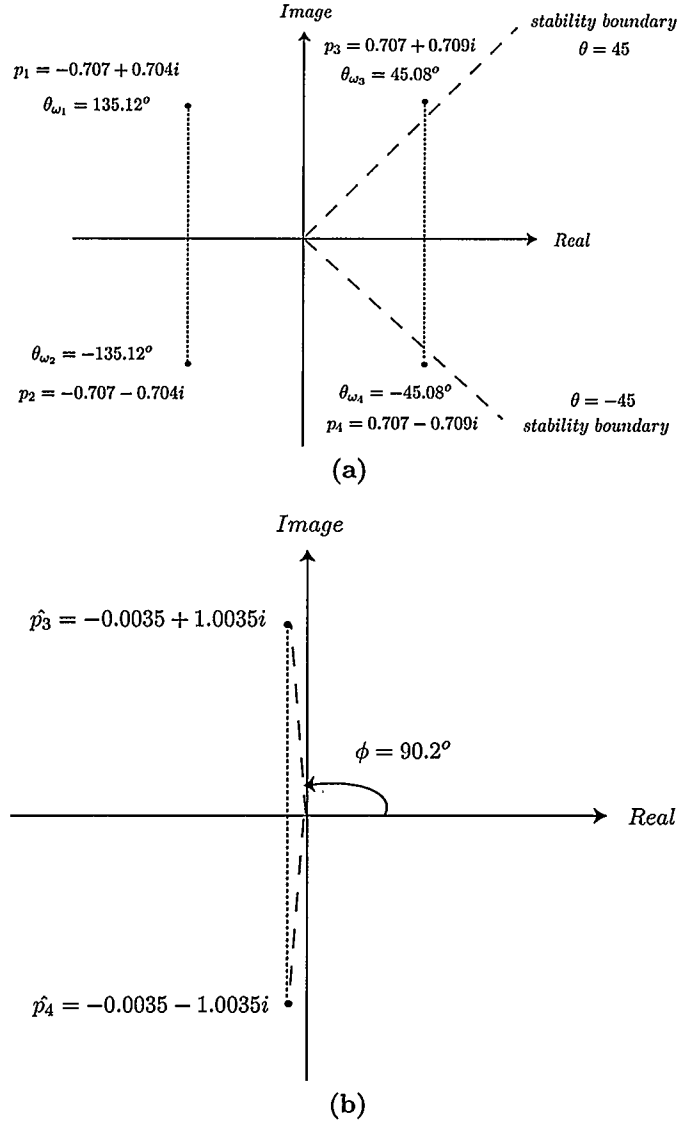


**Figure 2.9:** Roots of the transfer function (1.5) with  $\alpha = 0.5$ ,  $k_1 = 1$ ,  $a = 0.01$  and  $b = 1$  in (a)  $W$ -plane and (b)  $s$ -plane.

which is discussed in more detail in section 3.2.2. Substituting (2.8) in (1.5) yields a fourth order transfer function for Type I FDNR-based filter which can be written in the form

$$H_I(\hat{s}) = \hat{k}_1 \frac{s^2 + \hat{a}s + \hat{b}}{s^4 + \hat{c}s^3 + \hat{d}s^2 + \hat{e}s + \hat{f}} \quad (2.9)$$

where  $\hat{k}_1 = \frac{\alpha^2 + 3\alpha + 2}{\alpha^2 - 3\alpha + 2}$ ,  $\hat{a} = 8 - 2\alpha^2$ ,  $\hat{b} = \alpha^2 - 3\alpha + 2$ ,  $\hat{c} = 8 - 2\alpha^2$ ,  $\hat{d} = (a+b+1)\alpha^2 + 3(a-b+1)\alpha + 2(a+b+1)$ ,  $\hat{e} = (a+b)(8 - 2\alpha^2)$  and  $\hat{f} = (a+b)\alpha^2 + 3(b-a)\alpha + 2(a+b)$ . Figure

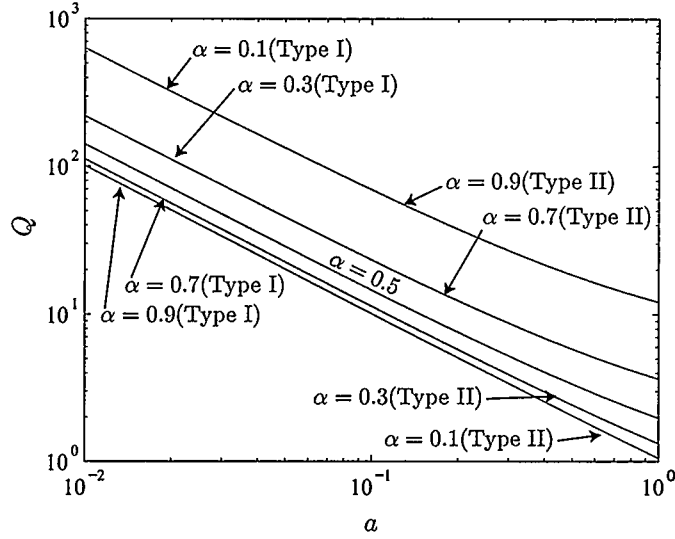


**Figure 2.10:** Quality factor versus  $a$  at  $b = 1$  for various values of  $\alpha$  for Type I and Type II transfer functions in (1.5) and (1.7).

2.11 shows the step response of the Type I FDNR-based filter in (1.5) at  $a = 0.2$ ,  $b = 1$  and  $\alpha = 0.5$ .

### 2.1.2 Type II Inductor-Based Asymmetric-Slope Band-pass Filter

For the Type II inductor-based filter governed by (1.7) the magnitude and phase functions are respectively given by

$$|H_{III}(j\omega)| = \frac{k_3}{\sqrt{1 + 2x \cos((1 + \alpha) \pi/2) + x^2}} \quad (2.10a)$$

$$\angle H_{III}(j\omega) = \frac{(1 + \alpha) \pi}{2} - \tan^{-1} \frac{\sin((1 + \alpha) \pi/2)}{x + \cos((1 + \alpha) \pi/2)} \quad (2.10b)$$

where  $x = (b - \omega^2)/a\omega^{1+\alpha}$ . The center frequency  $\omega_o$  at which the magnitude response has its maximum is given by

$$\omega_o = e^{y_3/(1+\alpha)} \quad (2.11)$$

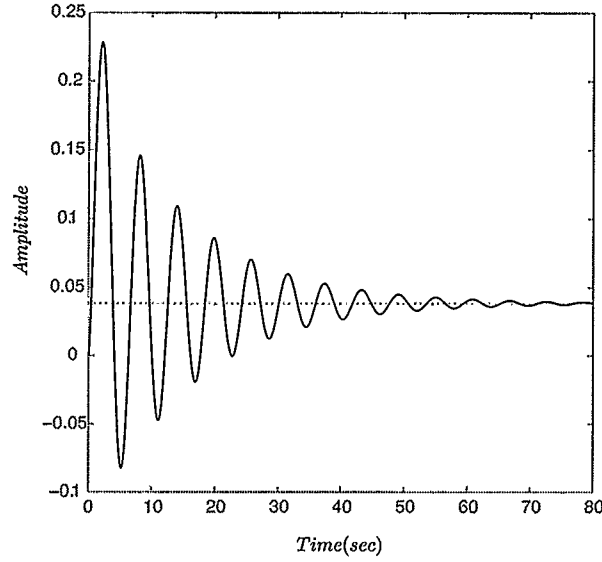


**Figure 2.11:** Step response of the Type I FDNR based filter in (1.5) at  $a = 0.2$ ,  $b = 1$  and  $\alpha = 0.5$ .

where  $y_3$  is a root of the equation

$$2y + (1 + \alpha) \left[ y - \ln \left( be^y + ae^{2y} \cos \frac{(1 + \alpha)\pi}{2} \right) \right] = 0 \quad (2.12)$$

which can also be found numerically. Similarly for  $a \ll b$ , it can be shown that  $\omega_o \approx \sqrt{b}$  for the Type II inductor-based filter. Figure 2.12 shows the magnitude and phase responses of the Type II inductor-based filter for  $a = 0.01$  and  $b = 1$  with  $k_3 = 1$ . It is worth noting that the transfer function in (1.7) approaches the normal integer-order band-pass transfer function for  $\alpha \rightarrow 0$ .

The poles in the  $W$ -plane can be obtained by solving the equation  $W^{2/\alpha} + aW^{\frac{1+\alpha}{\alpha}} + b = 0$ . Note that (2.12) is identical to (2.3) except that  $\alpha$  is replaced by  $1 + \alpha$ . Likewise the approximate relationship for  $Q$  is given as

$$\frac{1}{Q} \approx (1 - \alpha) \cdot \left[ \frac{a}{b^{0.5(1+\alpha)}} \right]^{0.8686} \quad (2.13)$$

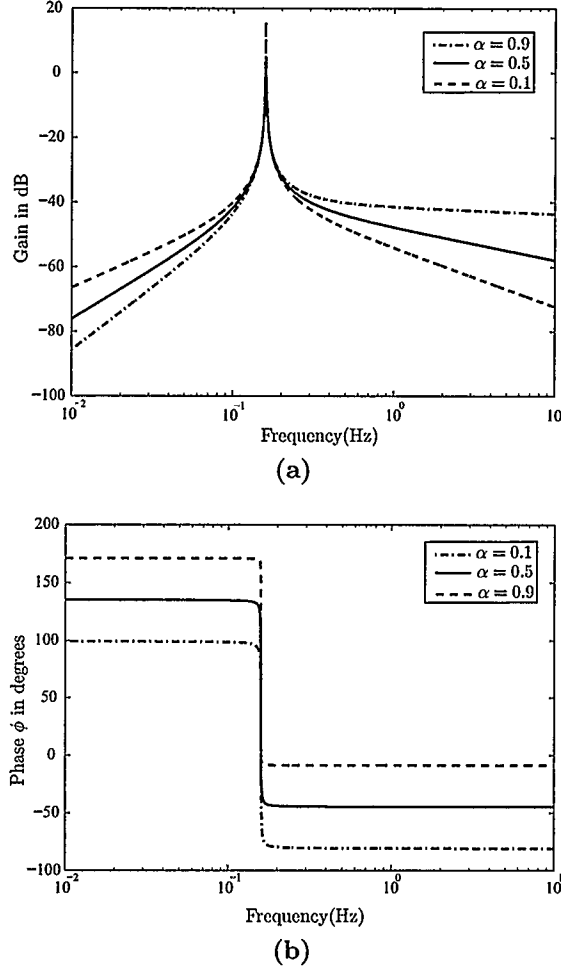


**Figure 2.12:** Magnitude and phase responses of the proposed Type II inductor-based asymmetric-slope band-pass filter in (1.7) to various values of  $\alpha$ .

which can be obtained from (2.7) by replacing  $\alpha$  with  $1 - \alpha$ . The implication of this is that the curves of Figure (2.10) can be used for the Type II inductor-based governed by (1.7) realization if for identical  $a$  and  $b$ ,  $\alpha$  is replaced by  $1 - \alpha$ . To illustrate an example the  $Q$  value for a Type II inductor-based filter with given  $a$  and  $b$  and  $\alpha = 0.3$  can be found by examining the Type I FDNR-based curve for the same  $a$  and  $b$  but with  $\alpha = 0.7$ . Note that for  $\alpha = 0.5$  the quality factors for both Type I FDNR-based and Type II inductor-based realizations are the same. For the Type II inductor-based filter, Figure (2.10) follows the reverse trend of the Type I FDNR-based filter. That is for a given  $a$ , large  $Q$ 's are obtained for increasing  $\alpha$ . For both Type I FDNR-based

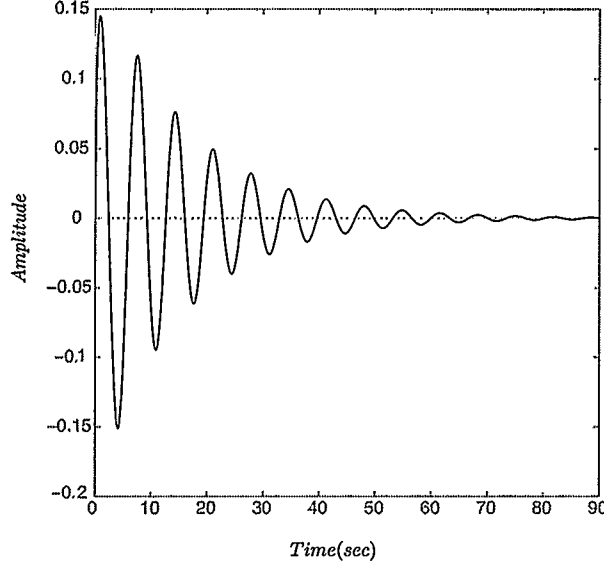


**Figure 2.13:** Step response of the Type II inductor based filter in (1.7) at  $a = 0.2$ ,  $b = 1$  and  $\alpha = 0.5$ .

and Type II inductor-based filters in general and for a given  $\alpha$ , large  $Q$ 's are obtained by ensuring that  $a \ll b$ .

Finally, the step response of the filter can be obtained by substituting for the non-integer Laplacian operator ( $s^\alpha$ ) with the integer order approximation in (2.8). Substituting (2.8) in (1.7) yields a fourth order transfer function for Type II inductor-based filter which can be written in the form

$$H_{III}^{\hat{}}(s) = k_{III}^{\hat{}} \frac{s(s^2 + \hat{a}s + \hat{b})}{s^4 + \hat{c}s^3 + \hat{d}s^2 + \hat{e}s + \hat{f}} \quad (2.14)$$

where  $k_{III}^{\hat{}} = \frac{\alpha^2 + 3\alpha + 2}{\alpha^2 - 3\alpha + 2}$ ,  $\hat{a} = 8 - 2\alpha^2$ ,  $\hat{b} = \alpha^2 - 3\alpha + 2$ ,  $\hat{c} = (a - 2)\alpha^2 + 3a\alpha + 2(a + 4)$ ,  $\hat{d} = (b - 2a + 1)\alpha^2 + 3(1 - b)$ ,  $\hat{e} = (a - 2b)\alpha^2 - 3a\alpha + 2(a + 4b)$  and  $\hat{f} = b(\alpha^2 + 3\alpha + 2)$ . Figure 2.13 shows the step response of the Type II inductor-based filter in (1.7) at  $a = 0.2$ ,  $b = 1$  and  $\alpha = 0.5$ .

### 2.1.3 Type I Inductor-Based Asymmetric-Slope Band-Pass Filter

The general magnitude and phase responses for the Type I inductor-based filter governed by (1.6) are given by

$$|H_{II}(j\omega)| = \frac{k_2}{\sqrt{1 + 2x \cos((1 - \alpha)\pi/2) + x^2}} \quad (2.15a)$$

$$\angle H_{II}(j\omega) = \frac{(1 - \alpha)\pi}{2} - \tan^{-1} \frac{\sin((1 - \alpha)\pi/2)}{x + \cos((1 - \alpha)\pi/2)} \quad (2.15b)$$

where  $x = (b - \omega^2)/a\omega^{(1-\alpha)}$ . The frequency at which the magnitude response has its maximum is

$$\omega_o = e^{y_2} \quad (2.16)$$

where  $y_2$  is a root of the equation

$$y(1 - \alpha) + \ln \left( -\frac{a \sin(\frac{\alpha\pi}{2})}{b - e^{2y}} \right) = 0 \quad (2.17)$$

which can be found numerically. For  $a \ll b$ , it can be easily shown that  $\omega_o \approx \sqrt{b}$ . Figure 2.14 shows the magnitude and phase responses of the Type I inductor-based filter for  $a = 0.01$  and  $b = 1$  with  $k_2 = 1$ . Normal second-order band-pass filter transfer function can be obtained from the transfer function in (1.6) for  $\alpha \rightarrow 0$ .

For this Type of filter the poles in the  $W$ -plane can be found by solving the equation  $W^{2/\alpha} + aW^{1-\alpha} + b = 0$ . For fixed values of  $a$  and  $b$ , the quality factor gets larger when  $\alpha$  increases. Figure 2.15 shows the values of  $Q$  versus  $a$  when  $b = 1$  for various values of  $\alpha$ . Figure 2.15 reveals that large  $Q$  values for the Type I inductor-based filter can be obtained for large  $\alpha$  and small values of  $a$  whereas large  $Q$  values for the Type I FDNR based filter in Figure 2.10 can be obtained for small values of  $a$  and  $\alpha$ . Numerically, the following approximate relationship was found for the Type I

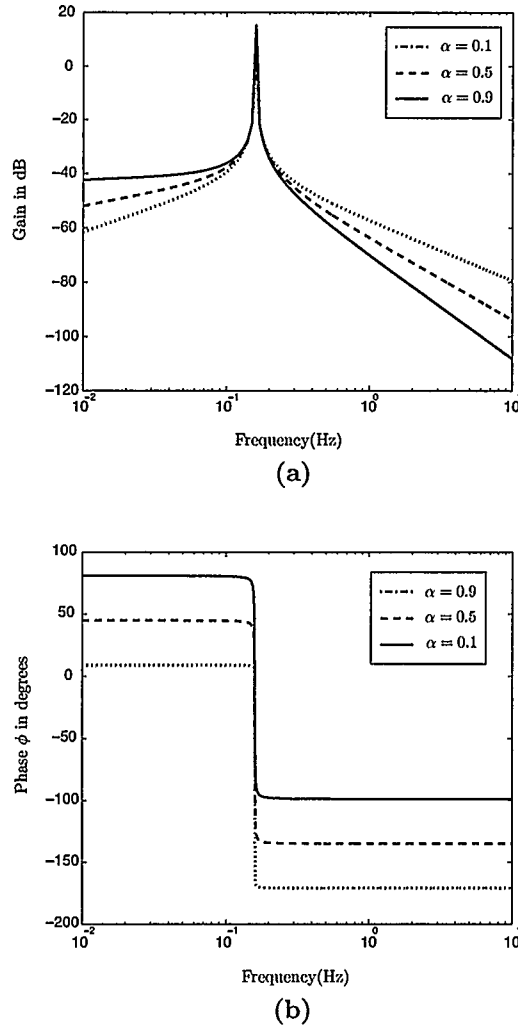


**Figure 2.14:** Magnitude and phase responses of the proposed Type I inductor-based asymmetric-slope band-pass filter in (1.6) to various values of  $\alpha$ .

inductor-based filter response,

$$\frac{1}{Q} \approx (1 - \alpha) \cdot \left[ \frac{a}{b^{0.5(1+\alpha)}} \right]^{0.8686} \quad (2.18)$$

which reveals that for given  $a$ ,  $b$  and  $\alpha$ , the quality factors of Type I and Type II inductor based transfer functions in (1.6) and (1.7) are the same and can be calculated using the equation (2.18).

It is to be noted that the step response of the Type I FDNR-based filter in (2.9)

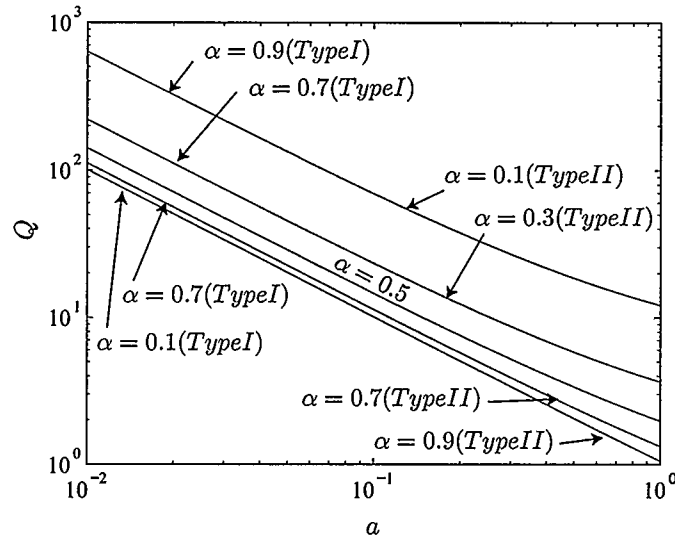


**Figure 2.15:** Quality factor versus  $a$  at  $b = 1$  for various values of  $\alpha$  for Type I inductor-based and Type II FDNR-based realizations.

can be used for the Type I inductor-based filter if for the identical  $a$  and  $b$ ,  $\alpha$  is replaced by  $1 - \alpha$ . Therefore, Figure 2.11 shows the step response of the Type I inductor-based filter in (1.6) at  $a = 0.2$ ,  $b = 1$  and  $\alpha = 0.5$ .

#### 2.1.4 Type II FDNR-Based Asymmetric-Slope Band-Pass Filter

Finally for the Type II FDNR-based design governed by (1.8) it can be shown that the magnitude and phase responses are respectively given by

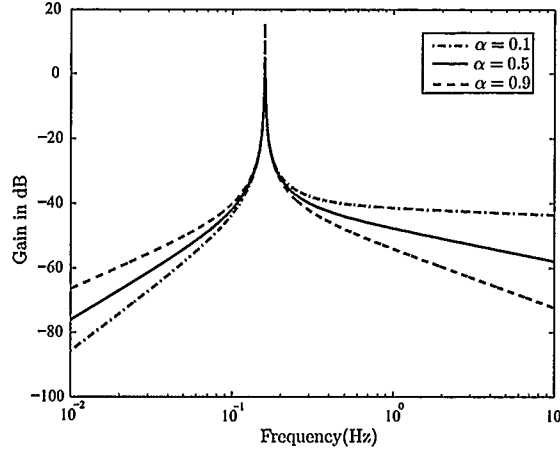
$$|H_{IV}(j\omega)| = \frac{k_4}{\sqrt{1 + 2x \cos((2 - \alpha)\pi/2) + x^2}} \quad (2.19a)$$

$$\angle H_{IV}(j\omega) = \frac{(2 - \alpha)\pi}{2} - \tan^{-1} \frac{\sin((2 - \alpha)\pi/2)}{x + \cos((2 - \alpha)\pi/2)} \quad (2.19b)$$

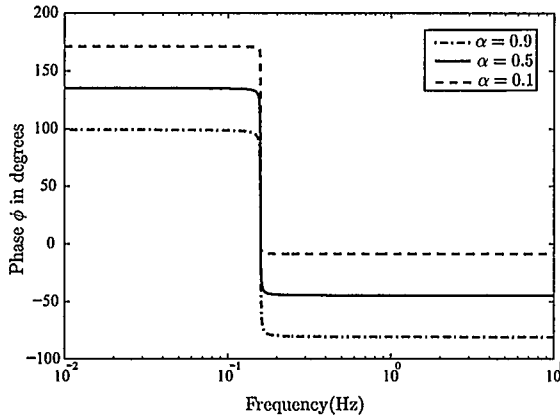
where  $x = (b - \omega^2)/a\omega^{2-\alpha}$ . The peak frequency is given by

$$\omega_o = e^{y_4} \quad (2.20)$$

where  $y_4$  is a root of the equation



(a)



(b)

**Figure 2.16:** Magnitude and phase responses of the proposed Type II FDNR-based asymmetric-slope band-pass filter in (1.8) to various values of  $\alpha$ .

$$y(2 - \alpha) + \ln \left( -\frac{a \sin\left(\frac{(\alpha-1)\pi}{2}\right)}{b - e^{2y}} \right) = 0 \quad (2.21)$$

which can also be found numerically. Note that (2.21) is identical to (2.17) except that  $\alpha$  is replaced by  $\alpha - 1$ . For  $a \ll b$ , it can be easily shown that  $\omega_o \approx \sqrt{b}$ . Figure 2.16 shows the magnitude and phase responses of the Type II FDNR-based filter for  $a = 0.01$  and  $b = 1$  with  $k_4 = 1$ . Normal second-order band-pass filter transfer function can be obtained from the transfer function in (1.8) for  $\alpha = 1$ . The poles can be found by solving the equation  $W^{\frac{2}{\alpha}} + aW^{\frac{2-\alpha}{\alpha}} + b = 0$  in the  $W$ -plane and the

approximate relationship for  $Q$  is given as

$$\frac{1}{Q} \approx \alpha \cdot \left[ \frac{a}{b^{(1-0.5\alpha)}} \right]^{0.8686} \quad (2.22)$$

which is equivalent to (2.7). In other words, Type I and Type II FDNR-based transfer functions in (1.5) and (1.8) have the same quality factor for given  $a$ ,  $b$  and  $\alpha$ .

The quality factor for Type II FDNR-based filter versus  $a$  at  $b = 1$  for different values of  $\alpha$  is shown in Figure 2.15 as well. It is clear that the curves for Type I inductor-based filter can be used for Type II FDNR-based realization if  $\alpha$  is replaced by  $1 - \alpha$ . As an example, for given  $a$  and  $b$  and  $\alpha = 0.9$ , Type II FDNR-based quality factor can be obtained by examining the Type I inductor-based curve for the same  $a$  and  $b$  but with  $\alpha = 0.1$ . Generally speaking, for Type I inductor-based realization, large  $Q$  values are obtained for large  $\alpha$  and small values of  $a$  and Type II FDNR-based filter obtains high quality factor for small values of  $a$  and  $\alpha$ .

It is also clear from Figures 2.10 and 2.15 that for a given  $\alpha$  large quality factors can be obtained for  $a \ll b$  for both Type I and Type II filters.

Finally it is worth noting that the step response of the Type II inductor-based filter in (2.14) can be used for the Type II FDNR-based filter if for the identical  $a$  and  $b$ ,  $\alpha$  is replaced by  $1 - \alpha$ . Therefore, Figure 2.13 shows the step response of the Type II FDNR-based filter at  $a = 0.2$ ,  $b = 1$  and  $\alpha = 0.5$ .

## 2.2 Possible Designs

### 2.2.1 Type I Filter Realizations

The circuits of Figures 2.4 and 2.5 can be easily realized actively by appropriately replacing the FDNR and the inductor by their active realizations which can employ operational amplifiers (opamps) [1, 2, 26, 27], OTAs [6, 28], current conveyors [29–32], Active-R [33, 34] and even hybrid realizations [35, 36]. Two circuits are proposed for

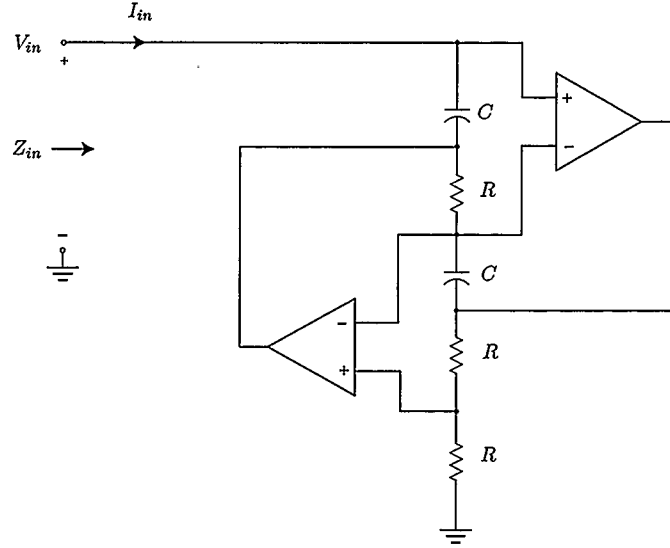


**Figure 2.17:** Grounded FDNR based on Antonio's General Impedance Converter, whose input impedance is  $Z_{in} = 1/RC^2s^2$  used in Type I FDNR-based asymmetric-slope band-pass filter.

the Type I realization governed by the transfer function in (1.5) in Figures 2.18(a) and (b). Figure 2.18(a) employs a General Impedance Converter (GIC) based FDNR, whose input impedance is  $Z_i = 1/RC^2s^2$  (see Figure 2.17), connected to the passive filter section which employs the resistor  $R_1$  and the fractional-order capacitor  $C_\alpha$  [1, 2]<sup>1</sup>. It can be shown that this circuit realizes the transfer function in (1.5) with  $k_1 = 2$ ,  $a = C_\alpha/RC^2$  and  $b = 1/R_1RC^2$ . Likewise, the circuit shown in Figure 2.18(b), which employs a multiple amplifier biquad (MAB), can also realize the transfer function in (1.5) with  $k_1 = -R_6/R_5$ ,  $a = \frac{\tau_\alpha[1+(R_3/R_4)]}{\tau_1\tau_2[1+(R_6/R_5)]}$  and  $b = \frac{R_3/R_4}{\tau_1\tau_2}$  where  $\tau_1 = R_1C_1$ ,  $\tau_2 = R_2C_2$  and  $\tau_\alpha = R_\alpha C_\alpha$ . The output in this case is taken as  $V_{out}$  while if the output is taken as  $V_{out1}$  (see Figure 2.18(b)),  $k_1$  in this case would be equal to  $-R_6R_2C_2/R_5R_\alpha C_\alpha$  with  $a$  and  $b$  staying the same and the numerator term in (1.5) changing from  $s^\alpha$  to  $s$ . This means that while the output  $V_{out}$  represents an asymmetric filter, the output taken at  $V_{out1}$  will represent symmetric filter characteristics.

<sup>1</sup>The FDNR is a standard circuit element in filter design whose impedance is negatively and inversely proportional to the square of the frequency [24], [37].

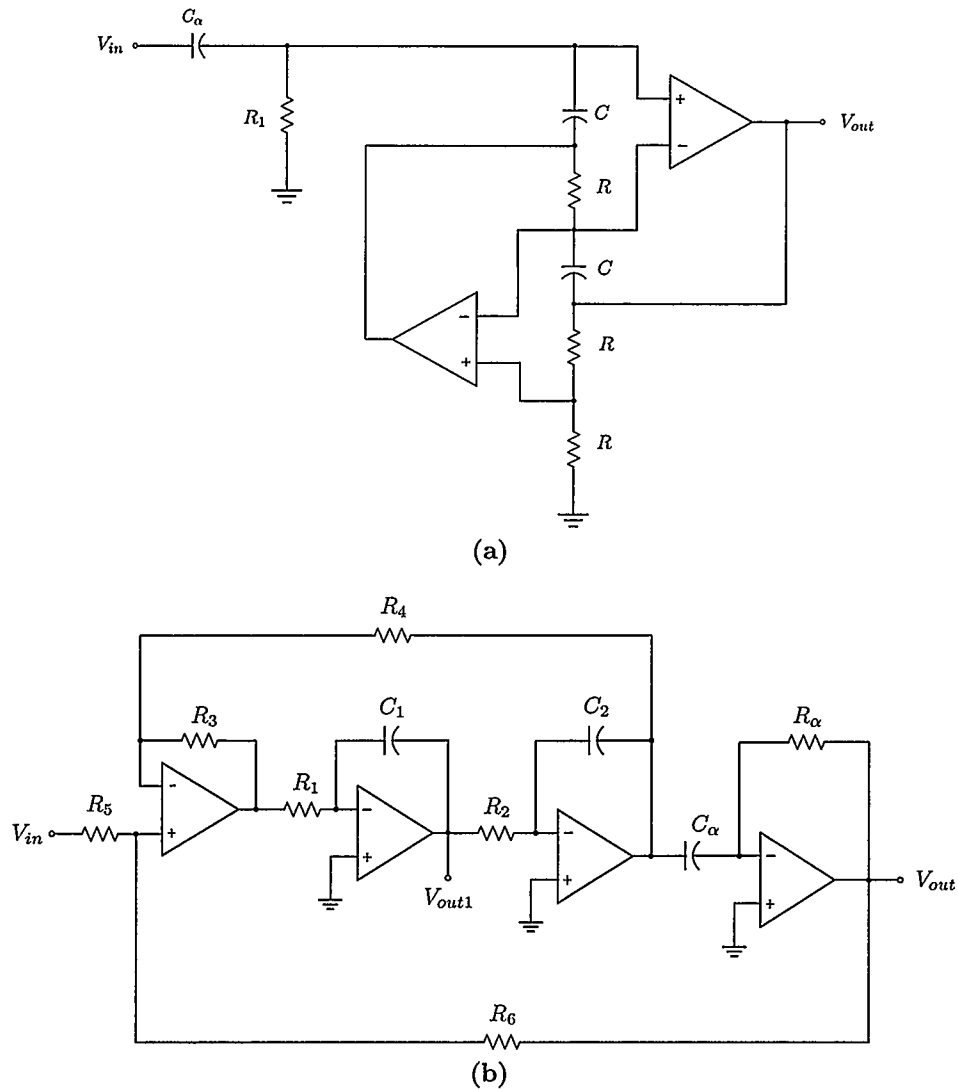


**Figure 2.18:** Possible realizations of the Type I asymmetric-slope band-pass filter realizing the transfer function in (1.5); (a) using an FDNR and (b) using a multiple amplifier biquad.

The circuit shown in Figure 2.20 realizes the transfer function in (1.6) with  $k_2 = 1$ ,  $a = R_1/(RR_2R_3C_1C_\alpha)$  and  $b = R_1/(RR_2R_3CC_1)$ . The circuit employs a floating inductor based on Riordan technique whose impedance is  $Z_i = RR_2R_3C_1s/R_1$  as shown in Figure 2.19 [38, 39].

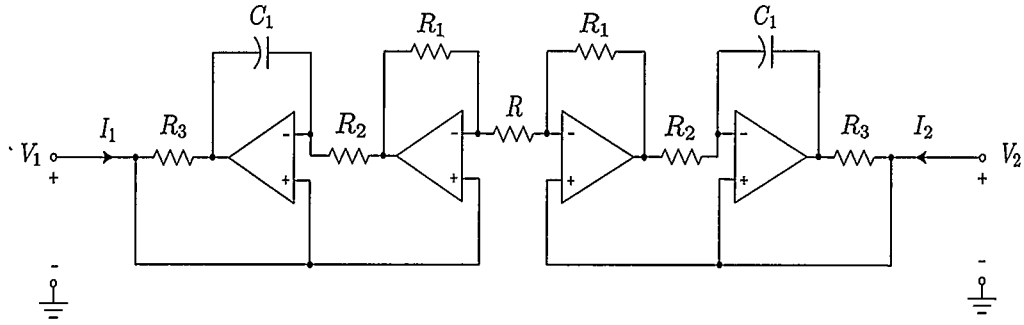


**Figure 2.19:** Floating inductor based on Riordan technique, whose input impedance is  $Z_i = RR_2R_3C_1s/R_1$  used in Type I inductor-based asymmetric-slope band-pass filter.

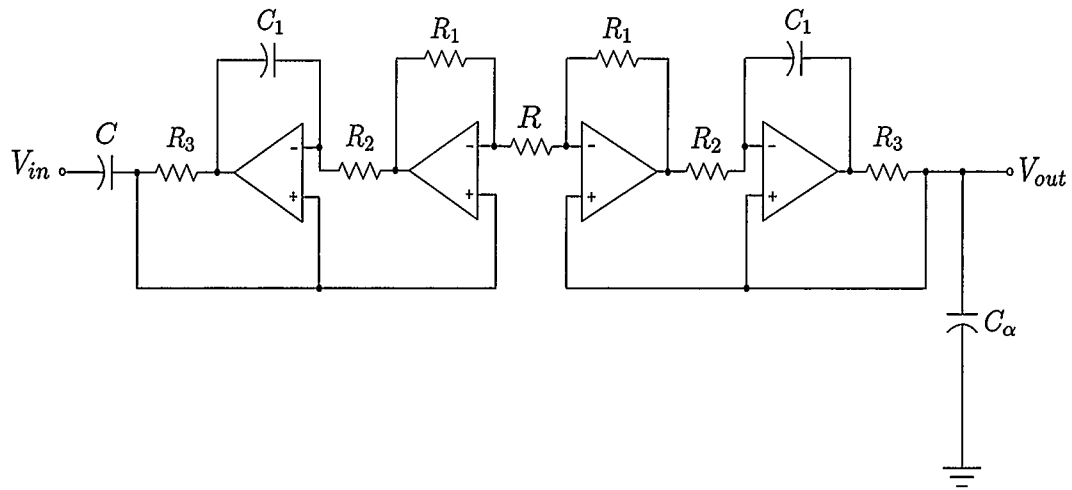


**Figure 2.20:** Possible realization of the Type I inductor-based asymmetric-slope band-pass filter realizing the transfer function in (1.6).

## 2.2.2 Type II Filter Realizations

Type II realizations governed by the transfer function in (1.7) using a grounded inductor of the Antonio GIC variety, whose impedance is  $Z_{in} = R_1R_2Cs$  (see Figure 2.21) and MAB variety are shown in Figure 2.22 with  $k_3 = 2$ ,  $a = C_\alpha/C_1$  and  $b = 1/R_1R_2CC_1$  for the grounded inductor version of Figure 2.22(a) and  $k_3 = \left(1 + \frac{R_4}{R_3} + \frac{R_4}{R_5}\right)$ ,  $a = \frac{R_3}{R_4} \frac{\tau_\alpha}{\tau_1}$ ,  $b = \frac{R_3/R_5}{\tau_1\tau_2}$  where  $\tau_1 = R_1C_1$ ,  $\tau_2 = R_2C_2$  and  $\tau_\alpha = R_\alpha C_\alpha$  for the MAB version of Figure 2.22(b). As in the previous Type I case, an additional symmetric band-pass filter characteristic is available at  $V_{out1}$  with  $k_3 =$

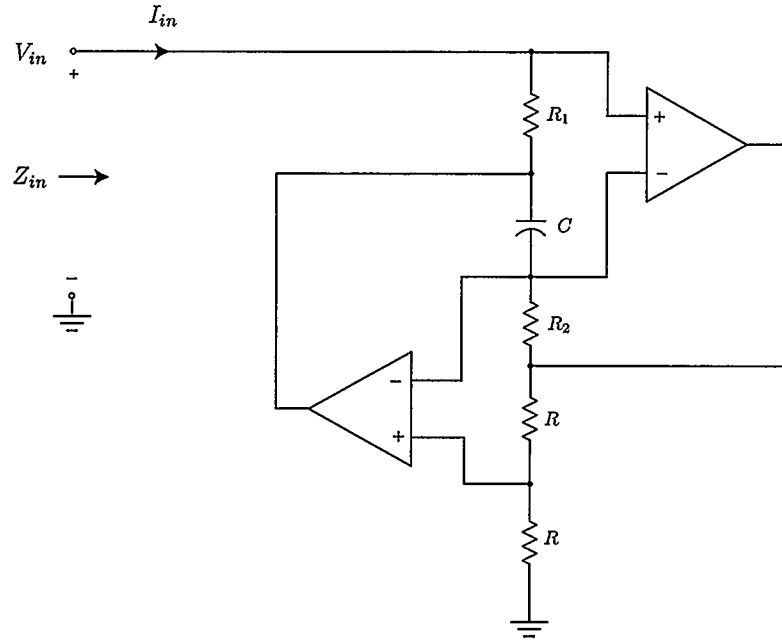
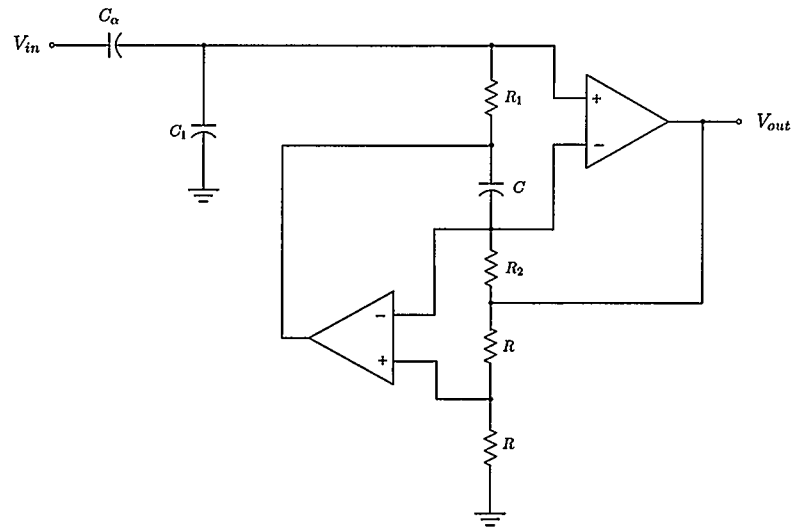


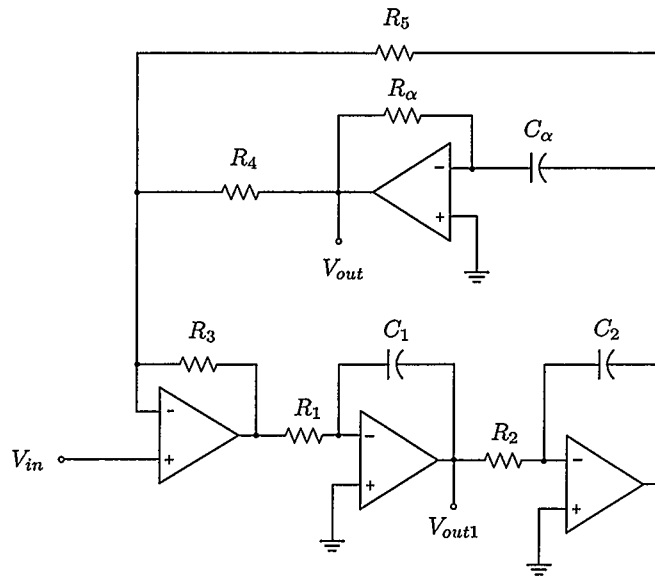
**Figure 2.21:** Grounded inductor based on Antonio's General Impedance Converter, whose input impedance is  $Z_{in} = R_1 R_2 C s$  used in Type II inductor-based asymmetric-slope band-pass filter.

$\frac{1}{\tau_1 \tau_\alpha} \left( 1 + \frac{R_4}{R_3} + \frac{R_4}{R_5} \right)$ ,  $a$  and  $b$  remaining unchanged, and the numerator term in (1.7) changing from  $s^{1+\alpha}$  to  $s$ . Another design example with different type of grounded inductor is proposed in Appendix B.

Type II FDNR-based asymmetric-slope band-pass filter using a floating FDNR, whose impedance is  $Z_i = C_1 C_2 R_1 R_2 / (R_3 s^2)$  (see Figure 2.23(a)) is shown in Figure 2.24 [40]. Note that for practical purposes each  $CCII-$  can be replaced by two  $CCII+$  s as shown in Figure 2.23(b). The circuit realizes the transfer function in (1.8) with  $k_4 = 1$ ,  $a = 1/RC_\alpha$  and  $b = R_3/(RR_1R_2C_1C_2)$ .



(a)



(b)

**Figure 2.22:** Possible realizations of the Type II asymmetric-slope band-pass filter realizing the transfer function in (1.7); (a) using an inductor and (b) using a multiple amplifier biquad.

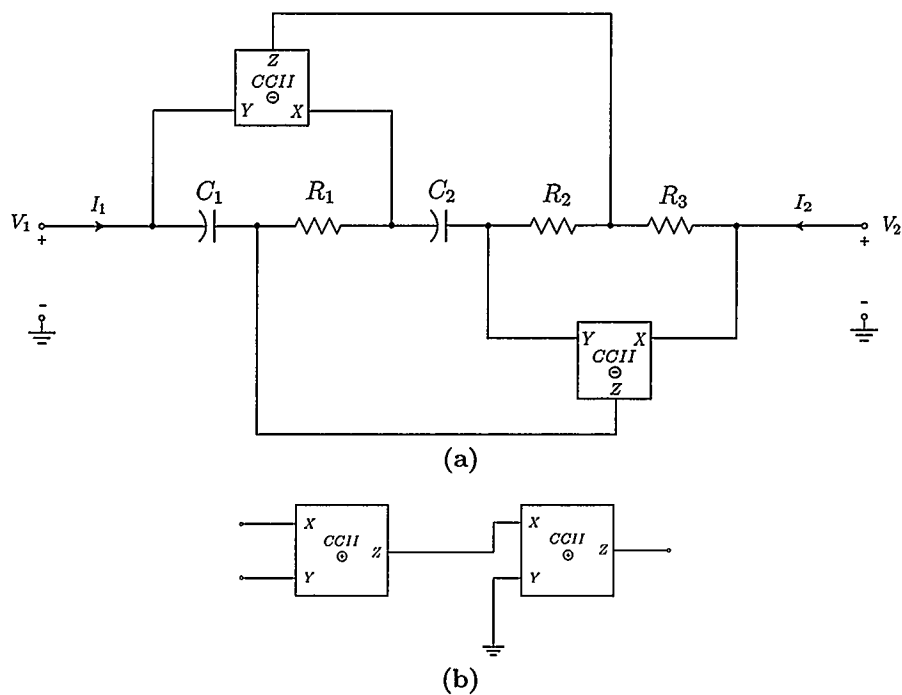


**Figure 2.23:** (a) Floating FDNR using current conveyors, whose input impedance is  $Z_i = C_1 C_2 R_1 R_2 / (R_3 s^2)$ . (b)  $CCII-$  is realized using two  $CCII+$ s.

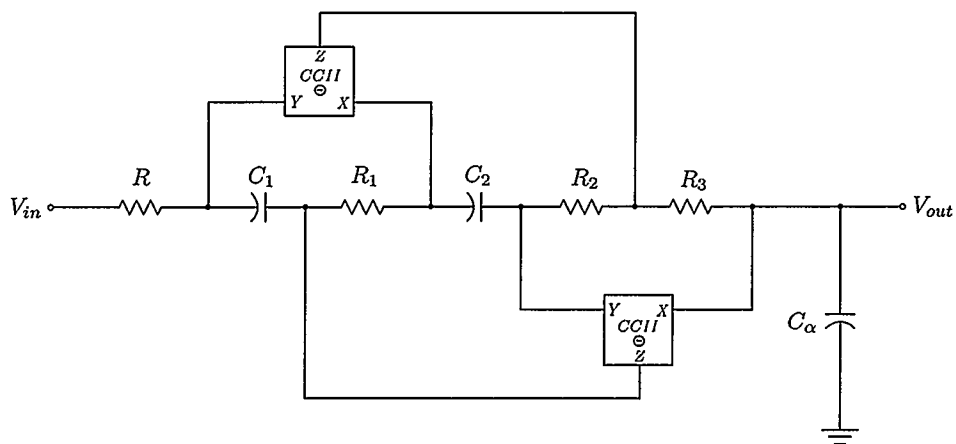


**Figure 2.24:** Possible realization of the Type II FDNR-based asymmetric-slope band-pass filter realizing the transfer function in (1.8).

## CHAPTER 3

### Simulation and Experimental Results

#### 3.1 Using Discrete Components

##### 3.1.1 Type I Filters

The Type I asymmetric-slope band-pass filters in Figures 2.18 and 2.20 were simulated in SPICE using LT1364 opamps (rated bandwidth 70MHz) biased with  $\pm 15V$  supplies. Carlson's method [7] was used to simulate the fractional-order capacitor  $C_\alpha$  having  $C = 1\mu F$  and  $\alpha = 0.5$ , as shown in Figure 3.1. The approximated model of the fractional capacitor represents a self-similar  $RC$  tree structure [41]. Note that other approximations exist [42–44] some more optimal than others, but Carlson's method was chosen for its simplicity. Table 3.1 shows the values of capacitors and resistors used in the approximated model of fractional capacitor in Figure 3.1. The values of components were calculated such that  $C_\alpha$  has an operating range of  $100Hz-10kHz$ . Figure 3.2 shows the simulation results for the Type I FDNR-based circuit of Fig-

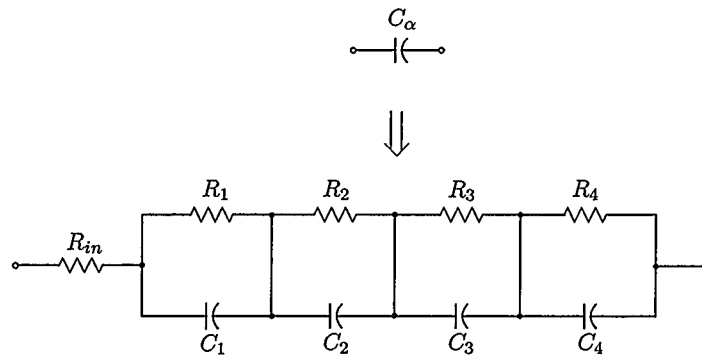
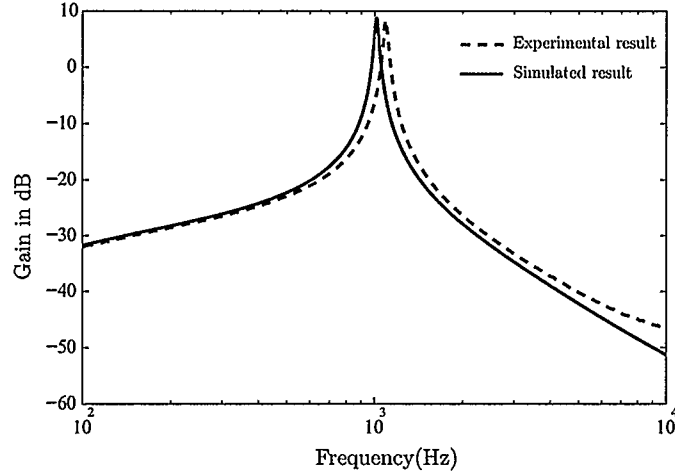


Figure 3.1: Approximation of  $C_\alpha$  based on Carlson's method.

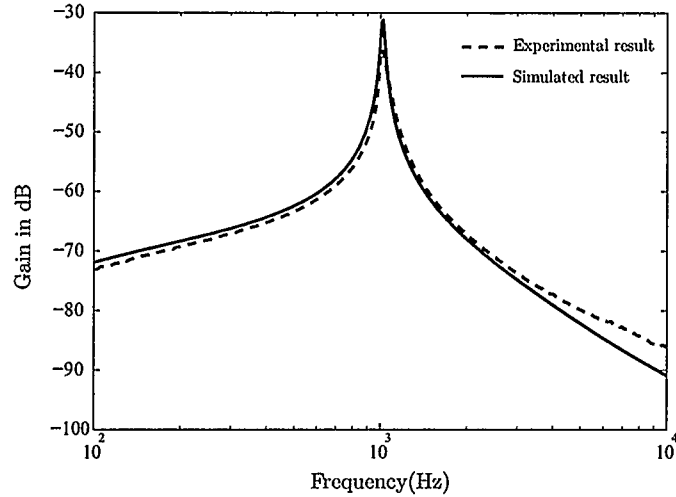
Variable	Value for SPICE simulation and experimental test
$R_{in}$	$1.4K\Omega$
$R_1$	$3.2K\Omega$
$R_2$	$4.77K\Omega$
$R_3$	$11.21K\Omega$
$R_4$	$92.97K\Omega$
$C_1$	$6.64nF$
$C_2$	$23.45nF$
$C_3$	$42.57nF$
$C_4$	$55.05nF$

**Table 3.1:** Values of components used in SPICE simulation and experimental test for  $C_\alpha = 1\mu F$ ,  $\alpha = 0.5$ .

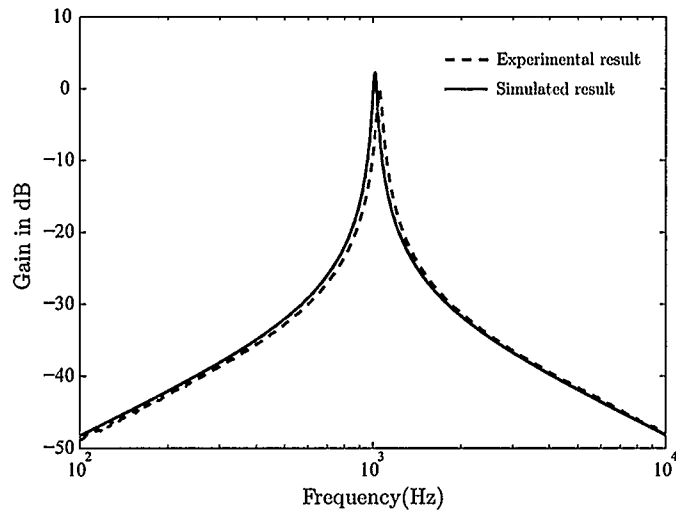


**Figure 3.2:** SPICE and experimental results of the Type I FDNR-based asymmetric-slope band-pass filter in Figure 2.18(a).

ure 2.18(a) taking  $R_1 = 531\Omega$ ,  $R = 4.7k\Omega$  and  $C = 0.1\mu F$  while Figures 3.3(a) and 3.3(b) show the results for the Type I MAB-based circuit of Figure 2.18(b) with  $R_1 = R_2 = 1.59k\Omega$ ,  $R_3 = R_4 = 1k\Omega$ ,  $R_5 = 5.1k\Omega$ ,  $R_6 = 100\Omega$ ,  $R_\alpha = 270\Omega$  and  $C_1 = C_2 = 0.1\mu F$ . Both circuits were designed to achieve a quality factor of 33 and a center frequency of  $f_o = 1kHz$ . The circuits were also constructed on breadboard and tested. Experimental results for the two circuits are also shown within Figures 3.2, 3.3(a) and 3.3(b). The slope at frequencies lower than  $f_o$  was measured as  $10 dB/dec$



(a)



(b)

**Figure 3.3:** SPICE and experimental results of the filter in Figure 2.18(b); (a) showing the asymmetrical output at  $V_{out}$  and (b) showing the symmetrical output at  $V_{out1}$ .

while it was measured as  $-30 \text{ dB/dec}$  at frequencies greater than  $f_o$  for both types of filters confirming the asymmetric nature of the band-pass filters and the accuracy of realizing Table 2.1(a). The measured  $(Q, f_o)$  for Type I FDNR based circuit were  $(31.65, 1.087 \text{ kHz})$  and they were measured  $(26.15, 1.051 \text{ kHz})$  for Type I MAB-based circuit, respectively. To confirm stability, the steady state transient response of the filter in Figure 2.18(a) is shown in Fig. 3.4.

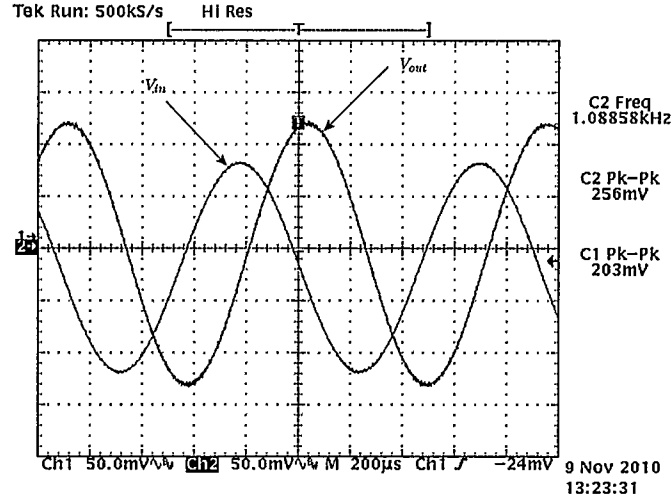


**Figure 3.4:** Measured transient response of the Type I band-pass filter in Figure 2.18(a) confirming stability at  $\alpha = 0.5$ .

The comparison between simulation and experimental results for Type I inductor-based asymmetric band-pass filter of Figure 2.20 taking  $R = 2k\Omega$ ,  $R_1 = 400\Omega$ ,  $R_2 = 4.48k\Omega$ ,  $R_3 = 5k\Omega$ ,  $C = 0.68nF$  and  $C_1 = 0.33\mu F$  is shown in Figure 3.5. The filter was designed to achieve a quality factor of 20 and a center frequency of  $f_o = 1kHz$ . The measured  $(Q, f_o)$  were respectively  $(16.52, 1.03kHz)$ . Also the measured slope at frequencies lower than  $f_o$  was  $10 dB/dec$  while it was  $-30 dB/dec$  at frequencies greater than  $f_o$  as expected from Table 2.1. The slight deviation from the SPICE simulations (see Figures 3.2 and 3.3) is attributed to the component tolerances and the two circuit topologies which are examined in Chapter 4. To confirm stability, the steady state transient response of the filter in Figure 2.20 is shown in Figure 3.6.

### 3.1.2 Type II Filters

Figure 3.7 shows the comparison between simulation and experimental results for the Type II inductor-based circuit of Figure 2.22(a) using  $R = R_1 = R_2 = 1k\Omega$ ,  $C = 0.1\mu F$  and  $C_1 = 0.215\mu F$  while the comparison between simulation and experimental results for the circuit of Figure 2.22(b) using  $R_1 = R_2 = 1.59k\Omega$ ,  $C_1 = C_2 = 0.1\mu F$ ,  $R_3 = R_4 = 1k\Omega$  and  $R_5 = 0.9k\Omega$  is shown in Figure 3.8. The measured  $(Q, f_o)$  results

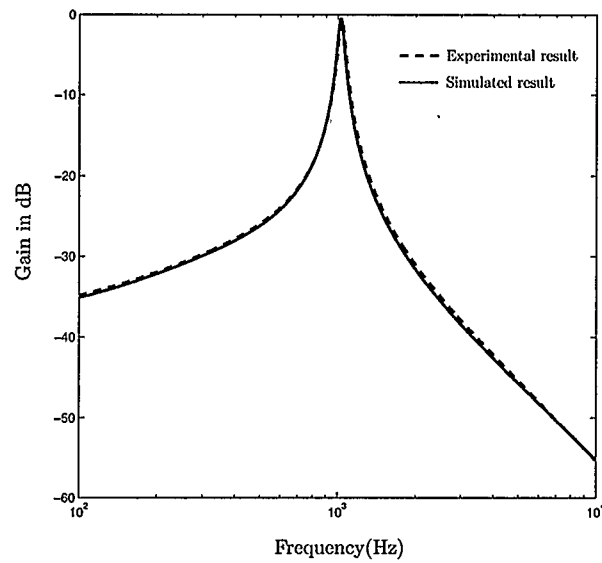


**Figure 3.5:** SPICE and experimental results of the Type I band-pass filter in Figure 2.20.

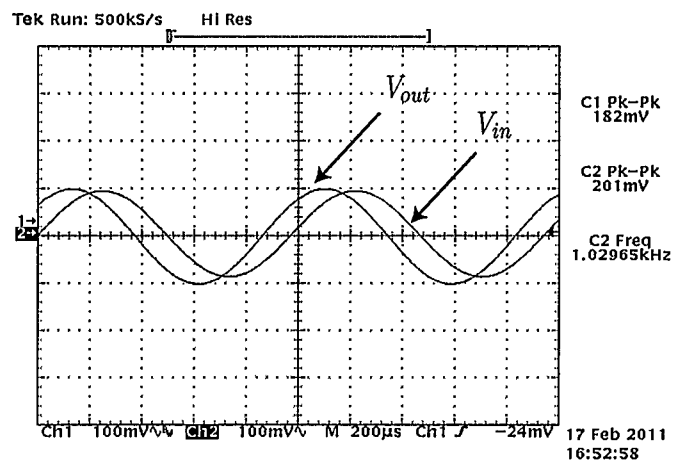


**Figure 3.6:** Measured transient response of the Type I band-pass filter in Figure 2.20 confirming stability at  $\alpha = 0.5$ .

for a designed  $Q = 25$  and  $f_o = 1.04\text{kHz}$  yielded a  $(20.1, 1.16\text{kHz})$  for the inductor based circuit and  $(19.75, 1.07\text{kHz})$  for the MAB based circuit. The measured slope at frequencies less than  $f_o$  was  $30\text{ dB/dec}$  while it was  $-10\text{ dB/dec}$  at frequencies greater than  $f_o$ . The steady state transient response of the filter in Figure 2.22(a) is shown in Figure 3.9.

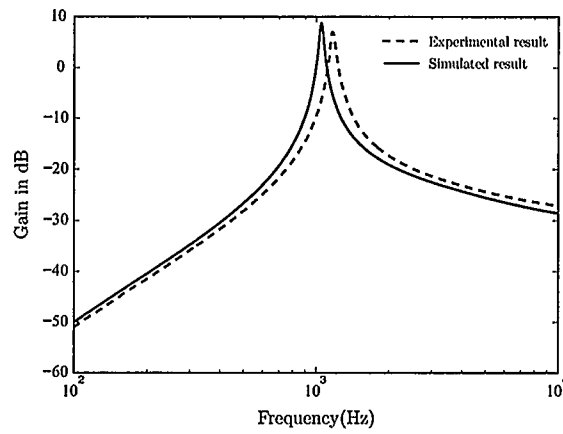


Figure 3.7: SPICE and experimental results of the filter in Figure 2.22(a).

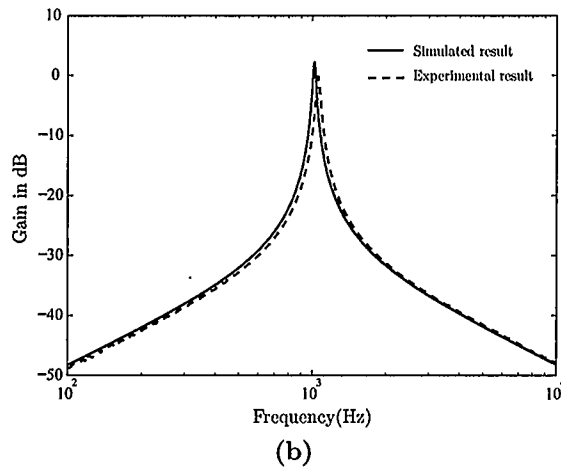
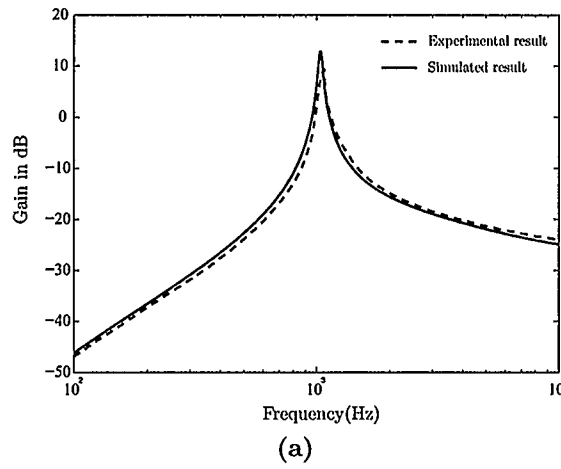
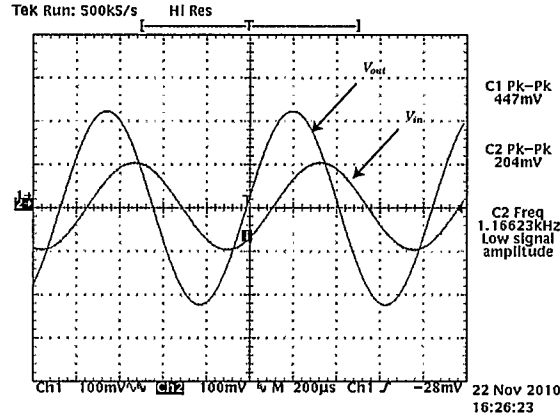


Figure 3.8: SPICE and experimental results of the filter in Figure 2.22(b); (a) showing the asymmetrical output at  $V_{out}$  and (b) showing the symmetrical output at  $V_{out1}$ .



**Figure 3.9:** Measured transient response of the Type II inductor-based band-pass filter in Fig. 2.22(a) for  $\alpha = 0.5$ .

Variable	Value for SPICE simulation and experimental test
$R_{in}$	$120\Omega$
$R_1$	$271\Omega$
$R_2$	$408\Omega$
$R_3$	$958\Omega$
$R_4$	$7.94K\Omega$
$C_1$	$7.77nF$
$C_2$	$27.4nF$
$C_3$	$49.8nF$
$C_4$	$64.4nF$

**Table 3.2:** Values of components used in SPICE simulation and experimental test for  $C_\alpha = 3.7\mu F$ ,  $\alpha = 0.5$ .

AD844 opamps (rated bandwidth 21MHz) were used to simulate Type II FDNR-based asymmetric-slope band-pass filter in Figure 2.24. The fractional-order capacitor  $C_\alpha$  having  $C_\alpha = 3.7\mu F$  and  $\alpha = 0.5$  was approximated by Carlson's method such that it has an operating range of  $1kHz - 100kHz$  [7]. Table 3.2 shows the values of resistors and capacitors used in Carlson's approximation. The comparison between simulation and experimental results for Type II FDNR-based asymmetric-slope band-pass filter of Figure 2.24 taking  $R = 14k\Omega$ ,  $R_1 = 8k\Omega$ ,  $R_2 = 8.2k\Omega$ ,  $R_3 = 40k\Omega$ ,  $C_1 = 4.7nF$  and  $C_2 = 2.2nF$  is shown in Figure 3.10. The filter was designed to achieve a quality

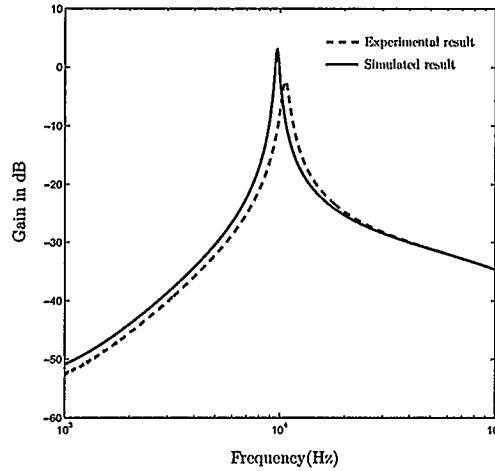


Figure 3.10: SPICE and experimental results of the filter in Figure 2.24.

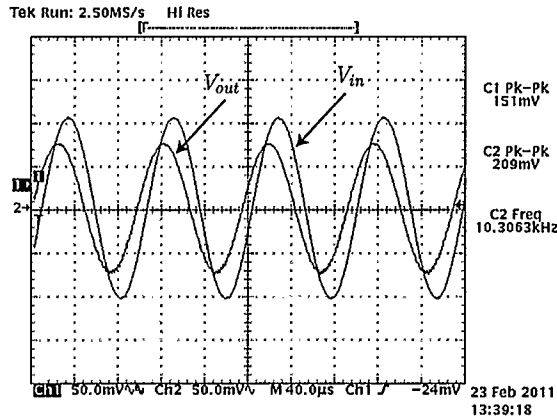


Figure 3.11: Measured transient response of the Type II FDNR-based band-pass filter in Figure 2.24 confirming stability at  $\alpha = 0.5$ .

factor of  $Q = 18$  and a center frequency of  $f_o = 10\text{kHz}$  and the measured  $(Q, f_o)$  were respectively  $(13.5, 10.52\text{kHz})$ . The slope at frequencies less than  $f_o$  was measured as  $30\text{ dB/dec}$  while it was measured as  $-10\text{ dB/dec}$  at frequencies greater than  $f_o$  in the operating range of  $C_\alpha$ . To confirm stability, the steady state transient response of the filter in Figure 2.24 is shown in Figure 3.11.

It is to be noted that because of the fractional differentiator circuit in the feedback loop of the MAB based circuits of Figures 2.18(b) and 2.22(b), at  $f_o$ , large signal

swings can be present at the outputs of the two lossless integrators. This results in the necessity to use small input signals for  $V_{in}$  to avoid the outputs of these lossless integrators being saturated. The MAB based circuit therefore should in general be driven by small input voltages. On the other hand the FDNR based circuits as well as the inductor based circuits in both types do not suffer from internal resonances at their nodes and are limited only by the maximum allowable differential voltage across the opamps input terminals.

Finally, it is also worth noting that the deviation in the  $Q$  and  $f_o$  is larger for the Type II circuit because of tolerances in addition to the fact that Type II filters responses are more susceptible to variations in the quality factor of the grounded inductor and floating FDNR in Figures 2.22(a) and 2.24. This point is discussed in more detail in Chapter 4.

## 3.2 FPAA realization

### 3.2.1 Field Programmable Analog Array Implementation

Field Programmable Analog Arrays (FPAA) offer a unique way to experimentally validate the functionality of analog design on the integrated circuit level. FPAA is an analog signal processor which allows complex analog circuits to be implemented in real time programmable Analog Signal Processors. These analog signal processors are designed to implement signal conditioning, filtering, summing, subtracting, data acquisition, closed-loop control, audio and other analog functions in a wide range of embedded systems. The AN231E04 device consists of a 2x2 matrix of fully Configurable Analog Blocks (CAMs), surrounded by programmable interconnect resources and analog input/output cells with active elements. The CAMs can be easily dropped in and wired together in the graphical design environment. Here, we use the proposed FPAA from Anadigm [45] based on fully differential switched capacitor building blocks running at a 4MHz clock. We use bilinear and biquadratic CAMs

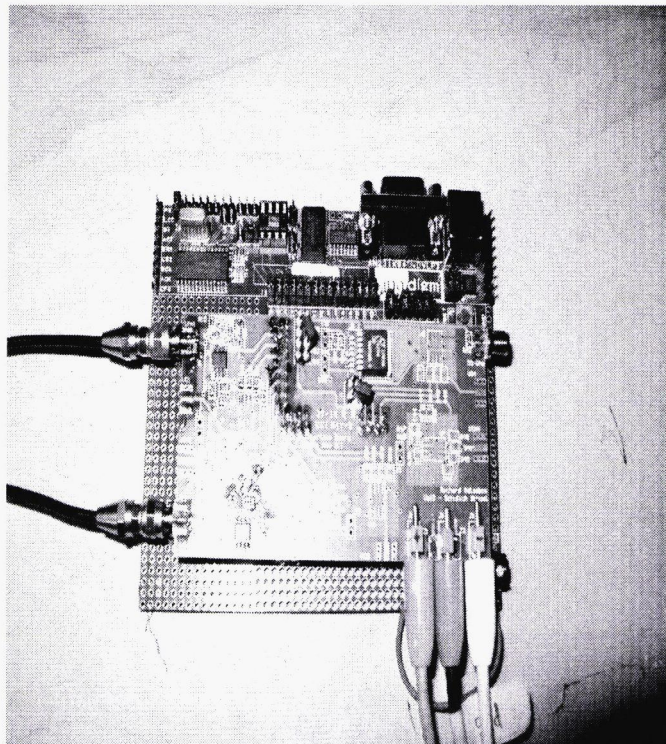


**Figure 3.12:** AN231E04 FPAA development kit from Anadigm.

to approximate the fractional order filters. Figure 3.12 shows the AN231E04 FPAA development kit from Anadigm.

### 3.2.2 FPAA Realization of Non-Integer Laplacian Operator

Using bilinear CAMs in FPAA we need to have the transfer function pole and zero frequencies. To use low-pass and band-pass biquads, quality factor and center frequency are needed as well. Since non-integer Laplacian operator  $s^\alpha$  cannot yet be physically realized, we substitute for  $s^\alpha$  with the second-order approximation introduced in [17] as

$$s^\alpha \approx \frac{cs^2 + ds + e}{es^2 + ds + c} \quad (3.1)$$

where  $c = \alpha^2 + 3\alpha + 2$ ,  $d = 8 - 2\alpha^2$  and  $e = \alpha^2 - 3\alpha + 2$ . The proposed approximation minimizes the magnitude error to less than 1dB over two decades. This point is discussed in more detail in Appendix A.

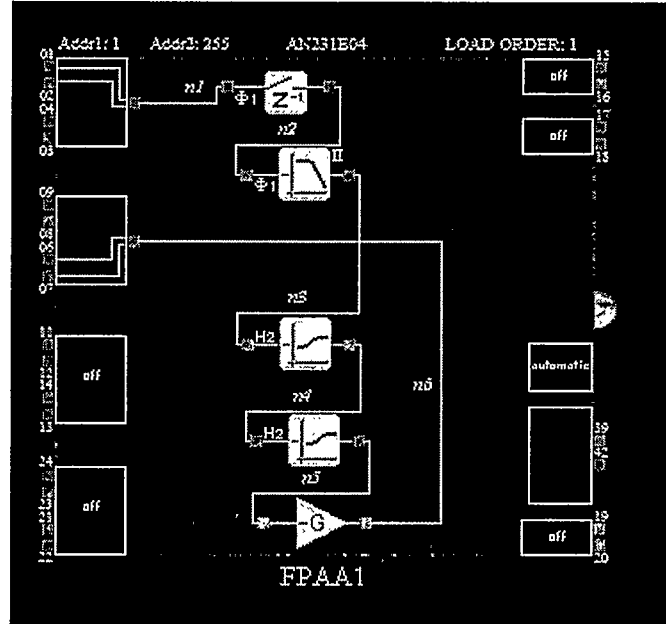


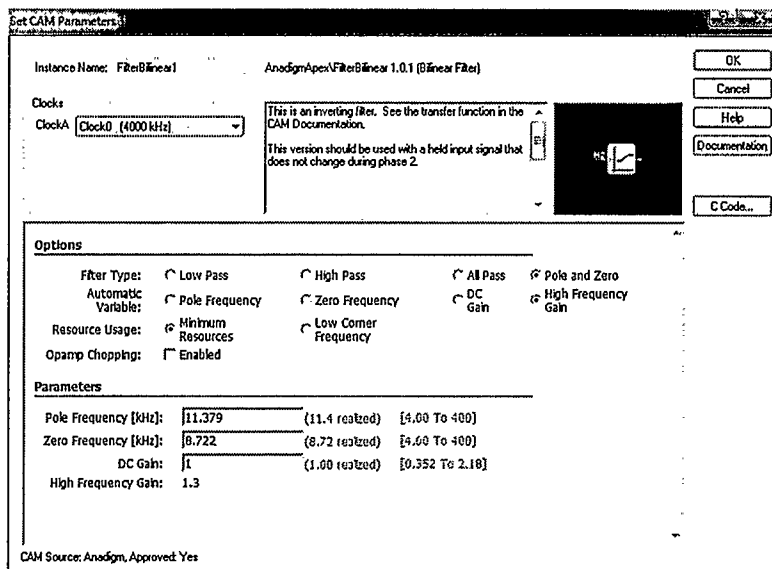
**Figure 3.13:** Approximated Type I asymmetric-slope band-pass filter in (3.2) implementation using gain, bilinear and biquadratic filter CAMs of the AnadigmDesigner tools for implementation on the AN231E04 FPAA.

### 3.2.3 FPAA Realization of Type I Band-pass Filter

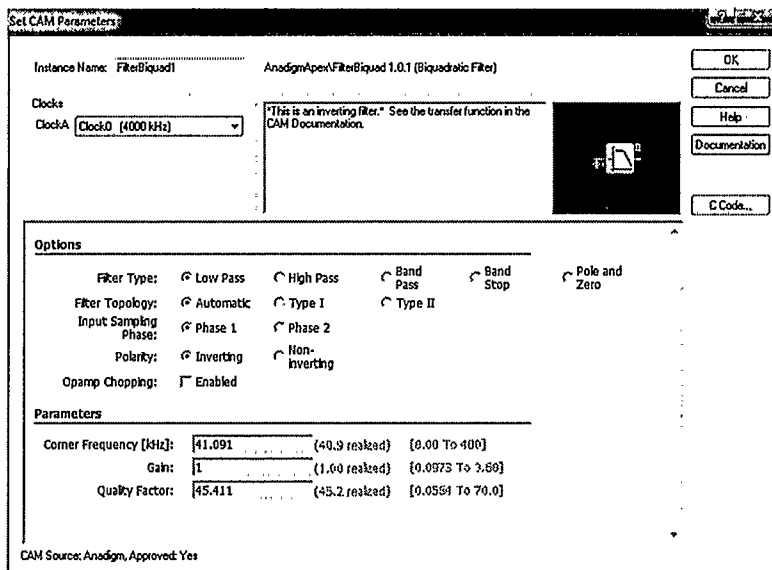
Substituting (3.1) in the Type I transfer function in (1.5) yields a fourth-order transfer function which can then be written in the form

$$H_I(s) = G_I \frac{(s + z_1)(s + z_2)}{(s + p_1)(s + p_2)} \frac{\omega_o^2}{s^2 + (\omega_o/Q)s + \omega_o^2} \quad (3.2)$$

after replacing  $s$  with  $s/\omega_o$ . This rearrangement in bilinear and biquadratic terms is needed for the FPAA realization. The fourth order transfer function in (3.2) can be tested in the FPAA using one gain CAM, two bilinear and one biquadratic filter CAMs cascaded and wired together to the desired input and output ports in the AnadigmDesigner design environment as shown in Figure 3.13. Bilinear CAMs were setup in the pole-zero configuration, shown in Figure 3.14(a) and biquadratic CAMs were setup in the low-pass configuration, shown in Figure 3.14(b). The bilinear CAM and low-pass biquadratic CAM are realized on the FPAA using the switch capacitor



(a)



(b)

Figure 3.14: Parameters setup environment of the AnadigmDesigner tools for the (a) bilinear and (b) biquadratic filter CAMs.

circuit in Figures 3.15(a) and (b). Figure 3.16 shows the experimental results realizing a filter with  $(\alpha, a, b, k) = (0.5, 0.03, 1, 1)$  which theoretically yields  $Q = 47.64$  and  $f_o = 38.42\text{kHz}$ . With reference to (3.2), the poles and zeros of the bilinear blocks in  $\text{kHz}$  are respectively  $(z_1, z_2, p_1, p_2) = (71.988, 4.011, 359.44, 19.773)$  and  $(Q, f_o)$  for

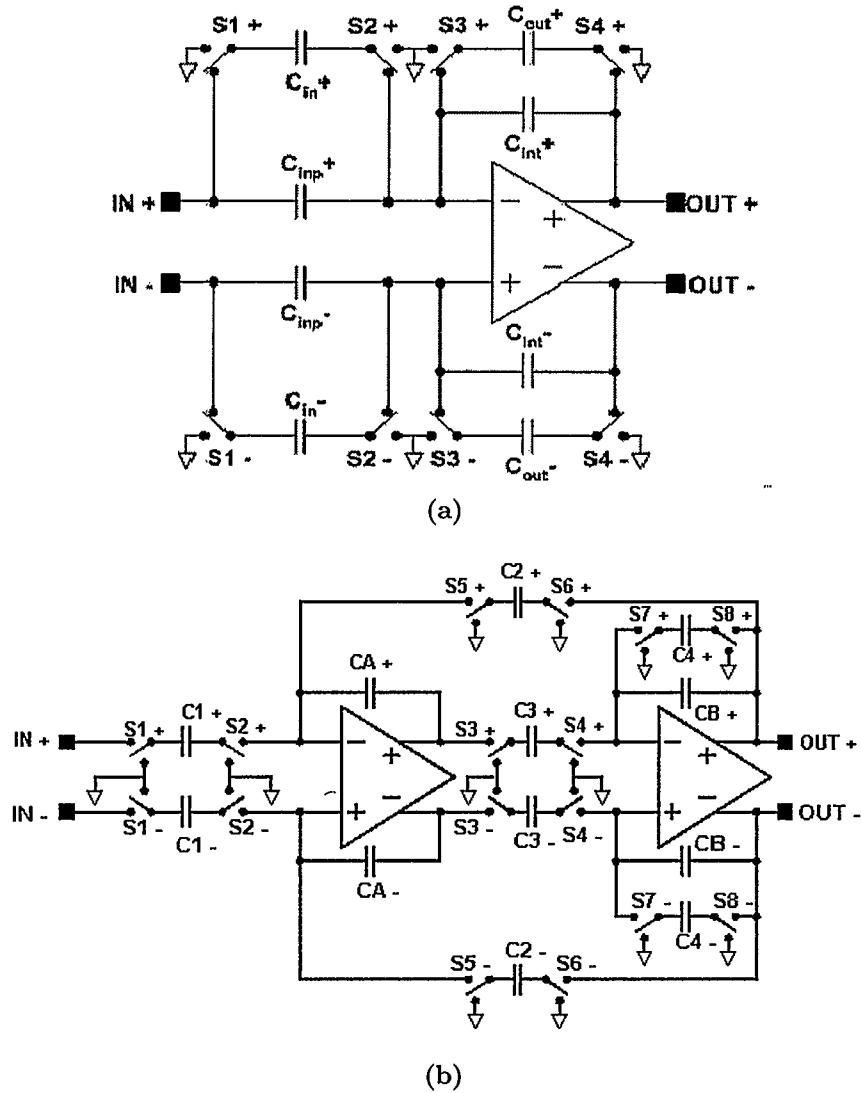


Figure 3.15: Internal switched capacitor circuits on the FPAA to realize the (a) pole/zero bilinear and (b) low-pass biquadratic transfer functions.

low-pass filter are  $(48.95, 38.414kHz)$ , respectively. The gain of the transfer function is  $G_I = 0.147$ . The measured quality factor  $Q$  was 44.13 and the center frequency  $f_o$  was  $38.73kHz$  which are very close to the design values. It is important to note here that the pole and zero values of (3.2) are rounded off by the FPAA.

Figure 3.17 shows another design example at  $(\alpha, a, b, k) = (0.1, 0.17, 1, 0.035)$  for a Type I transfer function. The poles and zeros of fourth-order transfer function in (3.2) in  $kHz$  are  $(z_1, z_2, p_1, p_2) = (122.55, 8.722, 165.049, 11.379)$  and  $G_I = 0.0404$  and

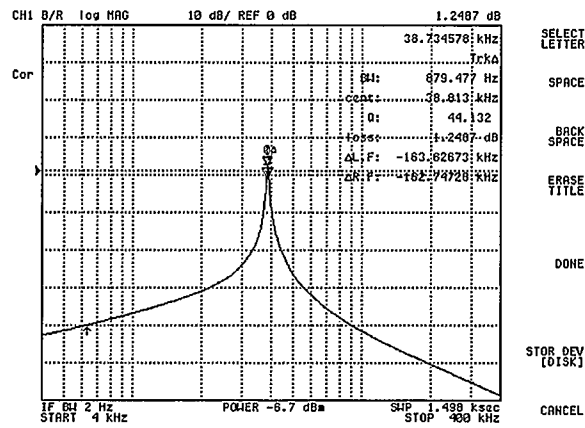


Figure 3.16: Experimental results using an FPAA for Type I asymmetric filter in 1.5 with  $\alpha = 0.5$ ,  $Q = 47.64$ .

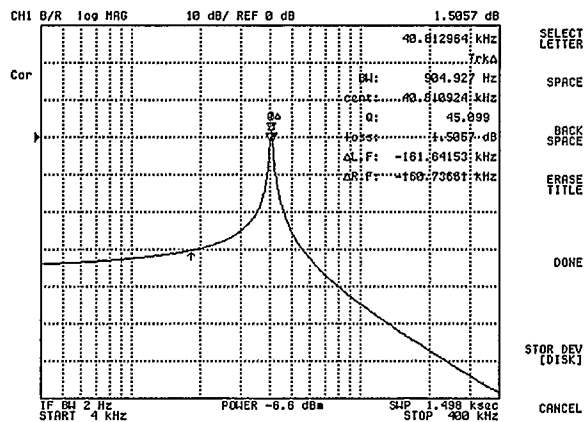


Figure 3.17: Experimental results using an FPAA for Type I asymmetric filter in 1.5 with  $\alpha = 0.1$ ,  $Q = 45.1$ .

$(Q, f_o)$  for low-pass CAM are  $(45.41, 41.091kHz)$ , respectively. The measured  $(Q, f_o)$  for a designed  $Q = 43.3$  and  $f_o = 41.078kHz$  were  $(45.1, 40.813kHz)$ , respectively.

It is to be noted that Type I transfer function in (1.6) can be obtained from the transfer function in (1.5) if  $\alpha$  is replaced by  $1 - \alpha$ . The implementation of this is that the fourth-order transfer function in (3.2) can be used for the Type I transfer function in (1.6) if for identical  $a$ ,  $b$  and  $k$ ,  $\alpha$  is replaced by  $1 - \alpha$ . To illustrate an example

the fourth order transfer function in (3.2) for the Type I filter in (1.5) with given  $a$ ,  $b$ ,  $k$  and  $\alpha = 0.1$  can be used for the Type I transfer function in (1.6) for the same  $a$ ,  $b$  and  $k$  but with  $\alpha = 0.9$ . As a result, Figure 3.17 shows the experimental result for the Type I filter in (1.6) for the same  $a$ ,  $b$  and  $k$  used in the previous example but for  $\alpha = 0.9$ .

### 3.2.4 FPAA Realization of Type II Band-pass Filter

Substituting (3.1) in a Type II transfer function in (1.7) yields a fourth-order transfer function which can then be written in the form

$$H_{II}(s) = G_{II} \frac{(s + \hat{z}_1)(s + \hat{z}_2)}{(s + \hat{p}_1)(s + \hat{p}_2)} \frac{s(\omega_o/Q)}{s^2 + (\omega_o/Q)s + \omega_o^2} \quad (3.3)$$

after replacing  $s$  with  $s/\omega_o$ . This rearrangement in bilinear and biquadratic terms is needed for the FPAA realization. The fourth order transfer function in (3.3) can be tested in the FPAA using one gain CAM, two bilinear and one biquadratic filter CAMs cascaded and wired together to the desired input and output ports in the AnadigmDesigner design environment as shown in Figure 3.18. Bilinear filters were setup in the pole-zero configuration and biquadratic filters were setup in the band-pass configuration.

Figure 3.19 shows a design example at  $(\alpha, a, b, k) = (0.5, 0.05, 1, 0.8)$  for Type II transfer function in (1.7). The poles and zeros of fourth-order transfer function in (3.3) in  $kHz$  are  $(\hat{z}_1, \hat{z}_2, \hat{p}_1, \hat{p}_2) = (72, 4.011, 365.94, 20.25)$  and  $G_{II} = 0.198$ . The band-pass block has  $Q = 36.73$  and  $f_o = 37.505kHz$ . The measured  $(Q, f_o)$  for a designed  $Q = 39$  and  $f_o = 38.3kHz$  were  $(38.935, 37.57kHz)$ , respectively.

Another design example at  $(\alpha, a, b, k) = (0.1, 0.027, 1, 1)$  with  $f_o = 37.916kHz$  and  $Q = 37.52$  for the Type II filter is shown in Figure 3.20. The poles and zeros of the bilinear blocks in  $kHz$  are respectively  $(\hat{z}_1, \hat{z}_2, \hat{p}_1, \hat{p}_2) = (8.722, 122.55, 11.805, 165.9)$  and  $G_{II} = 1.356$ . The quality factor and center frequency  $(Q, f_o)$  for band-pass filter

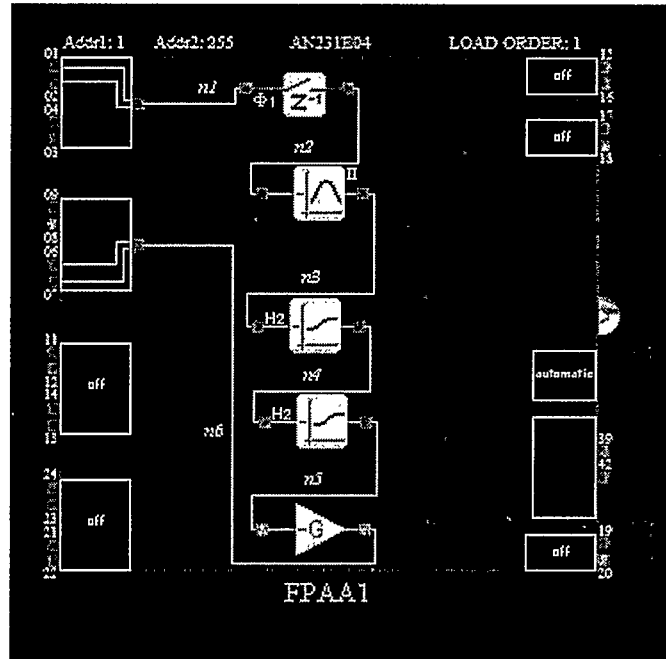


Figure 3.18: Approximated Type II asymmetric-slope band-pass filter in (3.3) implementation using gain, bilinear and biquadratic filter CAMs of the AnadigmDesigner tools for implementation on the AN231E04 FPA.

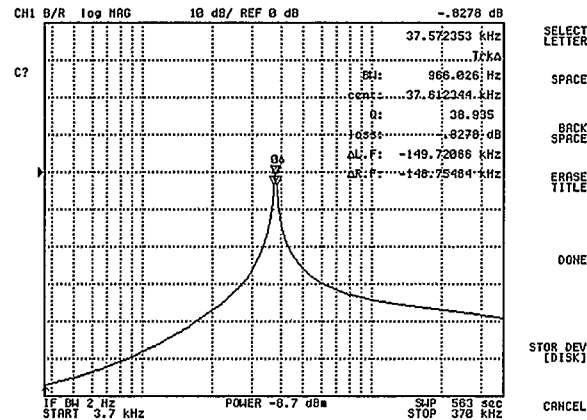
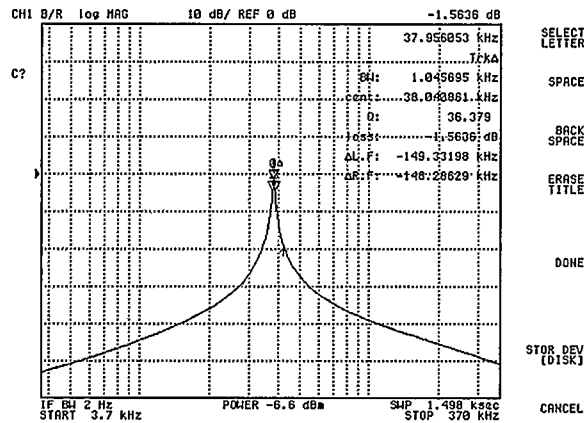


Figure 3.19: Experimental results using an FPA for Type II asymmetric filter in (1.7) with  $\alpha = 0.5$ ,  $Q = 39$ .

CAM are  $(37.47, 37.922\text{kHz})$ , respectively. The measured quality factor and center frequency are  $Q = 36.37$  and  $f_o = 37.956\text{kHz}$  which are very close to the theoretical values. Note that this Type II filter response has an almost symmetric characteristic



**Figure 3.20:** Experimental results using an FPAA for Type II asymmetric filter in (1.7) with  $\alpha = 0.1$ ,  $Q = 37.52$ .

about  $f_o$  because  $\alpha$  is small. The slope at frequencies lower than  $f_o$  is  $22 \text{ dB/dec}$  while it is  $18 \text{ dB/dec}$  at frequencies greater than  $f_o$  which is to be expected from Table 2.2.

Finally, it is worth noting once again that the Type II transfer function in (1.8) can be obtained from (1.7) if  $\alpha$  is replaced by  $1 - \alpha$ . Therefore, the approximated transfer function in (3.3) for Type II filter in (1.7) can be used for Type II filter in (1.8) if for identical  $a$ ,  $b$  and  $k$ ,  $\alpha$  is replaced by  $1 - \alpha$ . As an example, the fourth order transfer function in (3.3) with given  $a$ ,  $b$ ,  $k$  and  $\alpha = 0.1$  can be used for Type II transfer function in (1.8) for the same  $a$ ,  $b$  and  $k$  but with  $\alpha = 0.9$ . As a result, Figure 3.20 shows the experimental result for the Type II filter in (1.8) for the same  $a$ ,  $b$  and  $k$  used in the previous example but for  $\alpha = 0.9$ .

Note that the FPAA internal structure is based on switched capacitor building blocks running at a 4MHz sampling clock. Therefore, the bandwidth of any circuit implemented using the FPAA should not exceed 400kHz (1/10 of the sampling frequency) to obtain sufficient accuracy. The center frequency of the filters realized using the FPAA in this work was around 40kHz.

## CHAPTER 4

### Non-Ideal Effects

#### 4.1 Lossy Elements

##### 4.1.1 Type I FDNR-Based Circuit

To study the non-ideal effects in the proposed asymmetric-slope band-pass filters, it is useful to begin with a study of the non-idealities in the passive prototypes. In particular in the FDNR and the inductor, both of which would normally be implemented using active circuits. For this consider the modified passive prototype shown in Figure 2.4(a) where the  $D$ -element of the Type I filter is now modeled by an ideal  $D$ -element in parallel with capacitor  $c_p$  to model the losses as shown in Figure 4.1. The quality factor of non-ideal FDNR is  $Q_D = c_p/D\omega$  and straightforward analysis yields a modified Type I FDNR-based transfer function of the form,

$$H_I(s) = \frac{as^\alpha}{s^2 + as^\alpha + b + As} \quad (4.1)$$

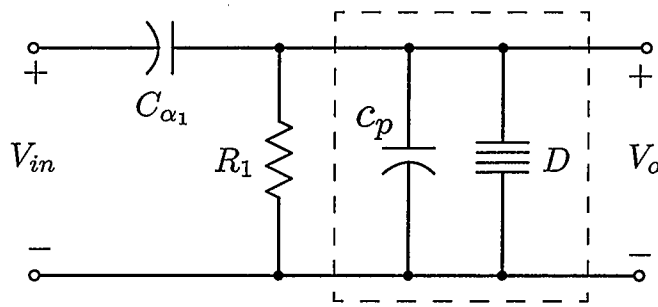


**Figure 4.1:** Non-ideal model of the Type I FDNR-based filter accounting for the lossy FDNR as shown by the dashed line.

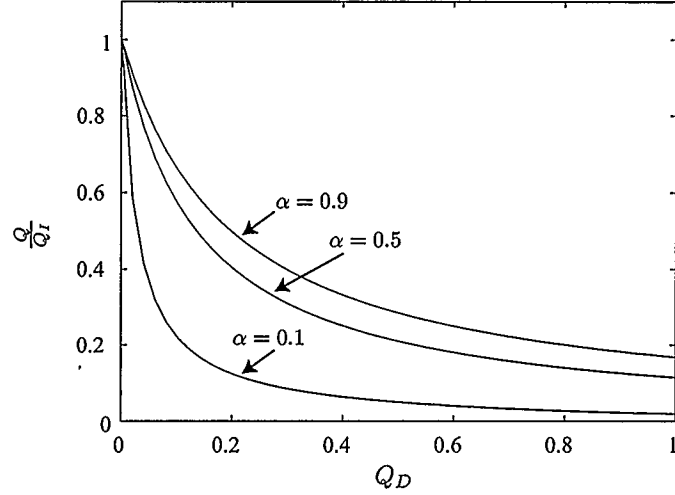


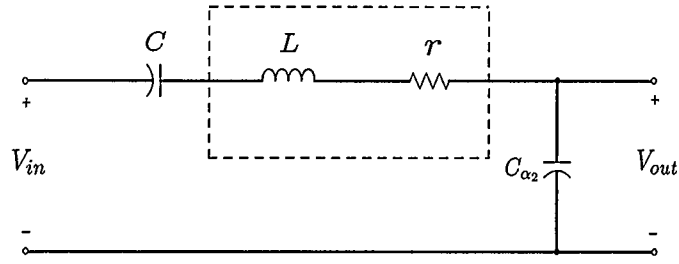
**Figure 4.2:** Plot of ratio  $\frac{Q}{Q_I}$  versus  $Q_D$  for Type I FDNR-based filter.  $Q_I$  is the ideal quality factor of the filters with ideal elements and  $Q$  is the observed quality factor of the filters with lossy elements.

where  $A = Q_D \omega \frac{\text{rad}}{\text{sec}}$  and  $\alpha_1 = \alpha$ . Ideally as  $Q_D \rightarrow 0$  equation (4.1) reverts back to Type I transfer function in (1.5) with  $k_1 = 1$ . In Figure 4.2, a plot of the ratio of the desired  $Q$  of the filter to the ideal quality factor  $Q_I$  against  $Q_D$  is shown for  $a = 0.2$ ,  $b = 1$  and various  $\alpha$ . Note that the ideal ratio of  $Q/Q_I$  should be one for  $Q_D = 0$ . The plot in Figure 4.2 reveals that in the case of the Type I FDNR-based filter for low values of  $\alpha$  it is important to keep  $Q_D$  as low as possible, since the slope is the largest for small  $\alpha$ . As  $\alpha$  increases, the slope for small  $Q_D$  decreases, meaning that more reactive losses can be tolerated.

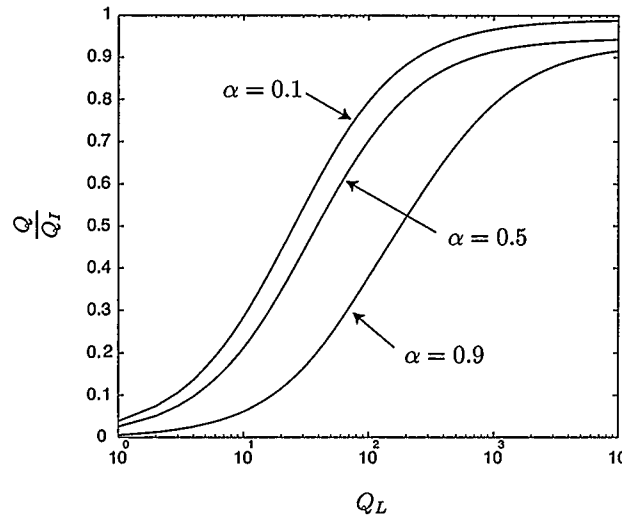
#### 4.1.2 Type I Inductor-Based Circuit

Figure 4.3 shows the modified passive prototype shown in Figure 2.4(b) where the inductor of the Type I filter is now modeled by an ideal inductor in series with resistor  $r$  to model the losses. Here, the quality factor of non-ideal inductor is  $Q_L = L\omega/r$ . The non-ideal transfer function of Type I inductor based filter in (1.6) can be written in the form

$$H_{II}(s) = \frac{as^{1-\alpha}}{s^2 + as^{1-\alpha} + b + \frac{1}{B}s}, \quad (4.2)$$



**Figure 4.3:** Non-ideal model of the Type I inductor-based filter accounting for the lossy inductor as shown by the dashed line.



**Figure 4.4:** Plot of ratio  $\frac{Q}{Q_I}$  versus  $Q_L$  for Type I inductor-based filter.  $Q_I$  is the ideal quality factor of the filters with ideal elements and  $Q$  is the observed quality factor of the filters with lossy elements.

where  $B = Q_L/\omega \frac{1}{\text{rad/sec}}$  and  $\alpha_2 = \alpha$ . Ideally as  $Q_L \rightarrow \infty$  equation (4.2) reverts back to the Type I transfer function in (1.6) with  $k_2 = 1$ . Figure 4.4 shows a plot of the ratio of the desired  $Q$  of the filter to the ideal quality factor  $Q_I$  against  $Q_L$  for  $a = 0.2$ ,  $b = 1$  and various  $\alpha$ . It reveals that large inductor quality factors are important to maintain a high  $Q/Q_I$  ratio. As  $\alpha$  decreases this requirement can be relaxed but it is clear overall that large  $Q_L$ 's are needed to ensure this circuit yields the desired  $Q$ .

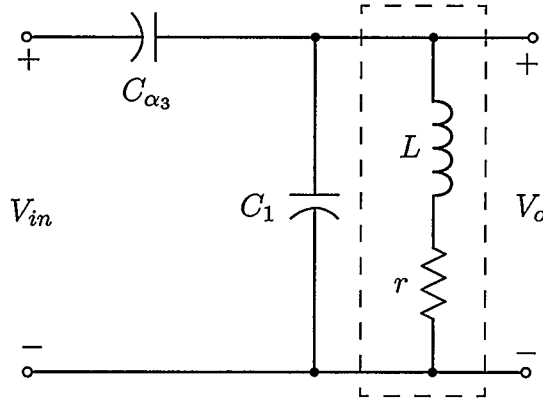


**Figure 4.5:** Non-ideal model of the Type II inductor-based filter accounting for the lossy inductor as shown by the dashed line.

#### 4.1.3 Type II Inductor-Based Circuit

The inductor of the Type II filter in Figure 2.5(a) is now modeled by an ideal inductor  $L$  in series with resistor  $r$  in Figure 4.5 to show its losses. Here, the quality factor of non-ideal inductor is  $Q_L = L\omega/r$ . The non-ideal transfer function of Type II inductor based filter can be written in the form

$$H_{III}(s) = \frac{a \left( s^{1+\alpha} + \frac{1}{B} s^\alpha \right)}{s^2 + a s^{1+\alpha} + b + \frac{1}{B} (s + a s^\alpha)}, \quad (4.3)$$

where  $B = Q_L/\omega \frac{1}{\text{rad/sec}}$  and  $\alpha_3 = \alpha$ . It is clear that as  $Q_L \rightarrow \infty$  equation (4.3) reverts back to the Type II transfer function in (1.7) with  $k_3 = 1$ . In Figure 4.6 plot of varying  $Q_L$  to the ratio of the desired  $Q$  of the filter to the ideal quality factor  $Q_I$  is shown for  $a = 0.2$ ,  $b = 1$  and various  $\alpha$ . Note that the ideal ratio of  $Q/Q_I$  should be one for  $Q_L = \infty$ . The plot of Figure 4.5 reveals that large inductor quality factors are needed to maintain a high  $Q/Q_I$  ratio. As  $\alpha$  decreases this requirement can be relaxed but it is clear that large quality factors for the inductor are needed to ensure this circuit yields the desired  $Q$ .

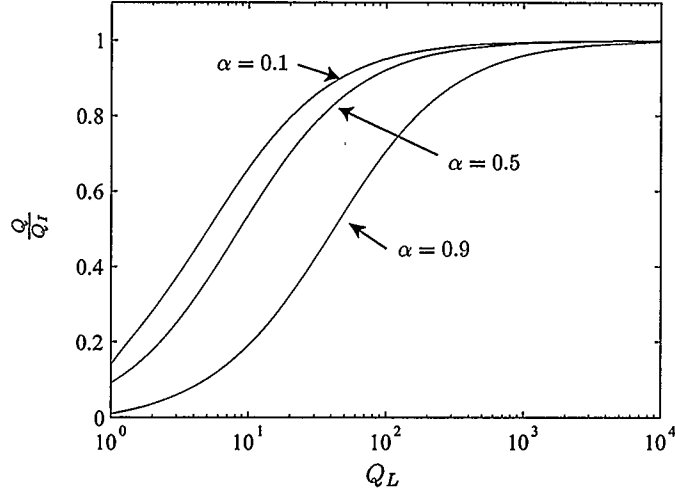


**Figure 4.6:** Plot of ratio  $\frac{Q}{Q_I}$  versus  $Q_L$  for Type II inductor-based filter.  $Q_I$  is the ideal quality factor of the filters with ideal elements and  $Q$  is the observed quality factor of the filters with lossy elements.

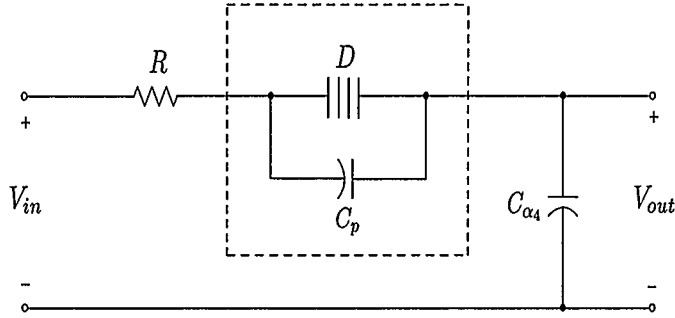


**Figure 4.7:** Non-ideal model of the Type II FDNR-based filter accounting for the lossy FDNR as shown by the dashed line.

#### 4.1.4 Type II FDNR-Based Circuit

The  $D$ -element of the Type II filter in Figure 2.5(b) is now modeled by an ideal  $D$ -element in parallel with capacitor  $c_p$  in Figure 4.7 to show the losses. The quality factor of non-ideal FDNR is  $Q_D = c_p/D\omega$ . The non-ideal transfer function for the Type II FDNR-based filter can be written in the form

$$H_{IV}(s) = \frac{a(s^{2-\alpha} + As^{1-\alpha})}{s^2 + as^{2-\alpha} + b + A(s + as^{1-\alpha})}, \quad (4.4)$$

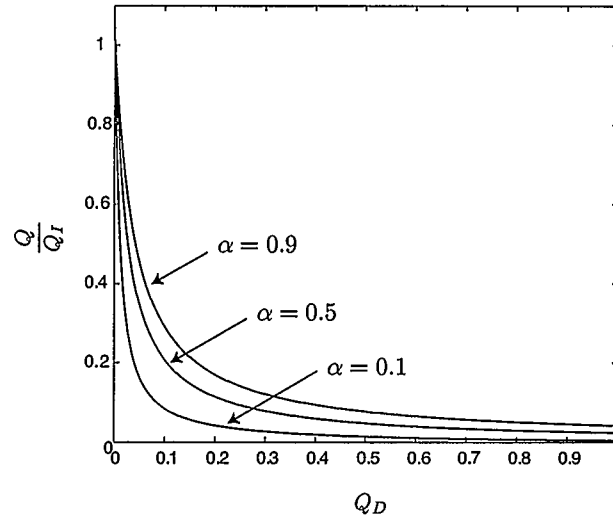


**Figure 4.8:** Plot of ratio  $\frac{Q}{Q_I}$  versus  $Q_D$  for Type II FDNR-based filter.  $Q_I$  is the ideal quality factor of the filters with ideal elements and  $Q$  is the observed quality factor of the filters with lossy elements.

where  $A = Q_D \omega \frac{\text{rad}}{\text{sec}}$  and  $\alpha_4 = \alpha$ . In Figure 4.8 a plot of varying  $Q_D$  to the ratio of the desired  $Q$  of the filter to the ideal quality factor  $Q_I$  is shown for  $a = 0.2$ ,  $b = 1$  and various  $\alpha$ . Ideally as  $Q_D \rightarrow 0$  equation (4.4) reverts back to the Type II transfer function in (1.8) with  $k_4 = 1$ . Note that the ideal ratio of  $Q/Q_I$  should be one for  $Q_D = 0$ . The plot of Figure 4.8 reveals that in the case of the Type II FDNR-based filter for low values of  $\alpha$ , it is important that  $Q_D$  be kept as low as possible, since the slope is the largest for small  $\alpha$ . As  $\alpha$  increases the slope for small  $Q_D$  decreases meaning that more reactive losses can be tolerated.

Finally it is worth noting that equations (4.3) and (4.4) reveal that the deviation in the  $Q$  and  $f_o$  is larger for the Type II circuits because of the fact that the responses of these filters are more susceptible to variations in the quality factor of the grounded inductor and floating FDNR, respectively.

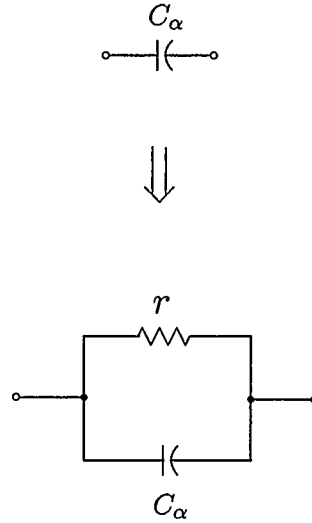


**Figure 4.9:** The non-ideal fractional capacitor is modeled by an ideal fractional capacitor  $C_\alpha$  in parallel with resistor  $r$ .

#### 4.1.5 The Non-ideal Fractional Capacitor

In this section, we study the effect of non-idealities in the fractional capacitor on filter quality factor. For this, consider the modified fractional capacitor shown in Figure 4.9 where the non-ideal fractional capacitor is now modeled by an ideal fractional capacitor  $C_\alpha$  in parallel with a resistor  $r$  to model the losses.

The quality factor of ideal fractional capacitor is

$$Q_I = -\tan\left(\frac{\alpha\pi}{2}\right) \quad (4.5)$$

and the quality factor of non-ideal fractional capacitor shown in Figure 4.9 is

$$Q = -\frac{rC_\alpha\omega^\alpha \sin\left(\frac{\alpha\pi}{2}\right)}{1 + rC_\alpha\omega^\alpha \cos\left(\frac{\alpha\pi}{2}\right)} \quad (4.6)$$

The non-ideal quality factor of fractional capacitor approaches the ideal quality factor for  $r \rightarrow \infty$ . In Figure 4.10, the plot of the ratio of the actual  $Q$  of the fractional capacitor to the ideal quality factor  $Q_I$  against  $r$  is shown for  $C_\alpha = 1F$  and various

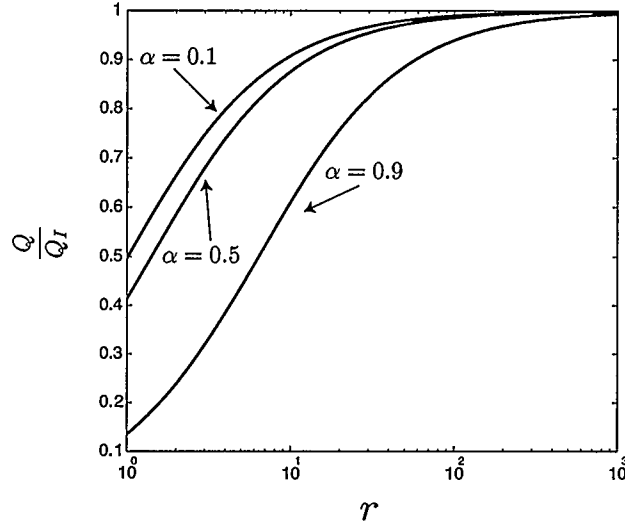


**Figure 4.10:** Plot of the ratio of the actual  $Q$  of the fractional capacitor to the ideal quality factor  $Q_I$  versus  $r$  for  $C_\alpha = 1F$  and various values of  $\alpha$ .

values of  $\alpha$ .

## 4.2 Finite Gain Bandwidth Product

For the opamp-based designs of filters in Figures 2.18, 2.20 and 2.22 it is important to find the effect of the finite gain-bandwidth product on  $\omega_o$  and  $Q$ . Here, we assume that identical opamps, each described by a single-pole open-loop transfer function of the form  $A(s) = \omega_t/s$  ( $\omega_t$  is the amplifier's gain-bandwidth product) are used.

### 4.2.1 Type I FDNR-Based Circuit

Using non-ideal and identical opamps the following transfer function is derived for the Type I FDNR-based filter

$$H_I(s) = \frac{1 + \frac{\tau s^2 + s}{\omega_t}}{\frac{1}{\omega_t^2} [\tau s^3 + (1 + \tau)s^2 + \omega_t s + \frac{1}{a} P_\alpha(s)] + \frac{1}{2}} \quad (4.7)$$

where  $\tau = RC$  and  $P_\alpha(s) = s^{4-\alpha} + (\frac{1}{\tau} + \omega_t + b\tau)s^{3-\alpha} + (\frac{1}{\tau} + b\tau\omega_t + 0.5\omega_t^2 + 2b)s^{2-\alpha} + b\omega_t s^{1-\alpha} + \frac{1}{2\tau}b\omega_t^2 s^{-\alpha}$  with  $a = C_\alpha/RC^2$  and  $b = 1/R_1RC^2$  as defined earlier. It is noted

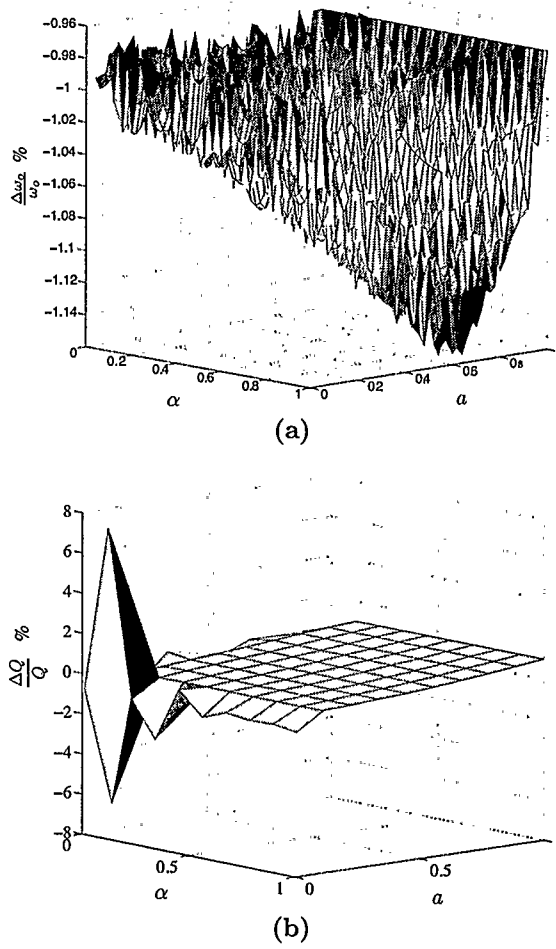


**Figure 4.11:** 3D plots of (a)  $\Delta\omega_o/\omega_o$  for  $\alpha=[0.005, 1]$ ,  $a=[0.005, 1]$  and (b)  $\Delta Q/Q$  for  $\alpha=[0.005, 1]$ ,  $a=[0.005, 1]$  both for the FDNR-based Type I realization.

that (4.7) has complex zeros located at  $\omega_z \approx \sqrt{\omega_t/\tau}$  for  $\omega_t > 1/4\tau$ . To minimize the effect of  $\tau$ , a good choice is to select  $\tau = 100/\omega_t$  which then yields  $\omega_z \approx \omega_t/10$ .

Furthermore, for the Type I FDNR-based filter, Figures 4.11(a) and 4.11(b) show the percentage variability of  $\Delta\omega_o/\omega_o$  and  $\Delta Q/Q$  versus  $\alpha$  and  $a$  for  $b = 1$  and  $\omega_t = 1000\omega_o$ . The minimum and maximum deviations for  $\omega_o$  and  $Q$  were respectively found to be  $(-0.97\%, -1.15\%)$  and  $(-6.6\%, 7.47\%)$ . For  $\omega_t = 100\omega_o$ , the minimum and maximum deviations jump to  $(-2.11\%, -1.51\%)$  and  $(-55.46\%, 4.49\%)$ . As expected the deviation in  $Q$ , which is traditionally larger than  $\omega_o$ , gets progressively worse as the center frequency approaches the opamp bandwidth. The Matlab codes to generate

Figures 4.11(a) and 4.11(b) is provided in the Appendix C.

#### 4.2.2 Type I MAB-Based Circuit

Examining the MAB based circuit of Figure 2.18(b), under the same assumptions, reveals that there are no complex zeroes in the non-ideal transfer function as shown in Appendix D. The transfer function is of order  $s^6$  in the integer terms and  $s^{6+\alpha}$  in the fractal terms of  $P_\alpha(s)$ .

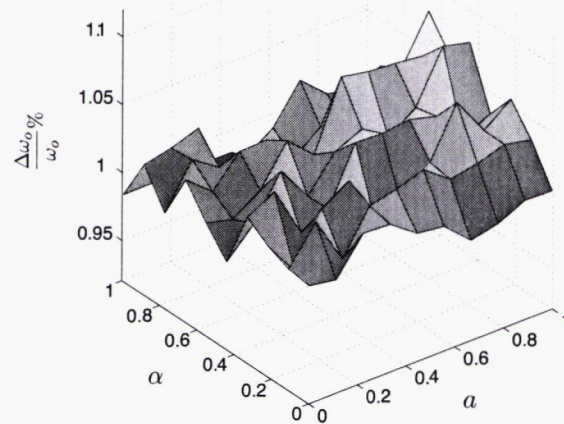
For the Type I MAB-based filter, Figures 4.12(a) and 4.12(b) show the percentage variability of  $\Delta\omega_o/\omega_o$  and  $\Delta Q/Q$  versus  $\alpha$  and  $a$  for  $b = 1$ ,  $\tau_1 = \tau_2 = \tau = 100/\omega_t$  and  $\omega_t = 1000\omega_o$ . Here  $\tau_1 = R_1C_1$ ,  $\tau_2 = R_2C_2$  and  $\tau = R_\alpha C_\alpha$ . The minimum and maximum deviations for  $\omega_o$  and  $Q$  were respectively found to be (0.925%,1.0811%) and (-0.698%,-57.81%). For  $\omega_t = 100\omega_o$ , the minimum and maximum deviations jump to (0.124%,1.006%) and (1.515%, -93.35%), respectively.

#### 4.2.3 Type I Inductor-based Circuit

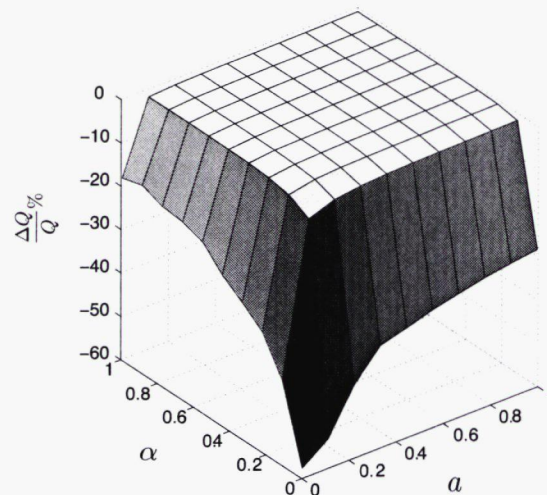
The non-ideal transfer function for the Type I inductor-based asymmetric-slope band-pass of Figure 2.20 is of order  $s^5$  in the integer terms and  $s^{5+\alpha}$  in the fractal terms of  $P_\alpha(s)$  as shown in Appendix E.

Figure 4.13(a) and 4.13(b) show the percentage deviation of  $\Delta Q/Q$  and  $\Delta\omega_o/\omega_o$  versus  $\alpha$  and  $a$  for  $\tau_3 = b = 1$ ,  $\tau_1 = 100/\omega_t$ ,  $\omega_t = 1000\omega_o$ . Here  $\tau_1 = R_2C_1$  and  $\tau_3 = R_3/R_2$ . The maximum deviations for  $\omega_o$  is (-0.235%,-0.5179%) while it is (-9.9%,72.73%) for the quality factor. For  $\omega_t = 100\omega_o$ , the minimum and maximum deviations of center frequency and quality factor jump to (-1.13%,2.307%) and (-8.81%, -88.45%), respectively.

In Figure 4.14, a comparison of the ideal magnitude response in (1.5) to the magnitude response of the circuits in Figures 2.18(a), 2.18(b) and 2.20 is shown for  $\alpha = 0.5$ ,  $a = 0.2$ ,  $\tau_3 = 1$ ,  $\tau_1 = \tau_2 = \tau = 100/\omega_t$ ,  $\omega_t = 1000\omega_o$  and  $b = 1$  with all the



(a)

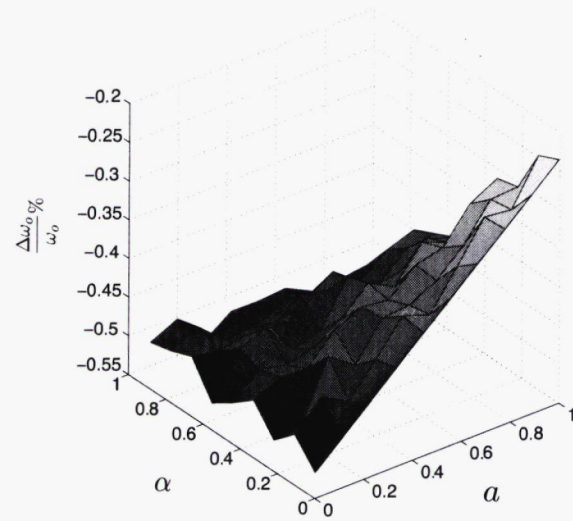


(b)

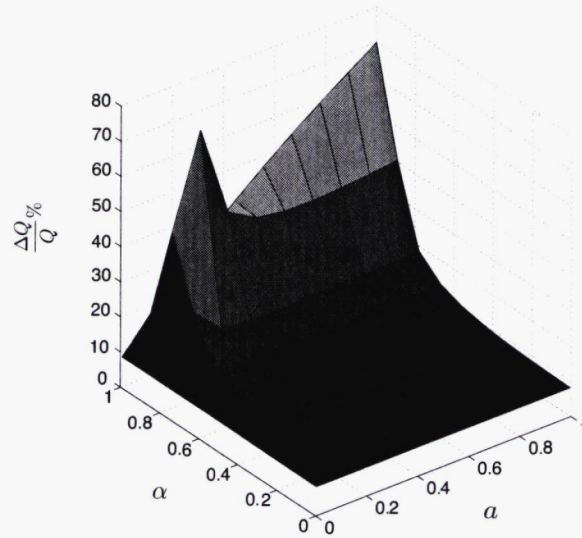
**Figure 4.12:** 3D plots of (a)  $\Delta\omega_o/\omega_o$  for  $\alpha=[0.005, 1]$ ,  $a=[0.005, 1]$  and (b)  $\Delta Q/Q$  for  $\alpha=[0.005, 1]$ ,  $a=[0.005, 1]$  both for the MAB-based Type I realization.

plots normalized to a center frequency gain of  $0\text{dB}$ . The presence of the zeroes in the FDNR based circuit can clearly be seen. Note that Type I ideal transfer functions in (1.5) and (1.6) have the same amplitude response for given  $a$  and  $b$  when  $\alpha = 0.5$ .

In order however, to gain a greater appreciation for the differences in the perfor-



(a)



(b)

**Figure 4.13:** 3D plots of (a)  $\Delta\omega_o/\omega_o$  for  $\alpha = [0.005, 1]$ ,  $a = [0.005, 1]$  and (b)  $\Delta Q/Q$  for  $\alpha = [0.005, 1]$ ,  $a = [0.005, 1]$  both for the inductor-based Type I realization.

manances of the Type I, FDNR, inductor based and MAB based realizations a complied table of simulated results for percentage deviations in  $\Delta\omega_o/\omega_o$  and  $\Delta Q/Q$  to various values of  $a$  is shown in Table 4.1 for  $\alpha = 0.5$ ,  $\tau_1 = \tau_2 = \tau = 100/\omega_t$ ,  $\tau_3 = 1$ ,

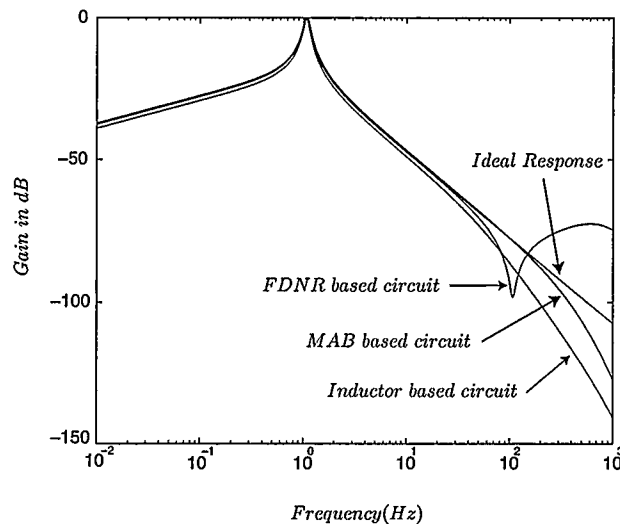


**Figure 4.14:** Plot of the amplitude response of the ideal transfer function of 1.5 compared to the non-ideal transfer functions of Figures 2.18(a) and (b) and 2.20 for  $\tau_1 = \tau_2 = \tau = 100/\omega_t$ ,  $\tau_3 = 1$ ,  $\omega_t = 1000\omega_o$  and  $b = 1$ .

$\omega_t = 1000\omega_o$  and  $b = 1$ . The percentage variation in  $\Delta\omega_o/\omega_o$  is small and roughly the same across the FDNR, inductor based and MAB based circuits of Figures 2.18(a), 2.18(b) and 2.20. Conversely if the percentage variation in  $\Delta Q/Q$  of Table 4.1(b) is examined the FDNR-based circuit always outperforms the MAB-based and inductor-based circuits for all  $a$  and inductor-based circuit has the worst performance. Note that for  $\alpha = 0.5$  the  $\omega_o$ 's and  $Q$ 's of the Type I filters in Figures 2.18(a), 2.18(b) and 2.20 are identical for a given  $a$  and  $b$ .

#### 4.2.4 Type II Inductor-Based Circuit

The non-ideal transfer function for the Type II inductor-based asymmetric-slope band-pass filter in Figure 2.22(a) is given as

$$H_{II}(s) = \frac{\omega_t s(s + b\tau + \omega_t)}{s^3 + (\omega_t + b\tau)s^2 + (b\tau\omega_t + \frac{1}{2}\omega_t^2)s + \frac{1}{a}P_\alpha(s)} \quad (4.8)$$

where  $\tau = R_1 C_1$  and

$$P_\alpha(s) = s^{4-\alpha} + \left(\frac{1}{\tau} + b\tau + \omega_t\right)s^{3-\alpha} + \left(b\tau\omega_t + b + \frac{1}{2}\omega_t^2 + \frac{\omega_t}{\tau}\right)s^{2-\alpha} + b\omega_t s^{1-\alpha} + \frac{1}{2}b\omega_t^2 s^{-\alpha}$$

$\frac{\Delta\omega_o}{\omega_o}\%$			
$a$	FDNR-based	MAB-based	Inductor-based
0.01	-0.9956	1.0083	-0.4984
0.05	-1.0059	1.0119	-0.4967
0.1	-1.0111	1.0214	-0.4896
0.5	-1.0684	1.0445	-0.4369

(a)

$\frac{\Delta Q}{Q}\%$			
$a$	FDNR-based	MAB-based	Inductor-based
0.01	0.2386	-13.1336	142.58
0.05	0.4544	-3.4386	17.17
0.1	0.4749	-2.0633	8.267
0.5	0.4314	-0.8922	2.078

(b)

**Table 4.1:** Percentage variation in (a) center frequency  $\omega_o$  and (b)  $Q$  for all Type I active filter realizations with  $\alpha = 0.5$  and  $b = 1$ .

with  $a = C_\alpha/C_1$  and  $b = 1/R_1R_2CC_1$  as defined earlier. Examination of (4.8) reveals the presence of zeroes at the origin and at frequencies slightly larger than the unity gain bandwidth of the opamp.

For the Type II inductor-based filter, Figures 4.15(a) and 4.15(b) show the percentage variability of  $\Delta\omega_o/\omega_o$  and  $\Delta Q/Q$  versus  $\alpha$  and  $a$  for  $b = 1$ ,  $\tau = 100/\omega_t$  and  $\omega_t = 1000\omega_o$ . The minimum and maximum deviations for  $\omega_o$  and  $Q$  were respectively found to be  $(-0.5072\%, -1.0281\%)$  and  $(-9.92\%, 58.171\%)$ . For  $\omega_t = 100\omega_o$ , the minimum and maximum deviations jump to  $(-1.9093\%, -2.6389\%)$  and  $(-9.9958\%, 103.214\%)$ . The deviation in  $Q$  is larger than center frequency and gets progressively worse as the center frequency approaches the opamp bandwidth.

#### 4.2.5 Type II MAB-Based Circuit

If the Type II MAB-based circuit is examined, its transfer function also has a zero near the unity gain bandwidth of the opamp and likewise it also is of order  $s^6$  in the

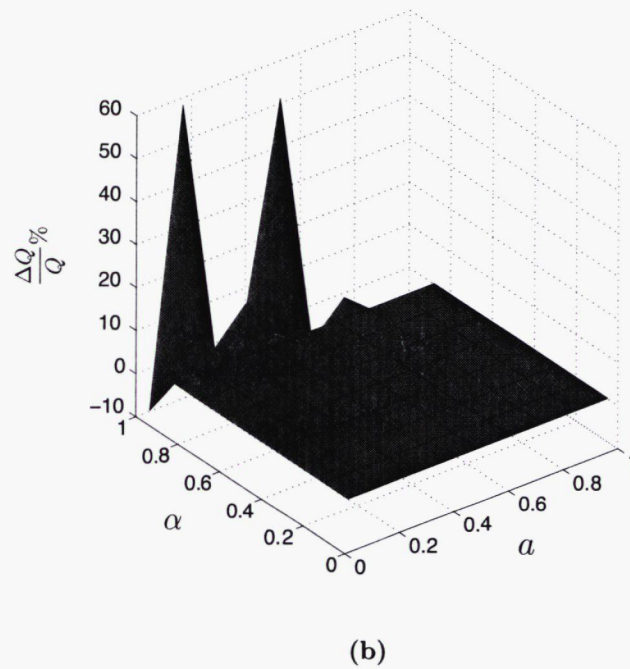
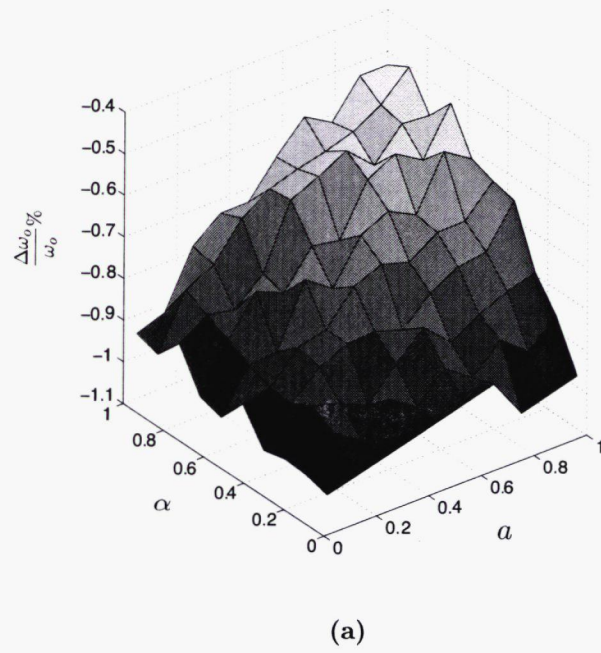


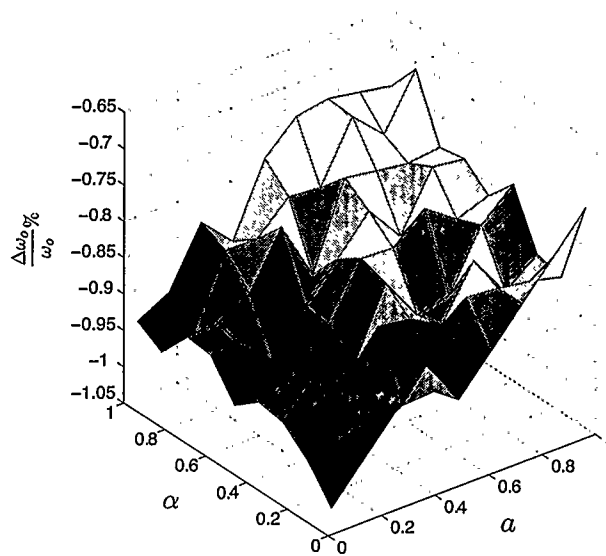
**Figure 4.15:** 3D plots of (a)  $\Delta\omega_o/\omega_o$  for  $\alpha=[0.005, 1]$ ,  $a=[0.005, 1]$  and (b)  $\Delta Q/Q$  for  $\alpha=[0.005, 1]$ ,  $a=[0.005, 1]$  both for the inductor-based Type II realization.

integer terms and  $s^{6+\alpha}$  in the fractal terms of  $P_\alpha(s)$  due to the number of opamps in the circuit as in the Type I MAB-based circuit. The non-ideal transfer function of Type II MAB-based is shown in Appendix F.

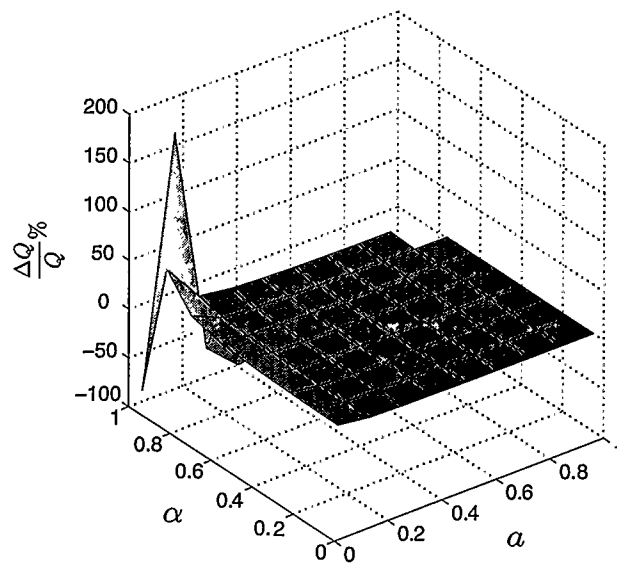
For the Type II MAB-based filter in Figure 2.22(b), Figures 4.16(a) and 4.16(b) show the percentage variability of  $\Delta\omega_o/\omega_o$  and  $\Delta Q/Q$  versus  $\alpha$  and  $a$  for  $b = 1$ ,  $\tau_1 = \tau_2 = \tau = 100/\omega_t$  and  $\omega_t = 1000\omega_o$ . Here  $\tau_1 = R_1C_1$ ,  $\tau_2 = R_2C_2$  and  $\tau = R_\alpha C_\alpha$ . The minimum and maximum deviations for  $\omega_o$  and  $Q$  were respectively found to be  $(-0.7091\%, -1.0281\%)$  and  $(-72.243\%, 168.682\%)$ . For  $\omega_t = 100\omega_o$ , the minimum and maximum deviations jump to  $(-0.7212\%, -1.716\%)$  and  $(-86.752\%, 276.315\%)$ , respectively.

In order, however, to gain a greater appreciation for the differences in the performances of the Type II inductor based and MAB based realizations a compiled table of simulated results for percentage deviations in  $\Delta\omega_o/\omega_o$  and  $\Delta Q/Q$  to various values of  $a$  is shown in Table 4.2 for  $\alpha = 0.5$ ,  $\tau_1 = \tau_2 = \tau = 100/\omega_t$ ,  $\omega_t = 1000\omega_o$  and  $b = 1$ . As expected the percentage variation in  $\Delta\omega_o/\omega_o$  is small and roughly the same across the Inductor based and MAB based circuits of Figures 2.22(a) and 2.22(b). Also Table 4.2 reveals that Type II inductor-based circuit performs better than MAB-based circuit if deviation in quality factor is considered.

The high frequency response of these two circuits can therefore be expected to be similar to Type I filters. Figure 4.17 shows a comparison of the ideal magnitude response in 1.7 to the magnitude response of the circuits in Figures 2.22(a) and 2.22(b) for  $\alpha = 0.5$ ,  $a = 0.2$ ,  $b = 1$ ,  $\tau_1 = \tau_2 = \tau = 100/\omega_t$  and  $\omega_t = 1000\omega_o$  with all the plots normalized to a center frequency gain of 0dB.



(a)



(b)

**Figure 4.16:** 3D plots of (a)  $\Delta\omega_o/\omega_o$  for  $\alpha=[0.005, 1]$ ,  $a=[0.005, 1]$  and (b)  $\Delta Q/Q$  for  $\alpha=[0.005, 1]$ ,  $a=[0.005, 1]$  both for the Type II MAB-based realization.

$\frac{\Delta\omega_o}{\omega_o}\%$		
$a$	Inductor-based	MAB-based
0.01	-0.9918	-0.9861
0.05	-0.9728	-0.9785
0.1	-0.9471	-0.9641
0.5	-0.7818	-0.8888

(a)

$\frac{\Delta Q}{Q}\%$		
$a$	Inductor-based	MAB-based
0.01	1.1975	73.6562
0.05	1.4056	9.7833
0.1	1.4123	4.948
0.5	1.2988	1.3006

(b)

**Table 4.2:** Percentage variation in (a) center frequency  $\omega_o$  and (b)  $Q$  for Type II inductor-based and MAB-based realizations with  $\alpha = 0.5$ ,  $b = 1$ .

### 4.3 Voltage and Current Tracking Errors

#### 4.3.1 Type II FDNR-Based Circuit

The Type II FDNR-based circuit was designed using current conveyors as shown in Figure 2.24. Note that for practical purposes each  $CCII-$  was replaced by two  $CCII+s$ . For the current conveyor-based design it is important to find the effect of current and voltage tracking errors ( $\varepsilon_I$  and  $\varepsilon_V$ ) on  $\omega_o$  and  $Q$ . We assume for simplicity that identical current conveyors each described by  $I_z = (1 - \varepsilon_I)I_x$  and  $V_y = (1 - \varepsilon_v)V_x$  (see Figure 2.23) are used. For the Type II FDNR-based filter, the following transfer function is then derived

$$H_{IV}(s) = k \frac{\frac{1}{RC_\alpha} s^{2-\alpha} + A(s) + \varepsilon_I^2 B(s) + \varepsilon_I C(s)}{s^2 + \frac{1}{RC_\alpha} s^{2-\alpha} + \frac{R_3}{RR_1 R_2 C_1 C_2} + A(s) + \varepsilon_I^2 [B(s) + cs^2] + \varepsilon_I [C(s) - 2cs^2]} \quad (4.9)$$

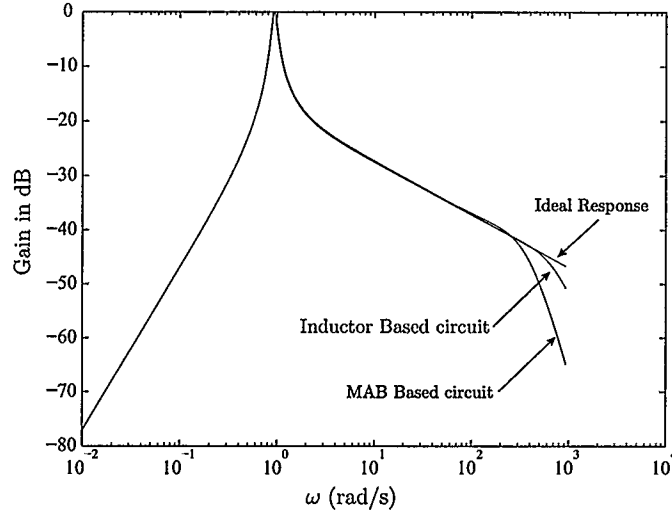


**Figure 4.17:** Normalized plot of the amplitude response of the ideal transfer function of 1.7 compared to the non-ideal transfer functions of Figures 2.22(a) and 2.22(b) for  $\alpha = 0.5$ ,  $a = 0.2$ ,  $\tau_1 = \tau_2 = \tau = 100/\omega_t$ ,  $\omega_t = 1000\omega_o$  and  $b = 1$ .

where the parameters are  $k = \frac{1}{(1-\varepsilon_V)^4}$ ,  $A(s) = [\varepsilon_I^4 - 4\varepsilon_I^3] \left( \frac{R_2 + R_3}{RR_1R_2C_\alpha C_1} s^{1-\alpha} + \frac{R_2 + R_3}{RR_2C_\alpha} s^{2-\alpha} \right)$ ,  $B(s) = \frac{6R_2 + 5R_3}{RR_1R_2C_\alpha C_1} s^{1-\alpha} + \frac{6R_2 + 5R_3}{RR_2C_\alpha} s^{2-\alpha}$ ,  $C(s) = -\left( \frac{4R_2 + 2R_3}{RR_1R_2C_\alpha C_1} s^{1-\alpha} + \frac{4R_2 + 2R_3}{RR_2C_\alpha} s^{2-\alpha} \right)$  and  $c = \left( 1 + \frac{R_3}{R_2} \right)$ . It is clear that for  $\varepsilon_I \rightarrow 0$  and  $\varepsilon_V \rightarrow 0$ , the non-ideal transfer function in (4.9) reverts to the ideal transfer function in (1.8) with  $a = 1/RC_\alpha$  and  $b = \frac{R_3}{RR_1R_2C_1C_2}$ .

The comparison between the ideal magnitude response of Type II filter in (1.8) to the magnitude response of the circuit in Figure 2.24 for  $\tau = RC_\alpha = 5$ ,  $\tau_1 = R_1C_1 = 1$ ,  $\tau_2 = R_2C_2 = 1$ ,  $\frac{R_3}{R_2} = 1$ ,  $\varepsilon_I = \varepsilon_V = 0.001$ ,  $a = 0.2$ ,  $b = 1$  and  $\alpha = 0.5$  is shown in Figure 4.18. The minimum and maximum deviations for  $\omega_o$  and  $Q$  were respectively found to be (1.196%, 1.981%) and (15.642%, 49.55%). For  $\varepsilon_I = \varepsilon_V = 0.001$ , the minimum and maximum deviations jump to (0.6429%, 2.5538%) and (4.542%, 27.132%), respectively.

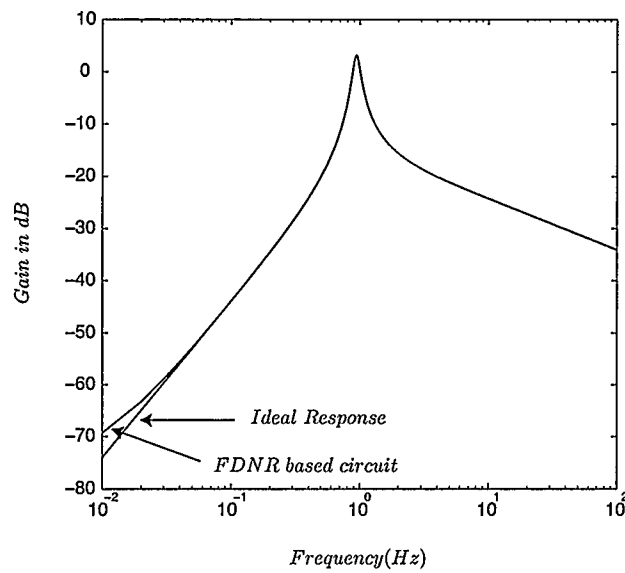


**Figure 4.18:** Plot of the amplitude response of the ideal transfer function of (1.8) compared to the non-ideal transfer function of Figure 2.24 when current and voltage tracking errors of  $CCII+$ 's are considered. For all curves  $\varepsilon_I = \varepsilon_V = 0.001$ ,  $\alpha = 0.5$ ,  $a = 0.2$  and  $b = 1$ .

## CHAPTER 5

### Higher-Order Asymmetric-Slope Band-Pass Filters

#### 5.1 Higher-Order Normal Band-pass Filters

Higher order band-pass filters are obtained using the same method proposed for the second-order asymmetric-slope band-pass filter implementation in Chapter 2. The  $m^{\text{th}}$  order low-pass filters in Figures 5.1(a) and 5.1(b) can be transformed into normal integer-order band-pass filters using  $s \rightarrow \frac{s^2 + \omega_o^2}{Bs}$  transformation, where  $\omega_o$  is the center frequency and  $B$  is the bandwidth of the band-pass filter. Now consider the band-pass filters in Figures 5.2(a) and 5.2(b), obtained by applying this transformation on the corresponding low-pass filters, respectively. In other words, a low-pass filter can be transformed into band-pass filter circuit by replacing the capacitor  $C$  with a parallel combination of capacitor and inductor of respective values  $\frac{C}{B}$  and  $\frac{B}{C\omega_o^2}$  and replacing

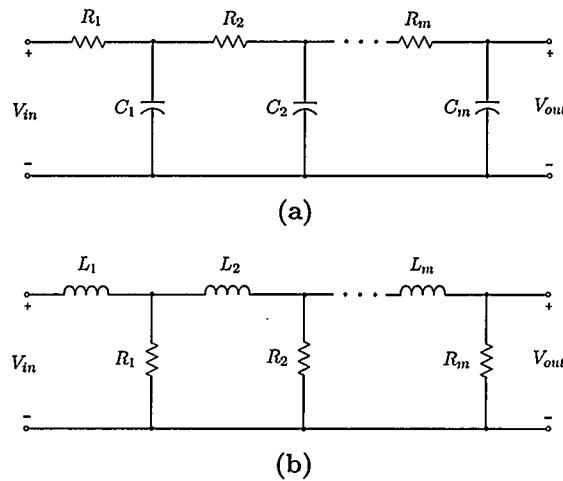
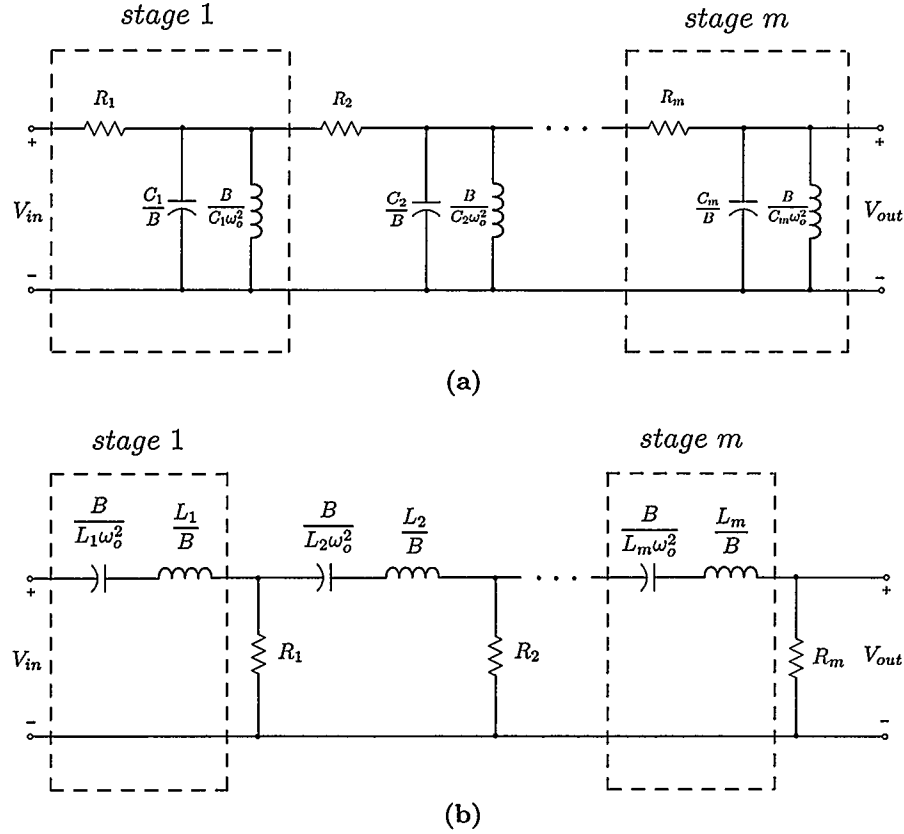


Figure 5.1:  $m^{\text{th}}$  order RC and RL low-pass filters.



**Figure 5.2:**  $m^{\text{th}}$  order band-pass filters schematics obtained by the  $s \rightarrow \frac{s^2 + \omega_o^2}{Bs}$  transformation on low-pass filters in Figure 5.1.

the inductor  $L$  with a series combination of capacitor and inductor of values  $\frac{B}{L\omega_o^2}$  and  $\frac{L}{B}$ , respectively. Likewise, Figure 5.3(a) and 5.3(b) show normal band-pass filters which are equivalent to the circuits in Figures 5.2(a) and 5.2(b) if one considers the multiplication of each element of the circuits in Figure 5.2(a) and 5.2(b) by a scaling factor  $1/\lambda s$  where  $\lambda$  is a constant of dimension  $\text{sec}^{-1}$ . In other words, Bruton  $RLC : CRD$  transformation [24] is used to generate band-pass filters in Figures 5.3(a) and 5.3(b). The transfer function of the band-pass filters in Figures 5.2 and 5.3 is given by

$$H(s) = \frac{aB^m s^m}{s^{2m} + \dots + aB^m s^m + \dots + \omega_o^{2m}} \quad (5.1)$$

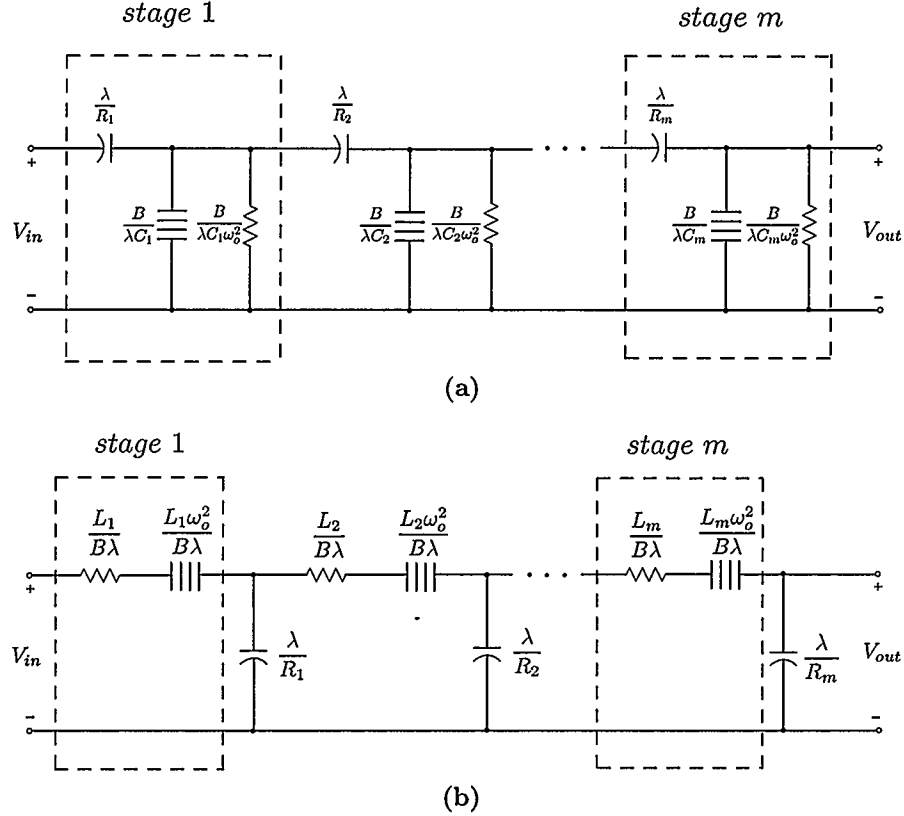


**Figure 5.3:**  $m^{\text{th}}$  order band-pass filters schematics, where  $m$  is an integer.

where  $B$  is the bandwidth,  $\omega_o$  is the center frequency and  $m$  is the order of filters.

The filters in 5.2(a) and 5.3(a) realize the transfer function in (5.1) with  $a = \prod_{i=1}^m \frac{1}{R_i C_i}$

and in the case of band-pass filters in 5.2(b) and 5.3(b),  $a = \prod_{i=1}^m \frac{R_i}{L_i}$ .

## 5.2 Asymmetric-Slope Band-pass Passive Prototypes

Consider the circuits in Figures 5.2 and 5.3. Fractional-order asymmetric-slope band-pass filters are obtained if at least one resistor in Figure 5.2 and one capacitor in Figure 5.3 is replaced by a fractional order capacitor. It is to be noted that the number of fractional-order capacitors which can be used in the  $m^{\text{th}}$  order fractional-order band-pass filter, varies from 1 to  $m$ . In other words, at least one fractional capacitor in one stage of a band-pass filter is needed to have an asymmetric-slope

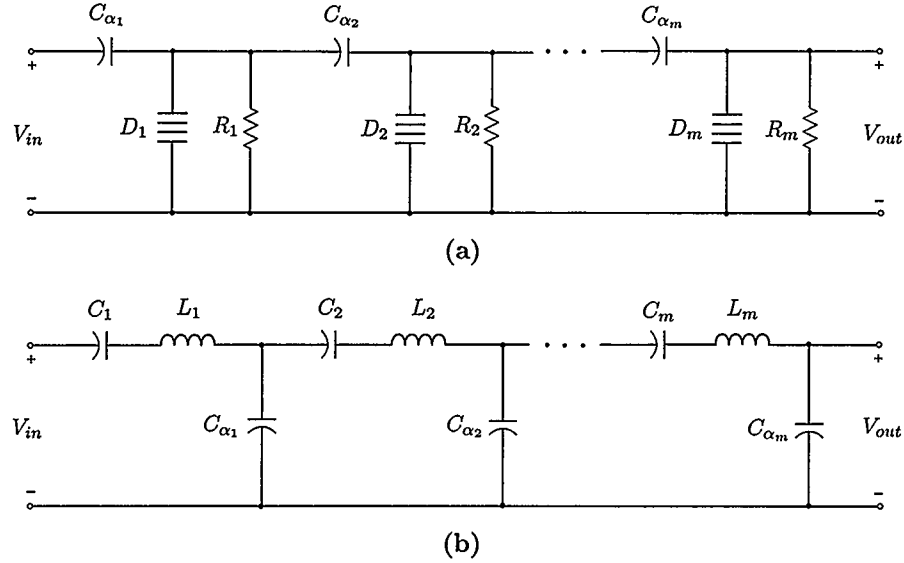


Figure 5.4:  $m^{\text{th}}$  order passive prototype models of Type I asymmetric-slope band-pass filter.

band-pass filter and the maximum number of fractional capacitor which can be used is  $m$  when all the resistors in Figure 5.2 and all the capacitors in Figure 5.3 are replaced by fractional-order capacitors.

### 5.2.1 Type I Asymmetric-Slope Band-pass Passive Prototypes

Figure 5.4(a) and 5.4(b) show  $m^{\text{th}}$  order passive prototypes Type I asymmetric-slope band-pass filters. The normal band-pass filter in Figure 5.3(a) converts to a Type I asymmetric-slope band-pass filter if at least one of the capacitors is replaced by a fractional capacitor of equal fractal capacitance and fractal order. Figure 5.4(a) shows passive prototype Type I asymmetric band-pass filter using maximum number of fractional capacitors,  $m$ . The transfer function of the proposed Type I FDNR based filter is given by

$$H_I(s) = \frac{aB^m s^{m[1-\frac{\alpha}{m}(1-\alpha)]}}{s^{2m} + \dots + aB^m s^{m[1-\frac{\alpha}{m}(1-\alpha)]} + \dots + \omega_o^{2m}} \quad (5.2)$$

Frequency	Type I FDNR-based	
	Slope (dB/dec)	$\phi$
$\omega \ll \omega_o$	$0 < 20m(1 - \frac{n}{m}(1 - \alpha)) < 20m$	$\frac{m\pi}{2}(1 - \frac{n}{m}(1 - \alpha))$
$\omega \gg \omega_o$	$20m < 20m(1 + \frac{n}{m}(1 - \alpha)) < 40m$	$-\frac{m\pi}{2}(1 + \frac{n}{m}(1 - \alpha))$

(a)

Frequency	Type I inductor-based	
	Slope (dB/dec)	$\phi$
$\omega \ll \omega_o$	$0 < 20m(1 - \frac{n}{m}\alpha) < 20m$	$\frac{m\pi}{2}(1 - \frac{n}{m}\alpha)$
$\omega \gg \omega_o$	$20m < 20m(1 + \frac{n}{m}\alpha) < 40m$	$-\frac{m\pi}{2}(1 + \frac{n}{m}\alpha)$

(b)

**Table 5.1:** Slopes for  $m^{\text{th}}$  order Type I asymmetric-slope band-pass filter.

where  $m$  is order of the filter,  $n$  is number of fractional-order capacitor used in the filter,  $B$  is the bandwidth,  $\omega_o$  is center frequency and  $a = \prod_{i=1}^m \frac{C_{\alpha_i}}{C_i}$ .

Likewise, the Type I passive prototype model in Figure 5.4(b) can be obtained from the normal band-pass filter in Figure 5.2(b) if each resistor is replaced by a fractional capacitor of equal fractal capacitance and fractal order. The transfer function of the filter is given by

$$H_{II}(s) = \frac{aB^m s^{m[1 - \frac{n}{m}\alpha]}}{s^{2m} + \dots + aB^m s^{m[1 - \frac{n}{m}\alpha]} + \dots + \omega_o^{2m}} \quad (5.3)$$

where  $m$  is order of the filter,  $n$  is number of fractional-order capacitor used in the filter,  $B$  is the bandwidth,  $\omega_o$  is center frequency and  $a = \prod_{i=1}^m \frac{1}{L_i C_{\alpha_i}}$ . Two different slopes and phases of the Type I FDNR-based filter in Figure 5.4(a) and inductor-based filter in Figure 5.4(b) are presented in Table 5.1. The phase of the filters was found empirically and verified using MATLAB.

Figure 5.5 shows the relationship between center frequency,  $\omega_3$  and  $\omega_4$  for the  $m^{\text{th}}$  order Type I FDNR-based asymmetric-slope band-pass filter.  $\omega_3$  and  $\omega_4$  are the stopband frequencies where the attenuation is maximum. With reference to Figure

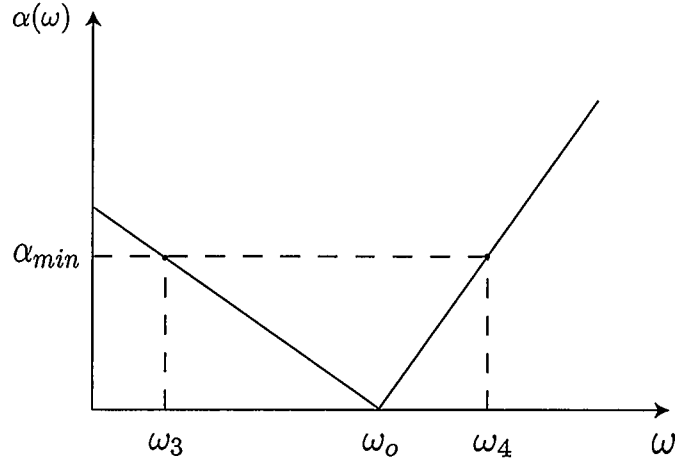


**Figure 5.5:**  $\omega_o$ ,  $\omega_3$  and  $\omega_4$  in the Type I asymmetric-slope band-pass filters.

5.5 and Table 5.1, we arrive at the following equation

$$\frac{\alpha_{min}}{\log\left(\frac{\omega_4}{\omega_o}\right)} = 20m\left(1 + \frac{n}{m}(1 - \alpha)\right) \quad (5.4)$$

which in turn yields

$$\alpha_{min} = 20m\left(1 + \frac{n}{m}(1 - \alpha)\right)\log\left(\frac{\omega_4}{\omega_o}\right) \quad (5.5)$$

for frequencies greater than  $\omega_o$ . Here,  $\alpha_{min}$  is the maximum attenuation in the stop-band. For frequencies less than  $\omega_o$ , we have the following equation

$$\frac{-\alpha_{min}}{\log\left(\frac{\omega_o}{\omega_3}\right)} = -20m\left(1 - \frac{n}{m}(1 - \alpha)\right) \quad (5.6)$$

which in turn yields

$$\alpha_{min} = 20m\left(1 - \frac{n}{m}(1 - \alpha)\right)\log\left(\frac{\omega_o}{\omega_3}\right) \quad (5.7)$$

The relationship between  $\omega_o$ ,  $\omega_3$  and  $\omega_4$  can then be found

$$\omega_o = \sqrt{\omega_3^{\left(1 - \frac{n}{m}(1 - \alpha)\right)} \omega_4^{\left(1 + \frac{n}{m}(1 - \alpha)\right)}} \quad (5.8)$$

by equating equations (5.5) and (5.7).

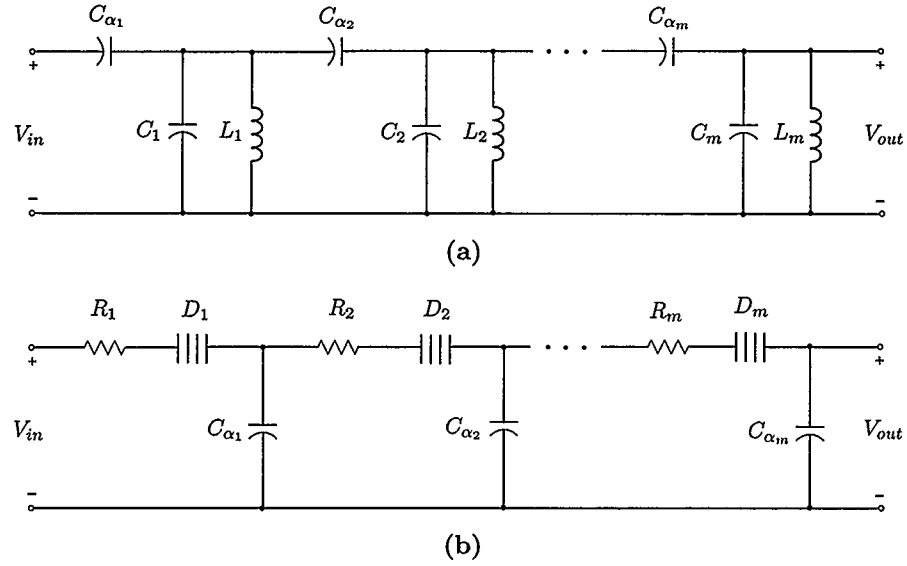


**Figure 5.6:**  $m^{\text{th}}$  order passive prototype models of Type II asymmetric-slope band-pass filter.

For the Type I  $m^{\text{th}}$  order inductor-based asymmetric-slope band-pass filter, the center frequency is given by

$$\omega_o = \sqrt{\omega_3^{(1-\frac{n}{m}\alpha)} \omega_4^{(1+\frac{n}{m}\alpha)}} \quad (5.9)$$

using the same method.

### 5.2.2 Type II Asymmetric-Slope Band-pass Passive Prototypes

Consider the  $m^{\text{th}}$  order passive prototypes Type II asymmetric-slope band-pass filter shown in Figures 5.6(a) and 5.6(b). Normal band-pass filter in Figure 5.2(a) converts to Type II asymmetric-slope band-pass filter if at least one of the resistors is replaced by a fractional capacitor of equal fractal capacitance and fractal order  $\alpha$ . Figure 5.6(a) shows passive prototype Type II asymmetric band-pass filter using maximum number of fractional capacitors. The transfer function of the proposed Type II inductor based

Frequency	Type II inductor-based	
	Slope (dB/dec)	$\phi$
$\omega \ll \omega_o$	$20m < 20m(1 + \frac{n}{m}\alpha) < 40m$	$\frac{m\pi}{2}(1 + \frac{n}{m}\alpha)$
$\omega \gg \omega_o$	$0 < 20m(1 - \frac{n}{m}\alpha) < 20m$	$\frac{m\pi}{2}(\frac{n}{m}\alpha - 1)$

(a)

Frequency	Type II FDNR-based	
	Slope (dB/dec)	$\phi$
$\omega \ll \omega_o$	$20m < 20m(1 + \frac{n}{m}(1 - \alpha)) < 40m$	$\frac{m\pi}{2}(1 + \frac{n}{m}(1 - \alpha))$
$\omega \gg \omega_o$	$0 < 20m(1 - \frac{n}{m}(1 - \alpha)) < 20m$	$\frac{m\pi}{2}(\frac{n}{m}(1 - \alpha) - 1)$

(b)

**Table 5.2:** Slopes for Type II  $m^{\text{th}}$  order asymmetric-slope band-pass filter.

filter is given by

$$H_{III}(s) = \frac{aB^m s^{m[1+\frac{n}{m}\alpha]}}{s^{2m} + \dots + aB^m s^{m[1+\frac{n}{m}\alpha]} + \dots + \omega_o^{2m}} \quad (5.10)$$

where  $m$  is order of the filter,  $n$  is number of fractional-order capacitor used in the filter,  $B$  is bandwidth,  $\omega_o$  is the center frequency and  $a = \prod_{i=1}^m \frac{C_{\alpha_i}}{C_i}$ .

Likewise, the Type II passive prototype in Figure 5.6(b) can be obtained from the normal band-pass filter in Figure 5.3(b) if each capacitor in Figure 5.3(b) is replaced by a fractional capacitor of equal fractal capacitance and fractal order.

The transfer function of the filter is given by

$$H_{IV}(s) = \frac{aB^m s^{m[1-\frac{n}{m}(\alpha-1)]}}{s^{2m} + \dots + aB^m s^{m[1-\frac{n}{m}(\alpha-1)]} + \dots + \omega_o^{2m}} \quad (5.11)$$

where  $m$  is order of the filter,  $n$  is number of fractional-order capacitor used in the filter,  $B$  is the bandwidth,  $\omega_o$  is the center frequency and  $a = \prod_{i=1}^m \frac{1}{L_i C_{\alpha_i}}$ . Table 5.2 shows the slopes and phases of the proposed Type II inductor-based filter in Figure 5.6(a) and FDNR-based filter in Figure 5.6(b).

It is to be noted that the maximum number of fractional capacitor is used in all

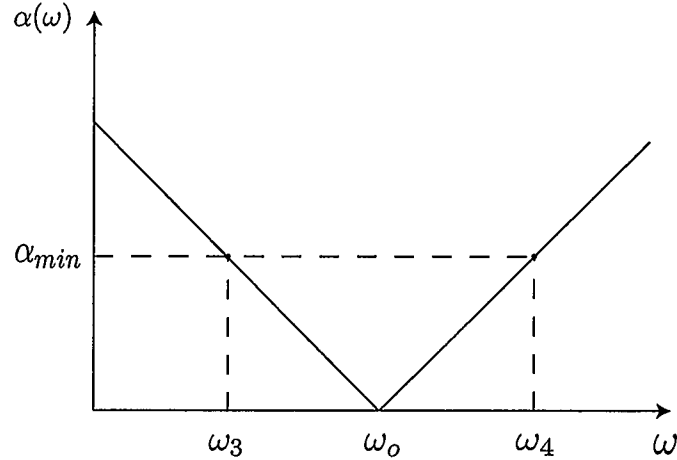


**Figure 5.7:**  $\omega_o$ ,  $\omega_3$  and  $\omega_4$  in the Type II asymmetric-slope band-pass filters.

four circuits in Figures 5.4 and 5.6.

Figure 5.7 shows the relationship between center frequency,  $\omega_3$  and  $\omega_4$  for the  $m^{\text{th}}$  order Type II inductor-based asymmetric-slope band-pass filter. With reference to Figure 5.7 and Table 5.2, we arrive at the following equation

$$\frac{\alpha_{min}}{\log\left(\frac{\omega_4}{\omega_o}\right)} = 20m\left(1 - \frac{n}{m}\alpha\right) \quad (5.12)$$

which in turn yields

$$\alpha_{min} = 20m\left(1 - \frac{n}{m}\alpha\right)\log\left(\frac{\omega_4}{\omega_o}\right) \quad (5.13)$$

at frequencies greater than  $\omega_o$ . For frequencies less than  $\omega_o$ , we have the following equation

$$\frac{-\alpha_{min}}{\log\left(\frac{\omega_o}{\omega_3}\right)} = -20m\left(1 + \frac{n}{m}\alpha\right) \quad (5.14)$$

which in turn yields

$$\alpha_{min} = 20m\left(1 + \frac{n}{m}\alpha\right)\log\left(\frac{\omega_o}{\omega_3}\right) \quad (5.15)$$

The relationship between  $\omega_o$ ,  $\omega_3$  and  $\omega_4$  can then be found

$$\omega_o = \sqrt{\omega_3^{(1+\frac{n}{m}\alpha)} \omega_4^{(1-\frac{n}{m}\alpha)}} \quad (5.16)$$

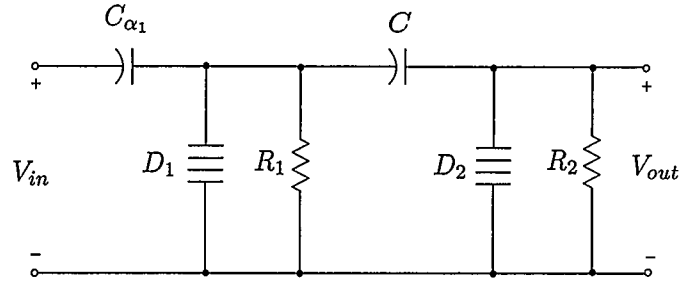


**Figure 5.8:** Passive prototype model of a fourth order Type I FDNR-based filter using one fractional capacitor.

by equating equations (5.13) and (5.15).

For the Type II  $m^{\text{th}}$  order FDNR-based asymmetric-slope band-pass filter, the center frequency is given by

$$\omega_o = \sqrt{\omega_3^{(1+\frac{n}{m}(1-\alpha))} \omega_4^{(1-\frac{n}{m}(1-\alpha))}} \quad (5.17)$$

using the same method.

Finally, it is clear from Table 5.1 that increasing the number of fractional capacitors in the Type I FDNR and inductor based filters decreases the slope at low frequencies and increases it at high frequencies. On the other hand, Table 5.2 reveals that having greater number of fractional capacitors in the Type II filters leads to sharper slopes at low frequencies and slighter slopes at high frequencies.

### 5.3 Fourth-Order Asymmetric-Slope Band-pass Filter

#### 5.3.1 Fourth-Order Type I FDNR-Based Filter

##### 5.3.1.1 Passive Prototype

Consider the fourth order passive prototype Type I filter shown in Figure 5.8 which deploys only one fractional capacitor. The transfer function of this filter is

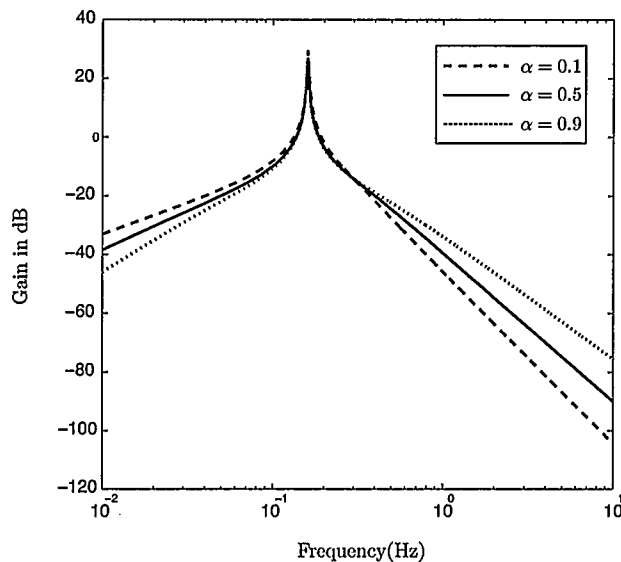


**Figure 5.9:** Magnitude response of the proposed fourth-order Type I filter in (5.18) to various values of  $\alpha$ .

$$H_I(s) = \frac{ds^{1+\alpha}}{s^4 + as^3 + bs^{2+\alpha} + cs^2 + ds^{1+\alpha} + es + fs^\alpha + g} \quad (5.18)$$

where  $a = \frac{C(D_1+D_2)}{D_1D_2}$ ,  $b = \frac{C_{\alpha_1}}{D_1}$ ,  $c = \frac{R_1D_1+R_2D_2}{R_1R_2D_1D_2}$ ,  $d = \frac{CC_{\alpha_1}}{D_1D_2}$ ,  $e = \frac{C(R_1+R_2)}{R_1R_2D_1D_2}$ ,  $f = \frac{C_{\alpha_2}}{R_2D_1D_2}$  and  $g = \frac{1}{R_1R_2D_1D_2}$ . The transfer function converts to

$$\hat{H}_I(s) = \frac{cs^{2\alpha}}{s^4 + as^{2+\alpha} + bs^2 + cs^{2\alpha} + ds^\alpha + e} \quad (5.19)$$

if  $C$  is replaced by another fractional capacitor ( $C_{\alpha_2}$ ) with the same fractal order in Figure 5.8. Here,  $a = \frac{(C_{\alpha_1}D_1+C_{\alpha_2}D_1+C_{\alpha_2}D_2)}{D_1D_2}$ ,  $b = \frac{R_1D_1+R_2D_2}{R_1R_2D_1D_2}$ ,  $c = \frac{C_{\alpha_1}C_{\alpha_2}}{D_1D_2}$ ,  $d = \frac{(R_1C_{\alpha_1}+R_1C_{\alpha_2}+R_2C_{\alpha_2})}{R_1R_2D_1D_2}$  and  $e = \frac{1}{R_1R_2D_1D_2}$ . Figure 5.9 shows the magnitude response for the filter in (5.18) at  $a = c = e = 2$ ,  $b = f = 1.5$ ,  $d = 0.05$  and  $g = 1$ .

The step response of the filter can be obtained by substituting for the non-integer Laplacian operator  $s^\alpha$  with the the equation (3.1). Figure 5.10 shows the step response of the fourth order FDNR-based filter in (5.19) at  $a = b = d = 2$ ,  $c = e = 1$  and  $\alpha = 0.5$ .

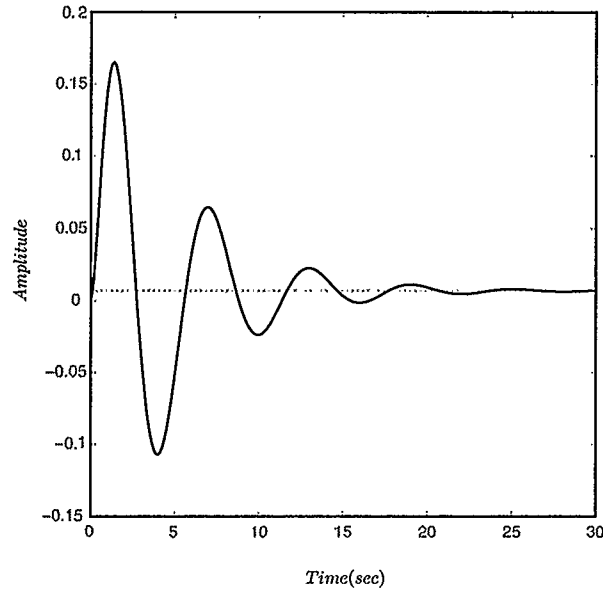


**Figure 5.10:** Step response of the fourth order FDNR based filter in (5.19) at  $a = b = d = 2$ ,  $c = e = 1$  and  $\alpha = 0.5$ .

### 5.3.1.2 Simulation and Experimental Results

The circuit of Figure 5.8 can be easily realized actively by appropriately replacing the FDNR by their active realizations which can employ operational amplifiers (opamps) [2], OTAs [6], current conveyors [29, 30], Active-R [33] and even hybrid realizations [35]. In the case of the Type I realization one such realization that uses opamps is shown in Figure 5.11 which employs a GIC based FDNR, connected to the passive filter section which employs the resistor  $R_1$ , the capacitor  $C_1$  and the fractional-order capacitor  $C_\alpha$ . The proposed filter was simulated in SPICE using LT1364 opamps (rated bandwidth 70MHz) biased with  $\pm 15V$  supplies. Carlson's method [7] was used once again to simulate the fractional-order capacitor  $C_\alpha$  having  $C = 1\mu F$  and  $\alpha = 0.5$ . The values of the capacitors and resistors in the approximated model shown in Table 3.1 were calculated such that  $C_\alpha$  has an operating range of  $100Hz - 10kHz$ . Figure 5.12 shows the simulation results for the fourth order Type I FDNR-based circuit of Figure 5.11 taking  $R_1 = 1.5k\Omega$ ,  $R = 1.68k\Omega$ ,  $C = 0.1\mu F$  and  $C_1 = 0.01\mu F$ . The

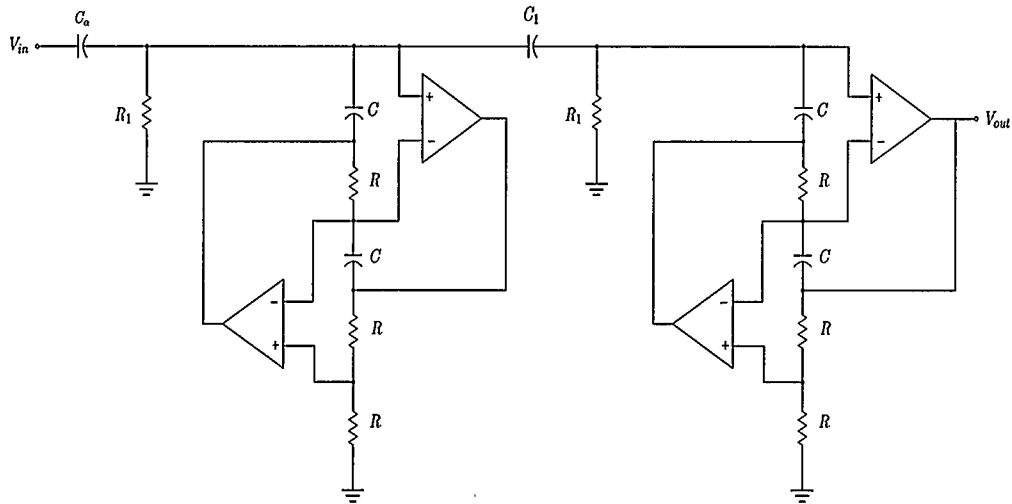


**Figure 5.11:** Possible realization of fourth-order Type I FDNR-based asymmetric-slope band-pass filter.

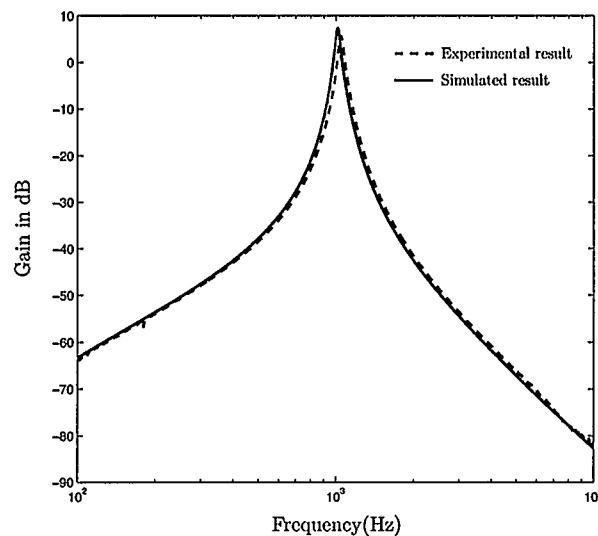


**Figure 5.12:** SPICE and experimental results of the filter in Figure 5.11.

expected quality factor and center frequency were  $Q = 25.15$  and  $\omega_o = 1kHz$ . The circuit was also constructed on breadboard and tested. Experimental result for the circuit is also shown within Figure 5.12. The slope at frequencies lower than  $f_o$  was measured as  $30 dB/dec$  while it was measured as  $-50 dB/dec$  at frequencies greater than  $f_o$  confirming the asymmetric nature of the band-pass filters and the accuracy of realizing Table 5.1(a). The measured  $(Q, f_o)$  for the circuit were  $(23, 1.04kHz)$ .

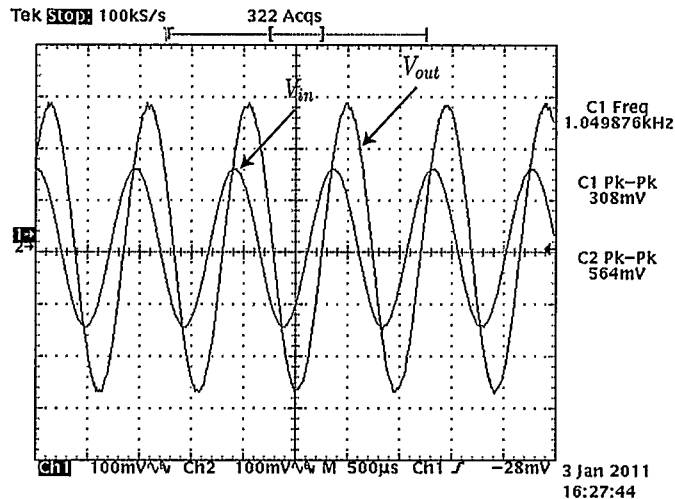


**Figure 5.13:** Measured transient response of the fourth order Type I FDNR-based band-pass filter in Figure 5.11 confirming stability at  $\alpha = 0.5$ .

To confirm stability, the steady state transient response of the filter in Figure 5.11 is shown in Figure 5.13.

The fourth order Type I transfer function in (5.19) was tested experimentally using an AN231E04 FPAA from Anadigm [45]. Substituting (3.1) into (5.19) yields an eighth order transfer function which can be written in the form

$$H_I(s) = G_I \frac{1}{(s^2 + \frac{\omega_{p1}}{Q_{p1}}s + \omega_{p1})(s^2 + \frac{\omega_{p2}}{Q_{p2}}s + \omega_{p2})} \frac{(s^2 + \frac{\omega_{z1}}{Q_{z1}}s + \omega_{z1})(s^2 + \frac{\omega_{z2}}{Q_{z2}}s + \omega_{z2})}{(s^2 + \frac{\omega_{p3}}{Q_{p3}}s + \omega_{p3})(s^2 + \frac{\omega_{p4}}{Q_{p4}}s + \omega_{p4})} \quad (5.20)$$

after replacing  $s$  with  $s/\omega_o$  where  $\omega_o = \omega_{p1}\omega_{p2}\omega_{p3}\omega_{p4}$ . This rearrangement in bi-quadratic terms is needed for the FPAA realization. The eighth order transfer function in (5.20) can be tested in FPAA using four biquadratic filter CAMs cascaded and wired together to the desired input and output ports in the AnadigmDesigner design environment as shown in Figure 5.14. Two biquadratic filters were setup in the low-pass configuration and two of them were setup in the pole-zero configuration. Figure 5.15 shows the experimental result realizing a filter with  $(\alpha, a, b, c, d, e) = (0.1, 2, 2, 2, 2, 1)$  which theoretically yields  $Q = 30.5$  and  $f_o = 53kHz$ . With reference to (5.19), the zeros quality factor and center frequency in

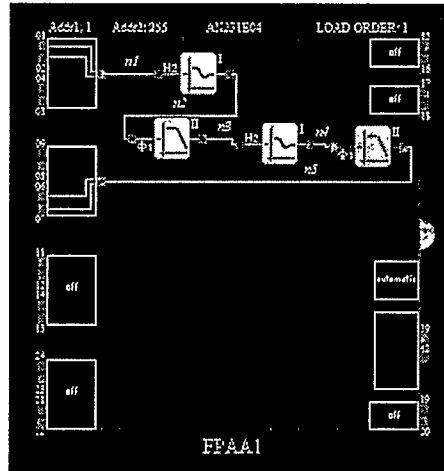


Figure 5.14: Approximated fourth order Type I band-pass filter in (5.20) using four biquadratic filter CAMs.

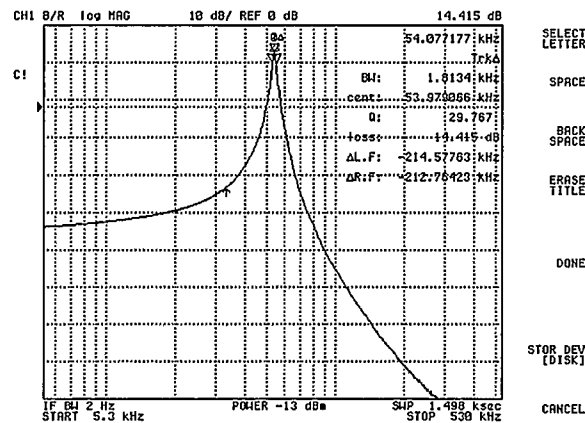
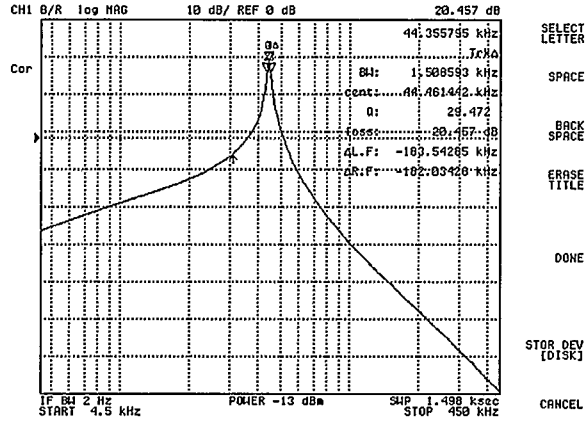


Figure 5.15: Experimental result using an FPAA for fourth order Type I asymmetric-slope filter in (5.19) with  $\alpha = 0.1$ ,  $Q = 30.5$ .

$kHz$  are respectively  $(Q_{z_1}, \omega_{z_1}, Q_{z_2}, \omega_{z_2}) = (0.249, 32.694, 0.249, 32.694)$ , the poles quality factor and center frequency in  $kHz$  are  $(Q_{p_1}, \omega_{p_1}, Q_{p_2}, \omega_{p_2}, Q_{p_3}, \omega_{p_3}, Q_{p_4}, \omega_{p_4}) = (5.16, 54.168, 29.36, 54.213, 0.499, 162.68, 0.499, 10.322)$  and  $G_I = 0.44$ . The measured quality factor was 29.767 and the center frequency  $f_o$  was 54.077kHz which are very close to the expected values. It is important to note here that the pole and zero values of (5.20) are rounded off by the FPAA.

Another design example for  $(\alpha, a, b, c, d, e) = (0.5, 2, 2, 1, 2.28, 1)$  with  $Q = 31$



**Figure 5.16:** Experimental result using an FPAA for fourth order Type I asymmetric-slope filter in (5.19) with  $\alpha = 0.1$ ,  $Q = 30.5$ .

and  $f_o = 45kHz$  is shown in Figure 5.16. With reference to (5.19), the zeros quality factor and center frequency in  $kHz$  are respectively  $(Q_{z_1}, \omega_{z_1}, Q_{z_2}, \omega_{z_2}) = (0.223, 13.41, 0.223, 13.41)$ , the poles quality factor and center frequency in  $kHz$  are  $(Q_{p_1}, \omega_{p_1}, Q_{p_2}, \omega_{p_2}, Q_{p_3}, \omega_{p_3}, Q_{p_4}, \omega_{p_4}) = (0.5, 9.79, 0.5, 270.4, 1.07, 43.26, 30.19, 44.7)$  and  $G_{II} = 0.933$ . The measured quality factor and center frequency were  $Q = 29.472$  and  $f_o = 44.355kHz$  which are very close to the theoretical values.

### 5.3.2 Fourth Order Type I inductor-Based Filter

#### 5.3.2.1 Passive Prototype

Consider the fourth order passive prototype Type I filter shown in Figure 5.17 which deploys only one fractional capacitor. The transfer function of the filter is

$$H_{II}(s) = \frac{ds^{2-\alpha}}{s^4 + as^3 + bs^{3-\alpha} + cs^2 + ds^{2-\alpha} + es + fs^{1-\alpha} + g} \quad (5.21)$$

where  $a = \frac{R}{L_2}$ ,  $b = \frac{L_1 + L_2}{L_1 L_2 C_{\alpha_1}}$ ,  $c = \frac{L_1 C_1 + L_2 L_2}{L_1 L_2 C_1 C_2}$ ,  $d = \frac{R}{L_1 L_2 C_{\alpha}}$ ,  $e = \frac{R}{L_1 L_2 C_1}$ ,  $f = \frac{C_1 + C_2}{L_1 L_2 C_1 C_2 C_{\alpha}}$  and  $g = \frac{1}{L_1 L_2 C_1 C_2}$ . The transfer function in (5.21) can be obtained from the Type I transfer function in (5.18) if  $\alpha$  is replaced by  $1 - \alpha$ . We have the following transfer

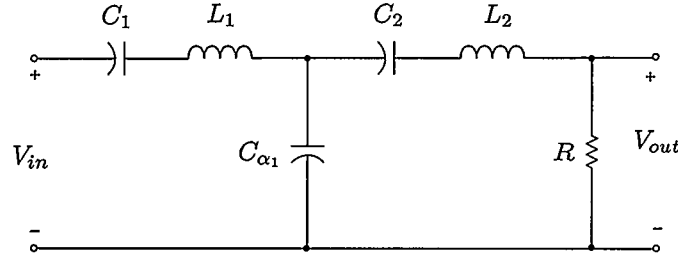


**Figure 5.17:** Passive prototype model of fourth order Type I inductor-based filter using one fractional capacitor.

function for the fourth order passive prototype model in (5.17) if  $R$  is replaced by a fractional order capacitor ( $C_{\alpha_2}$ ) with the same fractal order

$$H_{II}^{\wedge}(s) = \frac{cs^{2-2\alpha}}{s^4 + as^{3-\alpha} + bs^2 + cs^{2-2\alpha} + ds^{1-\alpha} + e} \quad (5.22)$$

where  $a = \frac{(L_1C_{\alpha_1} + L_1C_{\alpha_2} + L_2C_{\alpha_2})}{L_1L_2C_{\alpha_1}C_{\alpha_2}}$ ,  $b = \frac{L_1C_1 + L_2C_2}{L_1L_2C_1C_2}$ ,  $c = \frac{1}{L_1L_2C_1C_2}$ ,  $d = \frac{(C_1C_{\alpha_2} + C_1C_{\alpha_1} + C_2C_{\alpha_2})}{L_1L_2C_1C_2C_{\alpha_1}C_{\alpha_2}}$  and  $e = \frac{1}{L_1L_2C_1C_2}$ . Likewise, it is worth noting that the transfer function in (5.22) can be obtained from the transfer function in (5.19) if  $\alpha$  is replaced by  $1 - \alpha$ . Figure 5.18 shows the magnitude response of the filter in (5.21) at  $a = c = e = 2$ ,  $b = f = 1.5$ ,  $d = 0.05$  and  $g = 1$ . The step response of the filter can be obtained by substituting for the non-integer Laplacian operator  $s^\alpha$  with the equation in (3.1) into transfer functions in (5.21) and (5.22). Clearly the step response of the Type I FDNR based filters in (5.18) and (5.19) can be used for the fourth order Type I inductor-based filter if for the identical  $a, b, c, d, e, f$  and  $g$ ,  $\alpha$  is replaced by  $1 - \alpha$ . Therefore, Figure 5.10 shows the step response of fourth order filter in (5.22) at  $a = b = d = 2$ ,  $c = e = 1$  and  $\alpha = 0.5$ .

### 5.3.2.2 Simulation and Experimental Results

The fourth order Type I inductor based circuit using a floating inductor based on Riordan technique is shown in Figure 5.19 [38]. The circuit was first simulated using LT1364 opamps (rated bandwidth 70MHz) biased with  $\pm 15V$  supplies in SPICE

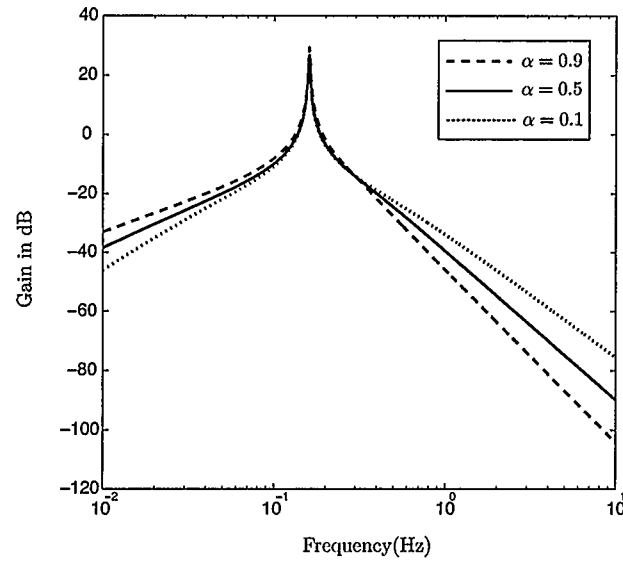


**Figure 5.18:** Magnitude response of the proposed fourth-order Type I filter in (5.21) to various values of  $\alpha$ .

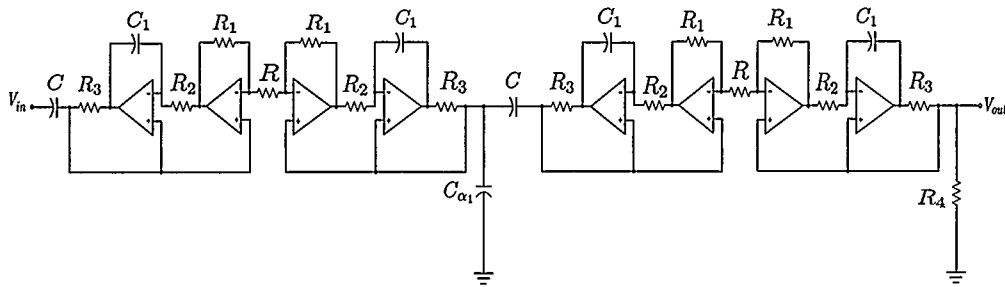


**Figure 5.19:** Possible realization of fourth-order Type I inductor-based asymmetric-slope band-pass filter.

as shown in Figure 5.20. The fractional-order capacitor  $C_\alpha$  having  $C = 1\mu F$  and  $\alpha = 0.5$  was approximated by Carlson's method such that it has an operating range of  $100Hz - 10kHz$ . The value of components in the approximated model is shown in Table 3.1.

The circuit was constructed on breadboard and tested. The comparison between simulation and experimental results taking  $R = R_3 = 6k\Omega$ ,  $R_1 = R_2 = 4k\Omega$ ,  $R_4 = 8k\Omega$ ,  $C = 2.2nF$  and  $C_1 = 0.33\mu F$  is also shown in Figure 5.20. The expected quality factor and center frequency were  $Q = 22$  and  $\omega_o = 1kHz$ . The slope at frequencies

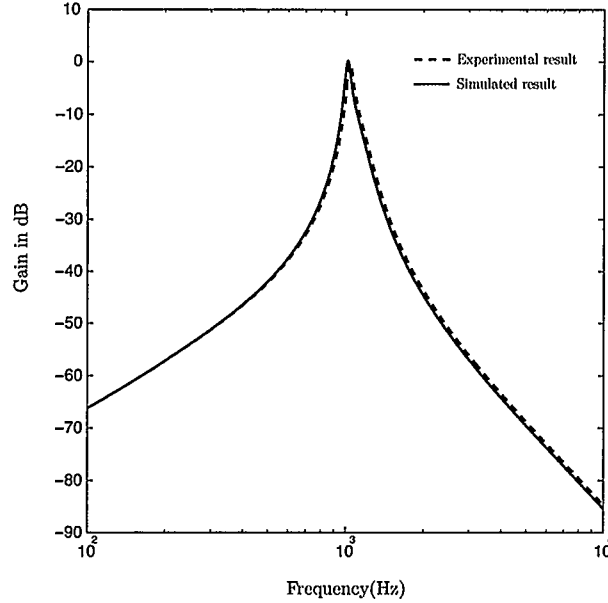


**Figure 5.20:** SPICE and experimental results of the filter in Figure 5.19.

lower than  $f_o$  was measured as  $30 \text{ dB/dec}$  while it was measured as  $-50 \text{ dB/dec}$  at frequencies greater than  $f_o$  confirming the asymmetric nature of the band-pass filter and the accuracy of realizing Table 5.1(b). The measured  $(Q, f_o)$  for the circuit were  $(18.2, 1.04 \text{ kHz})$ . To confirm stability, the steady state transient response of the filter in Figure 5.19 is shown in Figure 5.21.

### 5.3.3 Fourth Order Type II Inductor-Based Filter

#### 5.3.3.1 Passive Prototype

Consider the fourth order passive prototype Type II filter shown in Figure 5.22 which deploys only one fractional capacitor and grounded inductors. The transfer function of the proposed passive prototype is

$$H_{III}(s) = \frac{cs^{2+\alpha}}{s^4 + as^{3+\alpha} + bs^3 + cs^{2+\alpha} + ds^2 + es^{1+\alpha} + fs + g} \quad (5.23)$$

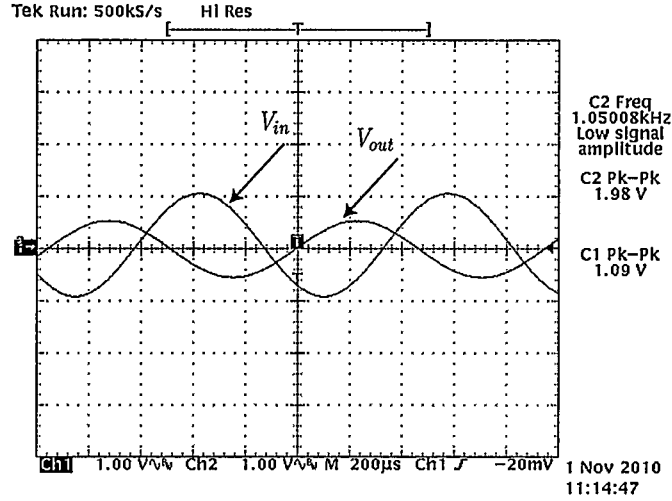


Figure 5.21: Measured transient response of the fourth order Type I inductor-based band-pass filter in Figure 5.19 confirming stability at  $\alpha = 0.5$ .

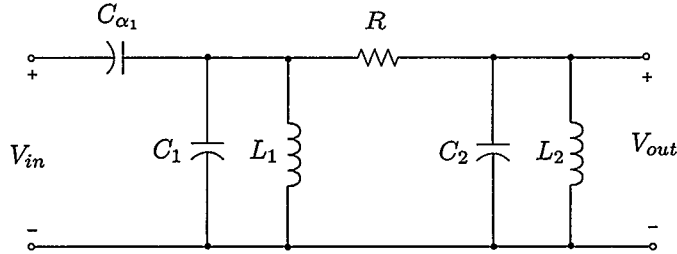


Figure 5.22: Passive prototype model of fourth order Type II inductor-based filter using one fractional capacitor.

where  $a = \frac{C_{\alpha_1}}{C_1}$ ,  $b = \frac{C_1 + C_2}{RC_1C_2}$ ,  $c = \frac{C_{\alpha_1}}{RC_1C_2}$ ,  $d = \frac{L_1C_1 + L_2C_2}{L_1L_2C_1C_2}$ ,  $e = \frac{C_{\alpha_1}}{L_2C_1C_2}$ ,  $f = \frac{L_1 + L_2}{RL_1L_2C_1C_2}$  and  $g = \frac{1}{L_1L_2C_1C_2}$ . The transfer function converts to

$$H_{III}(s) = \frac{bs^{2+2\alpha}}{s^4 + as^{3+\alpha} + bs^{2+2\alpha} + cs^2 + ds^{1+\alpha} + e} \quad (5.24)$$

if  $R$  is replaced by another fractional capacitor ( $C_{\alpha_2}$ ) with the same fractal order in Figure 5.22. Here,  $a = \frac{(C_1C_{\alpha_1} + C_2C_{\alpha_1} + C_2C_{\alpha_2})}{C_1C_2}$ ,  $b = \frac{C_{\alpha_1}C_{\alpha_2}}{C_1C_2}$ ,  $c = \frac{L_1C_1 + L_2C_2}{L_1L_2C_1C_2}$ ,  $d = \frac{(L_1C_{\alpha_1} + L_1C_{\alpha_2} + L_2C_{\alpha_2})}{L_1L_2C_1C_2}$  and  $e = \frac{1}{L_1L_2C_1C_2}$ . Figure 5.23 shows the magnitude response for the filter in (5.23) at  $a = e = 0.5$ ,  $b = d = f = 2$ ,  $c = 0.05$  and  $g = 1$ .

The step response of the filter can be obtained by substituting for the non-integer

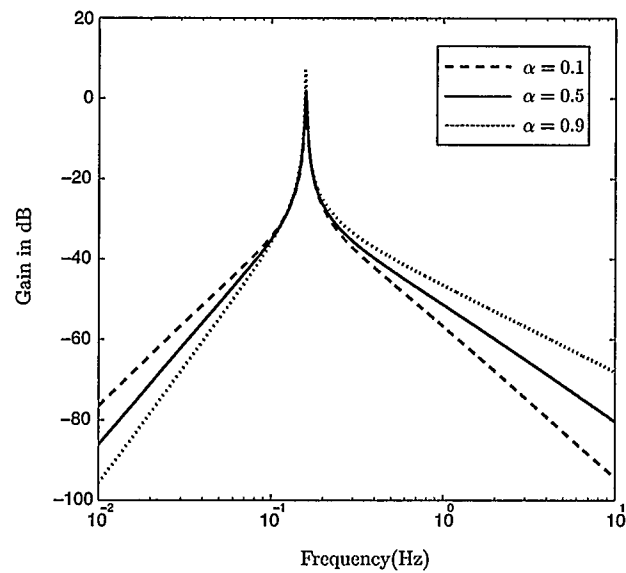


**Figure 5.23:** Magnitude response of the proposed fourth-order Type II filter in (5.23) to various values of  $\alpha$ .

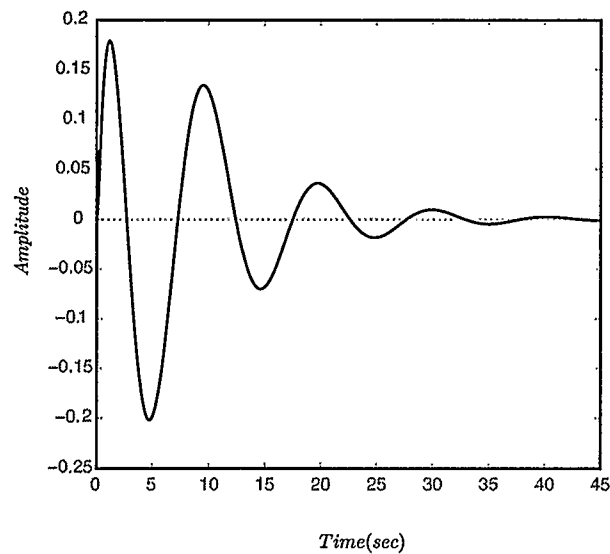


**Figure 5.24:** Step response of the fourth order inductor based filter in (5.24) at  $a = b = d = 2$ ,  $c = e = 1$  and  $\alpha = 0.5$ .

Laplacian operator  $s^\alpha$  with the the equation in (3.1) into the transfer functions in (5.23) and (5.24). Figure 5.24 shows the step response of the fourth order Type II inductor-based filter in (5.24) at  $a = b = d = 2$ ,  $c = e = 1$  and  $\alpha = 0.5$

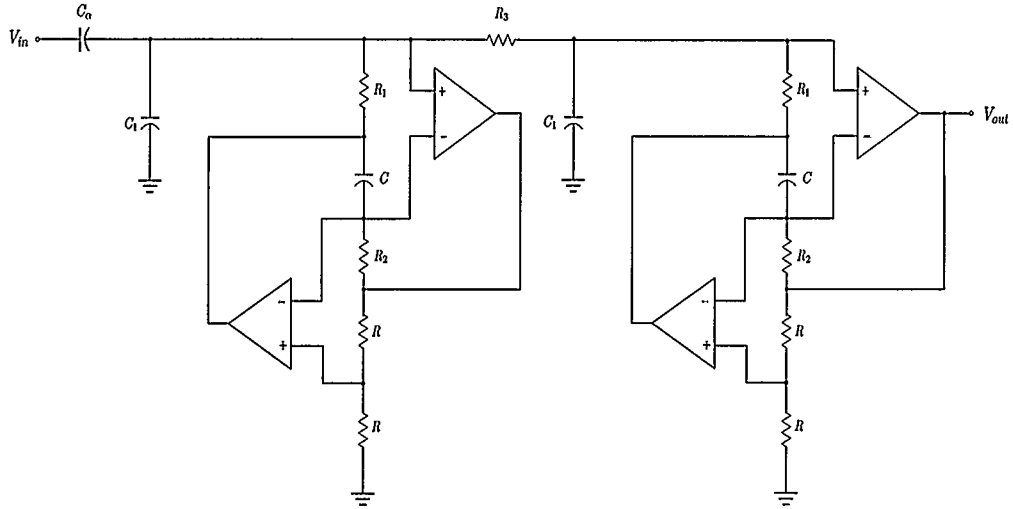


**Figure 5.25:** Possible realization of fourth-order Type II inductor-based asymmetric-slope band-pass filter.

### 5.3.3.2 Simulation and Experimental Results

The fourth order Type II realization using grounded inductor of the Antonio GIC variety whose impedance is  $Z_i = R_1 R_2 C s$  and one fractional-order capacitor is shown in Figure 5.25. The proposed filter was simulated in SPICE using LT1364 opamps biased with  $\pm 15V$  supplies. Carlson's method [7] was used to simulate the fractional-order capacitor  $C_\alpha$  having  $C = 1\mu F$  and  $\alpha = 0.5$ , as shown in Figure 3.1. Figure 5.26 shows the simulation result for the fourth order Type II inductor-based circuit of Figure 5.25 taking  $R_1 = R_2 = R = 1.5k\Omega$ ,  $R_3 = 100\Omega$  and  $C_1 = 0.1\mu F$ . The expected quality factor and center frequency were  $Q = 22$  and  $\omega_o = 1kHz$ . Experimental result for the circuit is also shown within Figure 5.26. The slope at frequencies lower than  $f_o$  was measured as  $50 dB/dec$  while it was measured as  $-30 dB/dec$  at frequencies greater than  $f_o$  confirming the asymmetric nature of the band-pass filter and the accuracy of realizing Table 5.2(a). The measured  $(Q, f_o)$  for the circuit were  $(19.798, 1.066kHz)$ , respectively. To confirm stability, the steady state transient response of the filter in Figure 5.25 is shown in Figure 5.27.

The fourth order Type II transfer function in (5.24) was tested experimentally

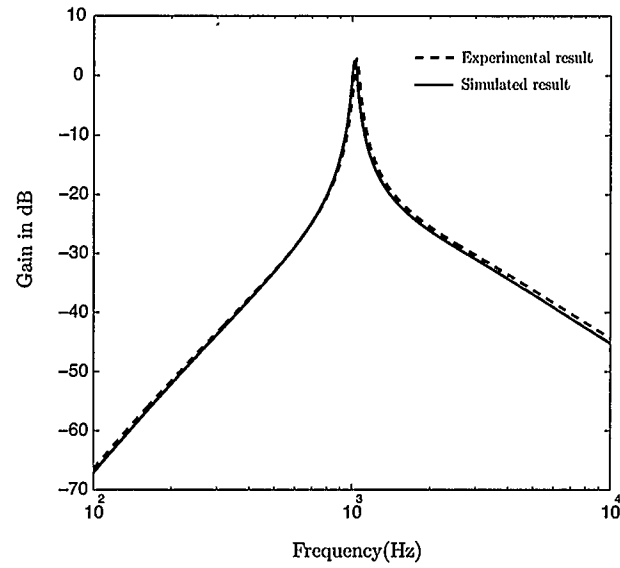


Figure 5.26: SPICE and experimental results of the filter in Figure 5.25.

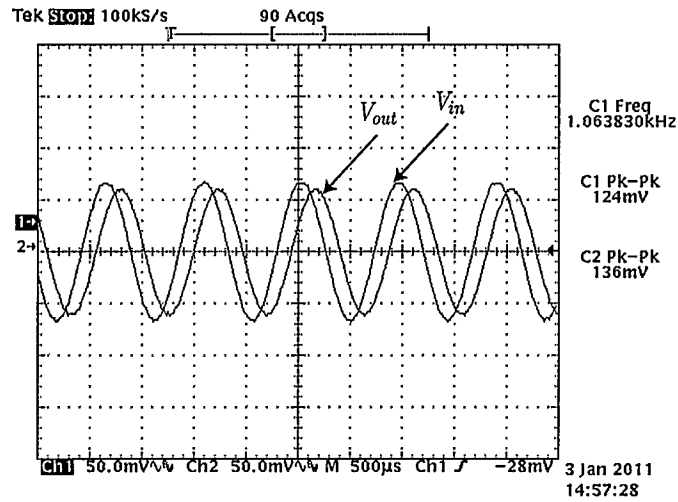


Figure 5.27: Measured transient response of the fourth order Type II inductor-based band-pass filter in Figure 5.25 confirming stability at  $\alpha = 0.5$ .

using AN231E04 FPAA from Anadigm [45]. Substituting (3.1) into (5.24) yields an eighth order transfer function which can be written in the form

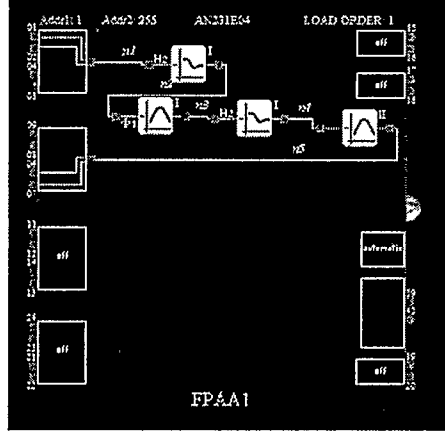
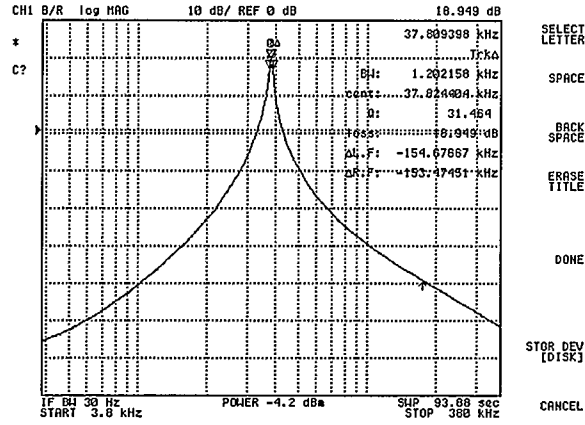


Figure 5.28: Approximated fourth order Type II band-pass filter in (5.25) using four biquadratic filter CAMs.

$$H_{III}^{\hat{}}(s) = G_{III} \frac{s^2}{(s^2 + \frac{\omega_{p1}}{Q_{p1}}s + \omega_{p1})(s^2 + \frac{\omega_{p2}}{Q_{p2}}s + \omega_{p2})} \frac{(s^2 + \frac{\omega_{z1}}{Q_{z1}}s + \omega_{z1})(s^2 + \frac{\omega_{z2}}{Q_{z2}}s + \omega_{z2})}{(s^2 + \frac{\omega_{p3}}{Q_{p3}}s + \omega_{p3})(s^2 + \frac{\omega_{p4}}{Q_{p4}}s + \omega_{p4})} \quad (5.25)$$

after replacing  $s$  with  $s/\omega_o$  where  $\omega_o = \omega_{p1}\omega_{p2}\omega_{p3}\omega_{p4}$ . The eighth order transfer function in (5.25) can be tested by FPAA using four biquadratic filter CAMs cascaded and wired to the desired input and output ports in the AnadigmDesigner design environment as shown in Figure 5.28. Two biquadratic filters were setup in the band-pass configuration and two of them were setup in the pole-zero configuration. Figure 5.29 shows the experimental result realizing a filter with  $(\alpha, a, b, c, d, e) = (0.1, 0.5, 0.015, 2, 0.5, 1)$  which theoretically yields  $Q = 32$  and  $f_o = 38kHz$ . With reference to (5.25), the zeros quality factor and center frequency in  $kHz$  are respectively  $(Q_{z1}, \omega_{z1}, Q_{z2}, \omega_{z2}) = (0.249, 32.694, 0.249, 32.694)$ , the poles quality factor and center frequency in  $kHz$  are respectively  $(Q_{p1}, \omega_{p1}, Q_{p2}, \omega_{p2}, Q_{p3}, \omega_{p3}, Q_{p4}, \omega_{p4}) = (2.17, 36.529, 31.562, 37.508, 0.499, 169, 0.499, 12.028)$  and  $G_{III} = 1.984$ . The measured quality factor was 31.464 and the center frequency  $f_o$  was 37.8kHz which are very close to the expected values. The slope at frequencies lower than  $f_o$  was 44 dB/dec while it was measured as 36 dB/dec at frequencies greater than  $f_o$  which



**Figure 5.29:** Experimental result using an FPAA for fourth order Type II asymmetric-slope band-pass filter in (5.24) with  $\alpha = 0.1$ ,  $Q = 32$ .

yields an almost symmetric characteristics about  $f_o$  because of small  $\alpha$ .

Another design example for  $(\alpha, a, b, c, d, e) = (0.5, 0.1, 0.01, 2, 0.1, 1)$  with  $Q = 42$  and  $f_o = 38kHz$  is shown in Figure 5.30. With reference to (5.25), the zeros quality factor and center frequency in  $kHz$  are respectively  $(Q_{z_1}, \omega_{z_1}, Q_{z_2}, \omega_{z_2}) = (0.223, 16.994, 0.223, 16.994)$ , the poles quality factor and center frequency in  $kHz$  are  $(Q_{p_1}, \omega_{p_1}, Q_{p_2}, \omega_{p_2}, Q_{p_3}, \omega_{p_3}, Q_{p_4}, \omega_{p_4}) = (0.5, 368, 0.5, 20.306, 10.311, 38.506, 44.227, 36.23)$  and  $G_{III} = 0.933$ . The measured quality factor and center frequency were  $Q = 40.801$  and  $f_o = 36.052kHz$  which are very close to the theoretical values.

### 5.3.4 Fourth Order Type II FDNR-based Filter

#### 5.3.4.1 Passive Prototype

Consider the fourth order passive prototype Type II filter shown in Figure 5.31 which deploys only one fractional capacitor. The transfer function of the proposed passive prototype is

$$H_{IV}(s) = \frac{cs^{3-\alpha}}{s^4 + as^{4-\alpha} + bs^3 + cs^{3-\alpha} + ds^2 + es^{2-\alpha} + fs + g} \quad (5.26)$$

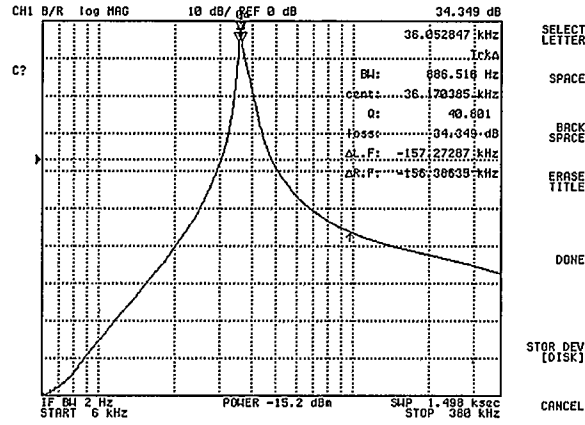


**Figure 5.30:** Experimental result using an FPAA for fourth order Type II asymmetric-slope band-pass filter in (5.24) with  $\alpha = 0.5$ ,  $Q = 42$ .

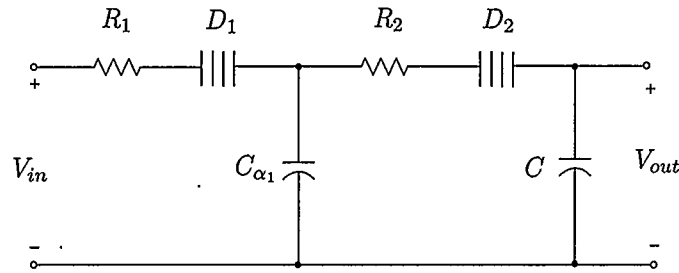


**Figure 5.31:** Passive prototype model of fourth order Type II FDNR-based asymmetric band-pass filter using one fractional capacitor.

where  $a = \frac{R_1 + R_2}{R_1 R_2 C_{\alpha_1}}$ ,  $b = \frac{1}{R_2 C}$ ,  $c = \frac{1}{R_1 R_2 C C_{\alpha_1}}$ ,  $d = \frac{R_1 D_1 + R_2 D_2}{R_1 R_2 D_1 D_2}$ ,  $e = \frac{D_1 + D_2}{R_1 R_2 D_1 D_2 C_{\alpha_1}}$ ,  $f = \frac{1}{R_1 R_2 D_1 C}$  and  $g = \frac{1}{R_1 R_2 D_1 D_2}$ . The transfer function in (5.26) can be obtained from the fourth order Type II transfer function in (5.23) if  $\alpha$  is replaced by  $1 - \alpha$ . We have the following transfer function for the fourth order passive prototype model in Figure 5.31 if  $C$  is replaced by another fractional order capacitor ( $C_{\alpha_2}$ ) with the same fractal order

$$H_{IV}^{\hat{}}(s) = \frac{cs^{2-2\alpha}}{s^4 + as^{4-\alpha} + bs^{4-2\alpha} + cs^2 + ds^{2-\alpha} + e} \quad (5.27)$$

where the parameters are  $a = \frac{(R_1 C_{\alpha_1} + R_1 C_{\alpha_2} + R_2 C_{\alpha_2})}{R_1 R_2 C_{\alpha_1} C_{\alpha_2}}$ ,  $b = \frac{1}{R_1 R_2 C_{\alpha_1} C_{\alpha_2}}$ ,  $c = \frac{R_1 D_1 + R_2 D_2}{R_1 R_2 D_1 D_2}$ ,  $d = \frac{(D_1 C_{\alpha_2} + D_2 C_{\alpha_1} + D_2 C_{\alpha_2})}{R_1 R_2 D_1 D_2 C_{\alpha_1} C_{\alpha_2}}$  and  $e = \frac{1}{R_1 R_2 D_1 D_2}$ . Clearly the fourth order Type II transfer

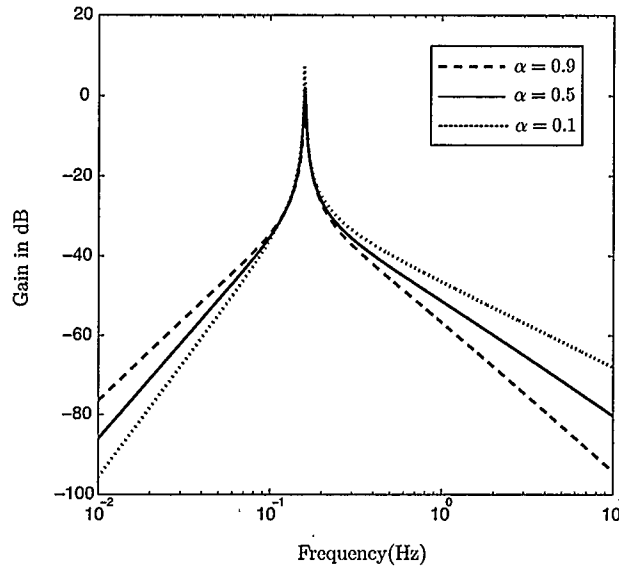


**Figure 5.32:** Magnitude response of the proposed fourth-order Type II filter in (5.26) to various values of  $\alpha$ .

function in (5.27) can be obtained from the transfer function in (5.24) if  $\alpha$  is replaced by  $1 - \alpha$ . Figure 5.32 shows the magnitude response of the filter in (5.26) at  $a = e = 0.5$ ,  $b = d = f = 2$ ,  $c = 0.05$  and  $g = 1$ . The step response of the filter can be obtained by replacing the non-integer Laplacian operator  $s^\alpha$  in transfer functions in (5.26) and (5.27) with the equation (3.1). It is to be noted that the step response of the fourth order Type II inductor-based filters in (5.23) and (5.24) can be used for the fourth order Type II FDNR-based filter if for the identical  $a, b, c, d, e, f$  and  $g$ ,  $\alpha$  is replaced by  $1 - \alpha$ . Therefore, Figure 5.24 shows the step response of fourth order filter in (5.27) at  $a = b = d = 2$ ,  $c = e = 1$  and  $\alpha = 0.5$ .

#### 5.3.4.2 Simulation and Experimental Results

The fourth order Type II realization using floating FDNR whose input impedance is  $Z_i = C_1 C_2 R_1 R_2 / (R_3 s^2)$  and one fractional-order capacitor  $C_{\alpha_1}$  is shown in Figure 5.33. The circuit was first simulated using AD844 opamps biased with  $\pm 15V$  supplies in SPICE as shown in Figure 5.34. The fractional-order capacitor  $C_{\alpha_1}$  having

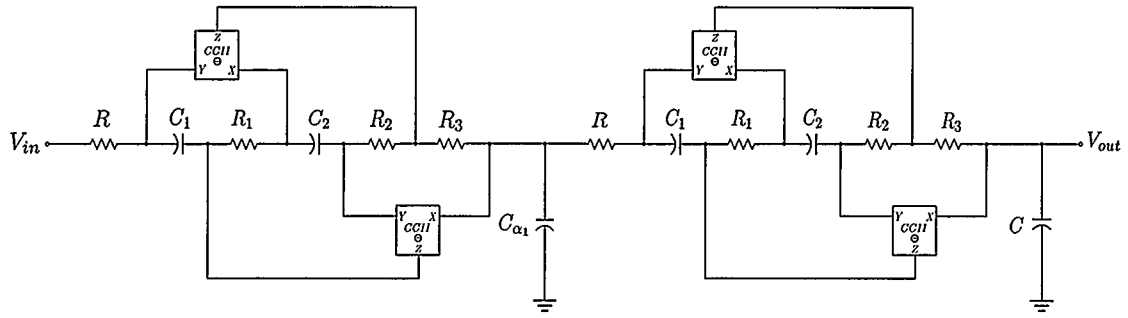


**Figure 5.33:** Possible realization of fourth-order Type II FDNR-based asymmetric-slope band-pass filter.

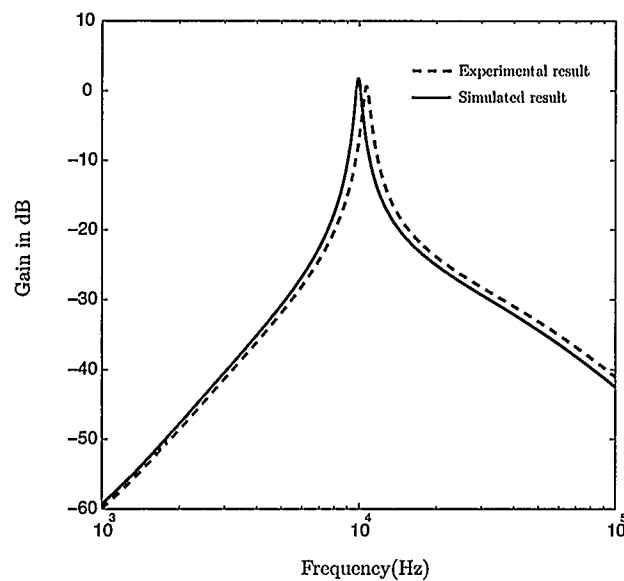


**Figure 5.34:** SPICE and experimental results of the filter in Figure 5.33.

$C = 3.7\mu F$  and  $\alpha_1 = 0.5$  was approximated by Carlson's method such that it has an operating range of  $1kHz - 100kHz$ . The value of components is shown in Table 3.2.

The comparison between simulation and experimental results for the fourth-order Type II FDNR-based asymmetric-slope band-pass filter of Figure 5.33 using  $R = 8k\Omega$ ,  $R_1 = 14k\Omega$ ,  $R_2 = 8.2k\Omega$ ,  $R_3 = 38k\Omega$ ,  $C_1 = 4.7nF$ ,  $C_2 = 2.2nF$  and  $C = 1nF$  is also shown in Figure 5.34. The expected quality factor and center frequency were  $Q = 20$  and  $f_o = 10kHz$ . The slope at frequencies lower than  $f_o$  was measured as  $50 dB/dec$  while it was measured as  $-30 dB/dec$  at frequencies greater than  $f_o$ .

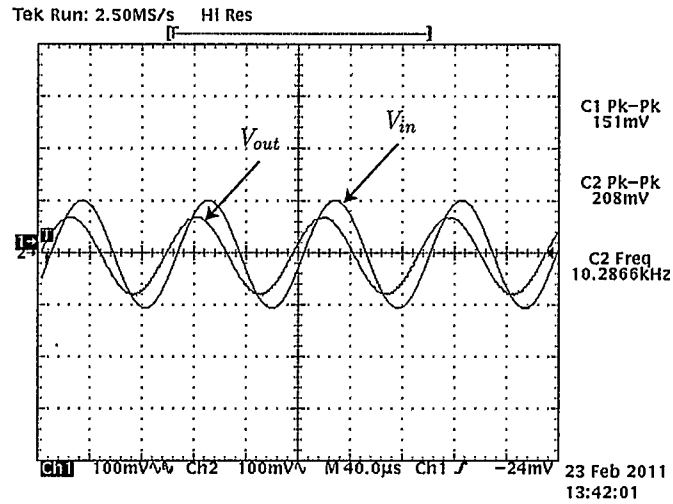


**Figure 5.35:** Measured transient response of the fourth order Type II FDNR-based asymmetric-slope band-pass filter in Figure 5.33 confirming stability at  $\alpha = 0.5$ .

confirming the asymmetric nature of the band-pass filter. The measured  $(Q, f_o)$  for the circuit were  $(16.95, 10.6kHz)$ , respectively. To confirm stability, the steady state transient response of the filter in Figure 5.33 is shown in Figure 5.35.

## CHAPTER 6

### Conclusions and future work

#### 6.1 Conclusion

In this work, new approaches were proposed for realizing high- $Q$  continuous-time asymmetrical-slope band-pass filters based on concepts of fractional-order filters [15], [16], [18]. Two types of asymmetric-slope band-pass filters were presented and the symmetry in the relationship of one transfer function to the next was highlighted. Exact expressions for  $\omega_o$  and approximate expressions for the  $Q$  of two types of second-order filters were presented. The two approaches were verified experimentally using discrete components and an FPAA technique. For the discrete realizations, the overhead of using an emulation of the fractional capacitor is still acceptable given the complexity of other techniques. The overhead of the FPAA technique, as clear from (3.2) and (3.3), is that a fourth-order transfer function is realized instead of the actual second-order functions in (1.5), (1.6), (1.7) and (1.8); due to employing the fractional Laplacian operator. The non-ideal effects of second-order asymmetric-slope band-pass filters were studied as well. The effects of parasitic capacitors in the non-ideal FDNR and resistor in non-ideal inductor were considered and four non-ideal transfer functions were introduced for each Type of second-order filters. Furthermore, the effects of current and voltage tracking errors in non-ideal current conveyors and the finite gain-band width product in operational amplifiers were considered for second-order filters and the amplitude response of the non-ideal transfer functions were compared to the ideal response curves.

The techniques used in the second-order filters were then extended to higher-order filters as well.  $m^{th}$  order band-pass filters with two different slopes in the stopband were introduced for proof of the concept. Two types of fourth-order asymmetric-slope band-pass filter were proposed, simulated in SPICE and verified experimentally using discrete components and FPAA technique. Using the FPAA technique two eighth order transfer functions were realized after substituting the Laplacian operator  $s^\alpha$  with the second order approximation in equations (5.19) and (5.24).

## 6.2 Contribution

The main contributions of this thesis have been divided into two areas. First in the design of second-order asymmetric-slope band-pass filters which can obtain very large quality factors and secondly extending the same techniques to design higher order asymmetric-slope band-pass filters.

This work introduced methods by which asymmetric band-pass filters can be realized, based on fractional-order transfer functions. All available techniques that have been proposed up until now for the design of such filters were microwave-based techniques (see [20, 21]) that have only been verified using micro-strip based circuits. In this work we not only introduce a new theory for the design of asymmetric filters but verify its functionality using classical discrete circuit topologies as well as by using an FPAA. The use of standard inductor, FDNR and MAB filter structures, which are classical and widely known structures, serves to show that the proposed fractional-order transfer functions can still rely on available classical techniques of filter circuit design. Compared to other design techniques for asymmetric filter design, this overhead is less and the design process is easier.

Coupled with obtaining asymmetrical characteristics, we also show that the proposed technique can achieve high-Q filters, which by itself is a challenging problem. Hence, the advantage of using fractional-order transfer functions in achieving together

two properties, which are otherwise very difficult to achieve, is clear. To obtain high quality factor we used fractional capacitors which yields fractional terms in the transfer function of the filters. The non-integer Laplacian operator in the denominator of the transfer function of band-pass filters played the main role in placing the poles very close to the stability boundary and obtaining high quality factors whereas the operator in the numerator was considered to obtain asymmetric-slope characteristics.

### 6.3 Future Work

This work has focused on the importing of concepts from fractional calculus into the design of filters to create asymmetric-slope fractional-order filters with high quality factors. Although no commercial fractional capacitors are available as yet, the research on fractals in [8, 11, 12, 46, 47] appears promising and lends itself to this work. Furthermore, even though low frequencies were used in the experiments, with the advent of commercial or in-house fractional capacitors it is conceivable that this work could be naturally extended to higher frequencies. Further research would have to be done to investigate the behavior of these circuits at higher frequencies and beyond the operational range of the fractional capacitances. Likewise the sharp and different phase responses for frequencies greater than or less than  $\omega_o$  for both types of circuits, suggest that these circuits may find other applications or uses in phase discriminators. The nature of the networks in Figures 5.4 and 5.6 suggest that these principles could potentially be expanded to the Butterworth, Chebychev, Inverse Chebychev and Elliptic filter approximations. In addition, further research could be done to generate and design asymmetric notch filters.

The entirety of this work focused on the continuous time second-order band-pass filters with asymmetric-slope characteristics and high quality factors. The design equations and process to create second-order band-pass filters were presented for two types of filters. The concept was expanded to higher order filters, however the

closed-loop expressions for center frequency and quality factor are unexplored. The concept was proved by giving simulation and experimental results for Type I and Type II fourth order filters in Chapter 5. Further work could be done to determine the generalized method to design higher order asymmetric-slope band-pass filters and find expressions for center frequency and quality factor.

Finally, further work could be done on designing and implementing high quality factor symmetric band-pass filters using fractional capacitor showing the potential to become commercially available.

## BIBLIOGRAPHY

- [1] R. Schaumann and M. V. Valkenburg, "Design of analog filters," *Oxford University Press, 1st ed*, 2001. 1, 2, 29, 30
- [2] A. Sedra and P. Brackett, *Filter Theory and Design: Active and Passive*. Matrix Publishers, 1978. 1, 2, 29, 30, 84
- [3] R. Raut and M. N. S. Swamy, *Modern Analog Filter Analysis and Design*. Wiley-VCH, 2010. 1, 2
- [4] L. D. Paarmann, *Design and Analysis of Analog Filters*. Springer, 2001. 1, 2
- [5] B. Mayer and M. Vogel, "Design Chebychev bandpass filters efficiently," *R.F. Des. (USA)*, vol. 25, no. 9, pp. 50 – 56, September 2002. 2
- [6] T. Deliyannis, Y. Sun, and J. Fidler, *Continuous-Time Active Filter Design*. CRC Press, 1999. 2, 29, 84
- [7] G. Carlson and C. Halijak, "Approximation of fractional capacitors  $(\frac{1}{s})^{\frac{1}{n}}$  by regular Newton process," *IEEE – Transactions on Circuit Theory*, vol. CT-11, no. 2, pp. 210 – 213, 1964. 4, 6, 36, 42, 84, 94, 121
- [8] I. S. Jesus, J. A. T. Machado, and M. F. Silva, "Fractional order capacitors," *Proceedings of the IASTED International Conference on Modelling, Identification, and Control, MIC*, 2008. 4, 104

- [9] A. Elwakil, "Fractional-order circuits and systems: An emerging interdisciplinary research area," *IEEE Circuits Syst. Mag. (USA)*, vol. 10, no. 4, pp. 40 – 50, Fourth Quarter 2010. 4
- [10] K. Biswas, S. Sen, and P. Dutta, "Modeling of a capacitive probe in a polarizable medium," *Sens. Actuators A, Phys. (Switzerland)*, vol. 120, no. 1, pp. 115 – 22, 2005/04/29. 4
- [11] T. Haba, G. Loum, J. Zoueu, and G. Ablart, "Use of a component with fractional impedance in the realization of an analogical regulator of order  $1/2$ ," *J. Applied Sciences*, vol. 8, no. 1, pp. 59 – 67, Jan. 2008. 4, 5, 104
- [12] T. Haba, G. Ablart, and T. Camps, "The frequency response of a fractal photolithographic structure," *IEEE Trans. Dielectr. Electr. Insul.*, vol. 4, no. 3, pp. 321 – 6, June 1997. 4, 5, 104
- [13] J. Tenreiro Machado, "Fractional derivatives: probability interpretation and frequency response of rational approximations," *Commun. Nonlinear Sci. Numer. Simul. (Netherlands)*, vol. 14, no. 9-10, pp. 3492 – 7, Sept.-Oct. 2009. 6
- [14] J. T. Machado, V. Kiryakova, and F. Mainardi, "Recent history of fractional calculus," *Communications in Nonlinear Science and Numerical Simulation*, vol. 16, no. 3, pp. 1140 – 1153, 2011. 6
- [15] A. Radwan, A. Soliman, and A. Elwakil, "First-order filters generalized to the fractional domain," *Journal of Circuits, Systems and Computers*, vol. 17, no. 1, pp. 55 – 66, 2008. [Online]. Available: <http://dx.doi.org/10.1142/S0218126608004162> 6, 9, 102
- [16] A. Radwan, A. Elwakil, and A. Soliman, "On the generalization of second-order filters to the fractional-order domain," *J. Circuits Syst. Comput.*

- (*Singapore*), vol. 18, no. 2, pp. 361 – 386, 2009. [Online]. Available: <http://dx.doi.org/10.1142/S0218126609005125> 6, 9, 102
- [17] T. Freeborn, B. Maundy, and A. Elwakil, “Towards the realization of fractional step filters,” in *International Symposium on Circuits and Systems (ISCAS)*, May 2010, pp. 1037–1040. 6, 45
- [18] B. Maundy, A. Elwakil, and T. Freeborn, “On the practical realization of higher-order filters with fractional stepping,” *Signal Processing*, vol. 91, pp. 484 – 491, 2011. [Online]. Available: <http://dx.doi.org/10.1016/j.sigpro.2010.06.018> 6, 102
- [19] A. M. A. Hudrouss, A. Jayyousi, and M. Lancaster, “An asymmetric dual-band hts band-pass filter for american mobile phone system,” *PIERS 2010 Cambridge - Progress in Electromagnetics Research Symposium, Proceedings*, pp. 183 – 186, 2010. 7, 8
- [20] J.-S. Hong and M. Lancaster, “Microstrip cross-coupled trisection bandpass filters with asymmetric frequency characteristics,” *IEE Proceedings: Microwaves, Antennas and Propagation*, vol. 146, no. 1, pp. 84 – 90, 1999. [Online]. Available: <http://dx.doi.org/10.1049/ip-map:19990146> 7, 8, 103
- [21] P. Field, I. Hunter, and J. Gardiner, “Asymmetric bandpass filter using a novel microstrip circuit,” *IEEE Microw. Guid. Wave Lett. (USA)*, vol. 2, no. 6, pp. 247 – 9, 1992. [Online]. Available: <http://dx.doi.org/10.1109/75.136521> 7, 8, 103
- [22] ———, “Asymmetric bandpass filter using a ceramic structure,” *IEEE Microwave and Guided Wave Letters*, vol. 2, no. 9, pp. 361 – 363, 1992. [Online]. Available: <http://dx.doi.org/10.1109/75.153620> 8

- [23] T. Freeborn, B. Maundy, and A. Elwakil, "FPAA implementation of fractional step filters," *IET Circuits Devices and Systems*, vol. 4, pp. 514–524, November 2010. 9
- [24] L. Bruton, "Network transfer functions using concept of frequency-dependent negative resistance," *IEEE Transactions on Circuit Theory*, vol. CT-16, no. 3, pp. 406 – 408, 1969. 12, 15, 30, 74
- [25] A. Radwan, A. Soliman, A. Elwakil, and A. Sedeek, "On the stability of linear systems with fractional-order elements," *Chaos, Solitons and Fractals*, vol. 40, no. 5, pp. 2317 – 2328, 2009. [Online]. Available: <http://dx.doi.org/10.1016/j.chaos.2007.10.033> 16
- [26] R. Senani, "Generation of new two-amplifier synthetic floating inductors," *Electron. Lett. (UK)*, vol. 23, no. 22, pp. 1202 – 3, 1987. 29
- [27] L. Bruton and A. Haase, "High-frequency limitations of re-active filters containing simulated-l and fdnr elements," *Int. J. Circuit Theory Appl. (UK)*, vol. 2, no. 2, pp. 187 – 94, 1974. 29
- [28] W.-S. Chung, H.-J. Kim, and K.-M. Cho, "Current-controllable fdnrs using linear transcapacitance amplifiers," *International Journal of Electronics*, vol. 91, no. 7, pp. 421 – 430, 2004. [Online]. Available: <http://dx.doi.org/10.1080/00207210412331294586> 29
- [29] S. Minaei, E. Yuce, O. Cicekoglu, and S. Ozcan, "Inductance and FDNR simulator employing only two CCII+s," *Applied Electronics*, pp. 227 – 231, September 2005. 29, 84
- [30] M. Cicekoglu, "Active simulation of grounded inductors with CCII+s and grounded passive elements," *International Journal of Electronics*, vol. 85,

- no. 4, pp. 455 – 462, 1998. [Online]. Available: <http://dx.doi.org/10.1080/002072198134003> 29, 84
- [31] S. Ben Salem, M. Fakhfakh, D. S. Masmoudi, M. Loulou, P. Loumeau, and N. Masmoudi, “A high performances cmos ccii and high frequency applications,” *Analog Integrated Circuits and Signal Processing*, vol. 49, no. 1, pp. 71 – 78, 2006. [Online]. Available: <http://dx.doi.org/10.1007/s10470-006-8694-4> 29
- [32] A. Ismail and M. Soliman, “Novel cmos current conveyor realizations suitable for high-frequency applications,” *Microelectron. J. (UK)*, vol. 30, no. 12, pp. 1231 – 9, 1999. [Online]. Available: [http://dx.doi.org/10.1016/S0026-2692\(99\)00047-6](http://dx.doi.org/10.1016/S0026-2692(99)00047-6) 29
- [33] M. Siddiqi and M. Ahmed, “Realization and performance assessment of active-R inductors,” *International Journal of Electronics*, vol. 70, no. 4, pp. 713 – 728, April 1991. 29, 84
- [34] M. Soderstrand, “Active r ladders: high-frequency high-order low-sensitivity active r filters without external capacitors,” *IEEE Trans. Circuits Syst. (USA)*, vol. CAS-25, no. 12, pp. 1032 – 8, 1978. 29
- [35] B. Maundy, S. Gift, and P. Aronhime, “A novel hybrid active inductor,” *IEEE Transactions on Circuits and Systems II: Express Briefs*, vol. 54, no. 8, pp. 663 – 667, 2007. [Online]. Available: <http://dx.doi.org/10.1109/TCSII.2007.898898> 29, 84
- [36] W. Gaiewski, L. Dunleavy, and L. Geis, “Hybrid inductor modeling for successful filter design,” *IEEE Trans. Microw. Theory Tech. (USA)*, vol. 42, no. 7, pp. 1426 – 9, 1994. [Online]. Available: <http://dx.doi.org/10.1109/22.299741> 29
- [37] L. Huelsman and P. Allen, *Introduction to the theory and design of active filters*. McGraw-Hill, 1980, USA. 30

- [38] L. P. Huelsman, *Active filters: lumped, distributed, integrated, digital and parametric*. McGraw Hill Company. 31, 89
- [39] U. Kumar, S. Shukla, and Amiete, "Analytical study of inductor simulation circuits," *Act. Passive Electron. Compon. (UK)*, vol. 13, no. 4, pp. 211 – 27, 1989. 31
- [40] A. M. Soliman and R. A. Saad, "Two new families of floating fdnr circuits," *Journal of Electrical and Computer Engineering*, vol. 2010. 33
- [41] M. Sugi, Y. Hirano, Y. F. Miura, and K. Saito, "Simulation of fractal immittance by analog circuits: An approach to the optimized circuits," *IEICE Transactions on Fundamentals of Electronics, Communications and Computer Sciences*, vol. E82-A, no. 8, pp. 1627 – 1635, 1999. 36
- [42] I. Podlubny, I. Petras, B. Vinagre, P. O'Leary, and L. Dorcak, "Analogue realizations of fractional-order controllers," *Nonlinear Dynamics*, vol. 29, pp. 281–296, 2002. 36
- [43] A. Djouambi, A. Charef, and A. Besancon, "Optimal approximation, simulation and analog realization of the fundamental fractional order transfer function," *Int. J. Appl. Math. Comput. Sci.*, vol. 17, no. 4, pp. 455–462, 2007. 36
- [44] B. Krishna and K. Reddy, "Active and passive realization of fractance device of order  $1/2$ ," *Active and Passive Electronic Components*, vol. 2008, no. 369421, p. 5 pages, 2008. [Online]. Available: <http://dx.doi.org/10.1155/2008/369421> 36
- [45] Anadigm, *Third generation dynamically re-configurable DPASP*, rev 1.1 ed., AN231E04 Datasheet, 2007. 44, 86, 95
- [46] G. Ablart, T. Haba, and G. Loum, "An analytical expression for the input impedance of a fractal tree obtained by a microelectronic process and exper-

- imental measurements of its non-integral dimension,” *Chaos Solitons Fractals (UK)*, vol. 33, no. 2, pp. 364 – 73, July 2007. 104
- [47] T. Haba, G. Ablart, T. Camps, and F. Olivie, “Influence of the electrical parameters on the input impedance of a fractal structure realised on silicon,” *Chaos Solitons Fractals (UK)*, vol. 24, no. 2, pp. 479 – 90, April 2005. 104
- [48] B. Maundy and S. Gift, “Active grounded inductor circuit,” *International Journal of Electronics*, In Press. 121

## APPENDIX A

### Approximated Fractional Capacitor Realization

An approximated fractional capacitor must be built to simulate the proposed asymmetric-slope band-pass filters. Carlson's method was used to simulate the fractional capacitor whose impedance is  $Z_{c_\alpha} = \frac{1}{C_\alpha(j\omega)^\alpha}$ , where  $C_\alpha$  is the value of capacitor and  $0 < \alpha < 1$ . It is possible to approximate the term  $(1/s)^n$  for  $n = \frac{1}{\alpha} > 1$  using this method.

The following function is used in the newton process for this approximation

$$F(x) = x \frac{(n-1)x^n + (n+1)(1/s)}{(n+1)x^n + (n-1)(1/s)} \quad (\text{A.1})$$

where  $x$  is the previous iteration. It is clear from A.1 that the order and accuracy of the approximation increases as the number of iteration increases.

The first iteration approximation of  $(1/s)^\alpha$  using an initial assumption  $x_o = 1$  yields

$$1/s^\alpha \approx \frac{(\alpha^2 + 3\alpha + 2)s^2 + (8 - 2\alpha^2)s + (\alpha^2 - 3\alpha + 2)}{(\alpha^2 - 3\alpha + 2)s^2 + (8 - 2\alpha^2)s + (\alpha^2 + 3\alpha + 2)} \quad (\text{A.2})$$

and the second iterate approximation is given by

$$1/s^\alpha \approx \frac{as^4 + bs^3 + cs^2 + ds + e}{es^4 + ds^3 + cs^2 + bs + a} \quad (\text{A.3})$$

where  $a = \alpha^4 - 10\alpha^3 + 35\alpha^2 - 50\alpha + 24$ ,  $b = -4\alpha^4 + 20\alpha^3 + 40\alpha^2 - 320\alpha + 384$ ,  $c = 6\alpha^4 - 150\alpha^2 + 864$ ,  $d = -4\alpha^4 - 20\alpha^3 + 40\alpha^2 + 320\alpha + 384$  and  $e = \alpha^4 + 10\alpha^3 + 35\alpha^2 + 50\alpha + 24$ . It is to be noted that equations in (A.2) and (A.3) approximate the

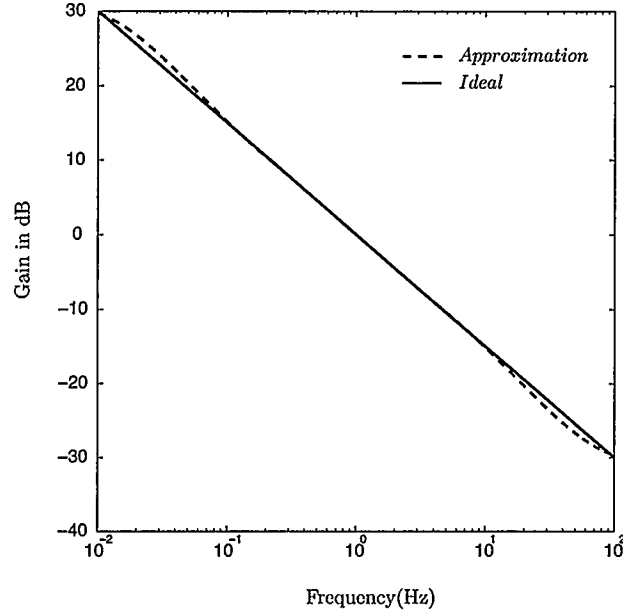


**Figure A.1:** Comparison between magnitude responses of the approximated fractional capacitor and ideal fractional capacitor at  $C = 1\mu F$  and  $\alpha = 0.75$ .

fractional order capacitor around the frequency  $1rad/s$ . As an example the following Carlson's approximation can be used for second iteration of  $1/s^{0.75}$ .

$$1/s^{0.75} \approx \frac{39s^4 + 2964s^3 + 13338s^2 + 10868s + 1463}{1463s^4 + 10868s^3 + 13338s^2 + 2964s + 39} \quad (\text{A.4})$$

the comparison between the magnitude responses of this approximation and ideal fractional capacitor of impedance  $Z_c(s) = \frac{1}{s^{0.75}}$  is shown in Figure A.1. Using the approximation in (A.3) the fractional capacitor can be realized using the RC ladder network in Figure A.2 whose input impedance is

$$Z_{in} = R_{in} + \frac{1}{C_1(s + R_1C_1)} + \frac{1}{C_2(s + R_2C_2)} + \frac{1}{C_3(s + R_3C_3)} + \frac{1}{C_4(s + R_4C_4)} \quad (\text{A.5})$$

The values of components can be found by equating equations in (A.3) and (A.5).

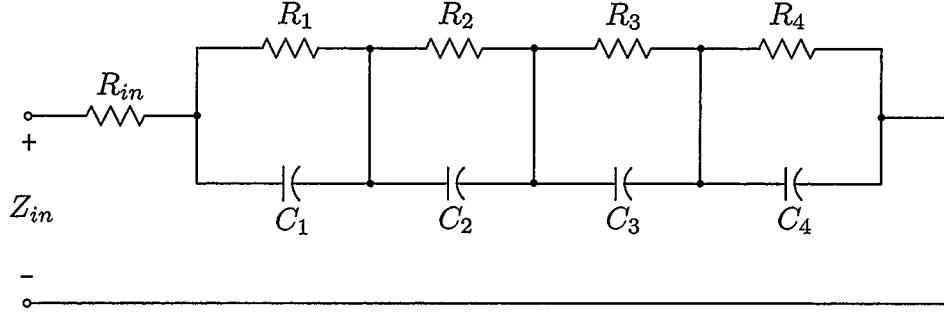


**Figure A.2:** RC tree to realize fourth order approximated fractional Laplacian operator based on Carlson's approximation technique.

As an example the equation in (A.4) can be rewritten in the form

$$1/s^{0.75} = 0.026 + \frac{0.332}{s + 1.192} + \frac{0.505}{s + 0.014} + \frac{0.28}{s + 0.267} + \frac{0.709}{s + 5.954} \quad (\text{A.6})$$

and the values of components are  $R_{in} = 0.026\Omega$ ,  $R_1 = 0.119\Omega$ ,  $R_2 = 0.278\Omega$ ,  $R_3 = 1.046\Omega$ ,  $R_4 = 36.041\Omega$ ,  $C_1 = 1.408F$ ,  $C_2 = 3.01F$ ,  $C_3 = 3.57F$  and  $C_4 = 1.977F$ .

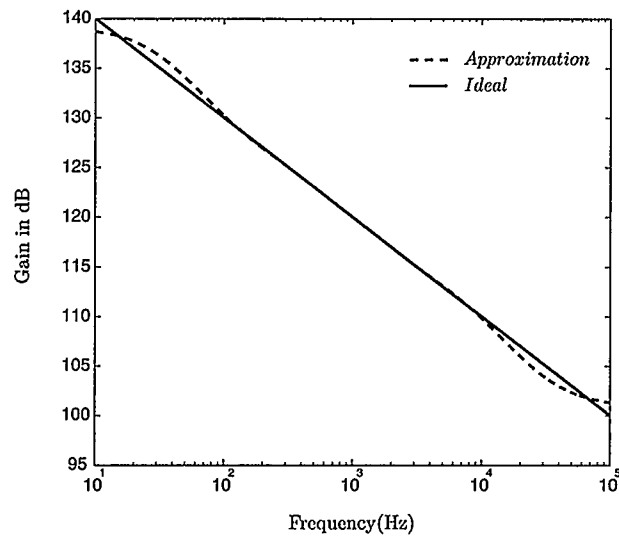
It is worth noting that the fractional capacitor with the capacitance of  $C_\alpha$  can be approximated around any frequency,  $\omega_c$ , by applying magnitude and frequency scaling factors to the values of  $R$  and  $C$  in the RC ladder network. The values of components after scaling are

$$\hat{R} = Rk_m \quad (\text{A.7})$$

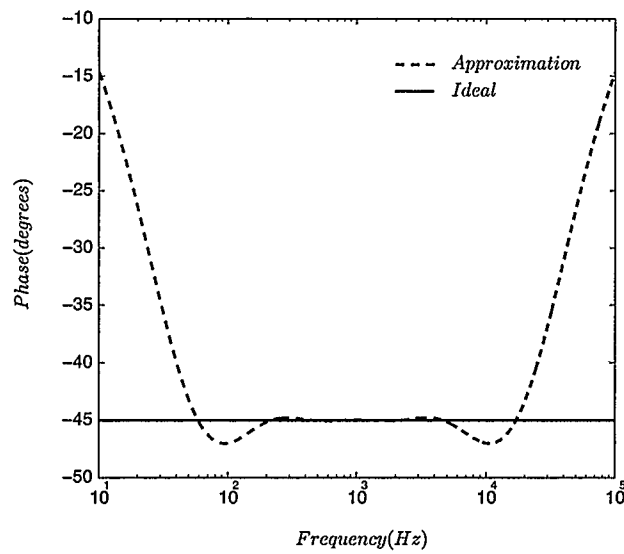
$$\hat{C} = C/K_mk_f \quad (\text{A.8})$$

where  $k_m = 1/(C_\alpha\omega_c^\alpha)$  is the magnitude scaling factor and  $k_f = \omega_c$  is frequency scaling factor. Figure A.3 and A.4 show the magnitude and phase responses of the approximated fractional capacitors used in this work compared to the ideal fractional capacitors.

Figure A.5 shows the code used to generate the values of components for fractional capacitor  $C_\alpha$  having  $C = 1\mu F$  and  $\alpha = 0.5$  with the center frequency of  $f_o = 1kHz$ .



(a)



(b)

**Figure A.3:** Comparison between the magnitude and phase responses of the approximated and ideal fractional capacitors with the impedance of

$$Z_{c_\alpha}(j\omega) = \frac{1}{1\mu F(j\omega)^{0.5}} \text{ centered around } 1kHz.$$

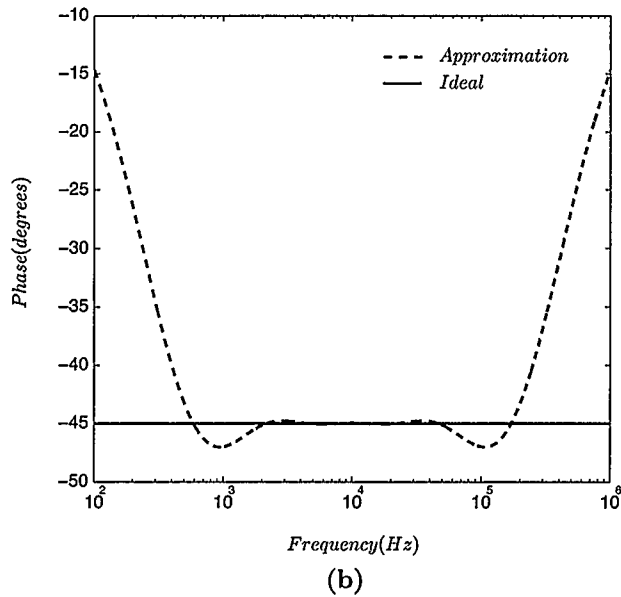
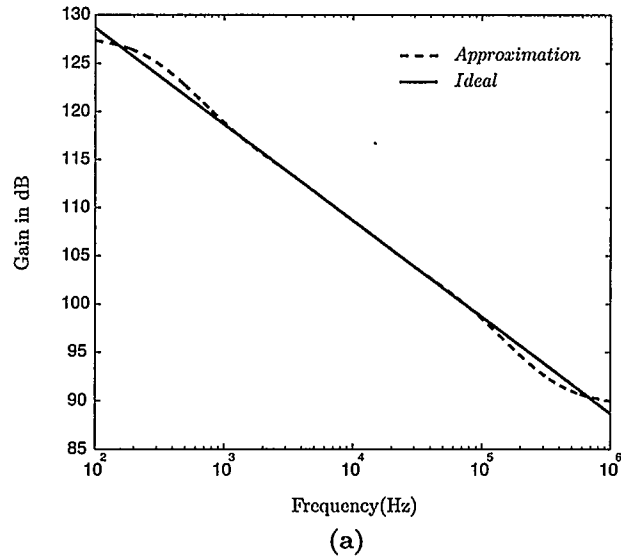


**Figure A.4:** Comparison between the magnitude and phase responses of the approximated and ideal fractional capacitors with the impedance of

$$Z_{c_\alpha}(j\omega) = \frac{1}{3.7\mu F(j\omega)^{0.5}} \text{ centered around } 10k Hz.$$

```

[This program generates any series RC tree for any value of alpha, center frequency and capacitance C
> restart;
with(numtheory):
wo:=evalf(2*Pi*(1e3)): This is the desired center frequency
alpha:=0.5: This is the desired value of alpha
C:=1e-6: These values represent the desired Capacitance and the center frequency wo of the approximation

> kf:=wo: This is the desired frequency scaling factor
> km:=1/C/(wo^0.5): This is the desired magnitude scaling factor
> n:=8: Expand to the order of s^4
> out1:=cfrac((1+x)^beta, x, n, 'simple'):
> x:=s-1:
> sa_h:=cfrac(out1):
> total:=sa_h:
total:=normal(total,expanded):
total:=sort(total,s,descending):
s_alpha:=collect(total,s):

> beta:=-alpha: Flip the value of the function needed.
s_alpha:=normal(s_alpha):
> s_alpha:=simplify(%);
          s_alpha := 
$$\frac{39. s^4 + 2964. s^3 + 13338. s^2 + 10868. s + 1463.}{1463. s^4 + 10868. s^3 + 13338. s^2 + 2964. s + 39.}$$


> num:=numer(s_alpha):num:=collect(num,s):
a:=coeff(num,s,3)/coeff(num,s,4);
b:=coeff(num,s,2)/coeff(num,s,4);
c:=coeff(num,s,1)/coeff(num,s,4);
d:=coeff(num,s,0)/coeff(num,s,4);
          a := 76.00000000
          b := 342.00000000
          c := 278.66666667
          d := 37.51282051

>
> y:=Rin + (1/C1)/(s + 1/R1/C1) + (1/C2)/(s + 1/R2/C2) + (1/C3)/(s +
1/R3/C3) + (1/C4)/(s + 1/R4/C4);This is the input impedance of RC network

```

```

y := Rin +  $\frac{1}{C1 \left( s + \frac{1}{R1 \ C1} \right)}$  +  $\frac{1}{C2 \left( s + \frac{1}{R2 \ C2} \right)}$  +  $\frac{1}{C3 \left( s + \frac{1}{R3 \ C3} \right)}$  +  $\frac{1}{C4 \left( s + \frac{1}{R4 \ C4} \right)}$ 
>
> test:=(s^4 + a*s^3 + b*s^2 + c*s + d)/(d*s^4 + c*s^3 + b*s^2 + a*s + 1);
I use this to check that the partial fraction expansion matches the unscaled R's and C's
test :=  $\frac{s^4 + 76.00000000 s^3 + 342.0000000 s^2 + 278.6666667 s + 37.51282051}{37.51282051 s^4 + 278.6666667 s^3 + 342.0000000 s^2 + 76.00000000 s + 1}$ 
> out:=convert(test,parfrac,s,real);
out := 0.02665755298 +  $\frac{0.3322203021}{s + 1.192550328}$  +  $\frac{0.5058089777}{s + 0.01403407795}$  +  $\frac{0.2800354153}{s + 0.2674945446}$  +  $\frac{0.7098817949}{s + 5.954492479}$ 
> x:=fsolve(denom(test)=0,s);
x := -5.954492479, -1.192550328, -0.2674945446, -0.01403407795
> fg:=s->out;
fg := s -> out
> res1:=residue(fg(s),s=x[1]);
res2:=residue(fg(s),s=x[2]);
res3:=residue(fg(s),s=x[3]);
res4:=residue(fg(s),s=x[4]);
res1 := 0.7098817947
res2 := 0.3322203021
res3 := 0.2800354153
res4 := 0.5058089777
> Calculate the new scaled and shifted values of R's and C's
> Rin:=1/d;
C1:=1/res1;R1:=-res1/x[1];
C2:=1/res2;R2:=-res2/x[2];
C3:=1/res3;R3:=-res3/x[3];
C4:=1/res4;R4:=-res4/x[4];
Rin := 0.02665755298
C1 := 1.408685231
R1 := 0.1192178506
C2 := 3.010050842
R2 := 0.2785796912
C3 := 3.570976903
R3 := 1.046882716
C4 := 1.977030943

```



## APPENDIX B

### Alternative Second-order Type II Inductor-based Circuit

In this section we present an alternative second-order Type II inductor-based filter supported by simulation and experimental results. A second order Type II inductor-based asymmetric-slope band-pass filter using a grounded inductor, whose impedance is  $Z_i = RR_1C_1s$  (see Figure B.1(a)) is shown in Figure B.1(b) [48]. The circuit realizes (1.7) with  $k_3 = 1$ ,  $a = C_\alpha/C_1$  and  $b = 1/(RR_1CC_1)$ .

The proposed circuit was simulated in SPICE using LT1364 opamps (rated bandwidth 70MHz) biased with  $\pm 15V$  supplies. Carlson's method [7] was used to simulate the fractional-order capacitor  $C_\alpha$  having  $C = 1\mu F$  and  $\alpha = 0.5$ , as shown in Figure 3.1. The values of the capacitors and resistors in the approximated model shown in Table 3.1 were calculated such that  $C_\alpha$  has an operating range of  $100Hz-10kHz$ .

The comparison between simulation and experimental results for the proposed filter taking  $R = R_1 = 1.59k\Omega$ ,  $C = 0.1\mu F$  and  $C_1 = 0.215\mu F$  is shown in Figure B.2. The filter was designed to achieve a quality factor of 25 and a center frequency of  $f_o = 1kHz$ . The measured  $(Q, f_o)$  were respectively  $(23.956, 1.0213kHz)$ . Also the measured slope at frequencies lower than  $f_o$  was  $30 dB/dec$  while it was  $-10 dB/dec$  at frequencies greater than  $f_o$  as expected from Table 2.2.

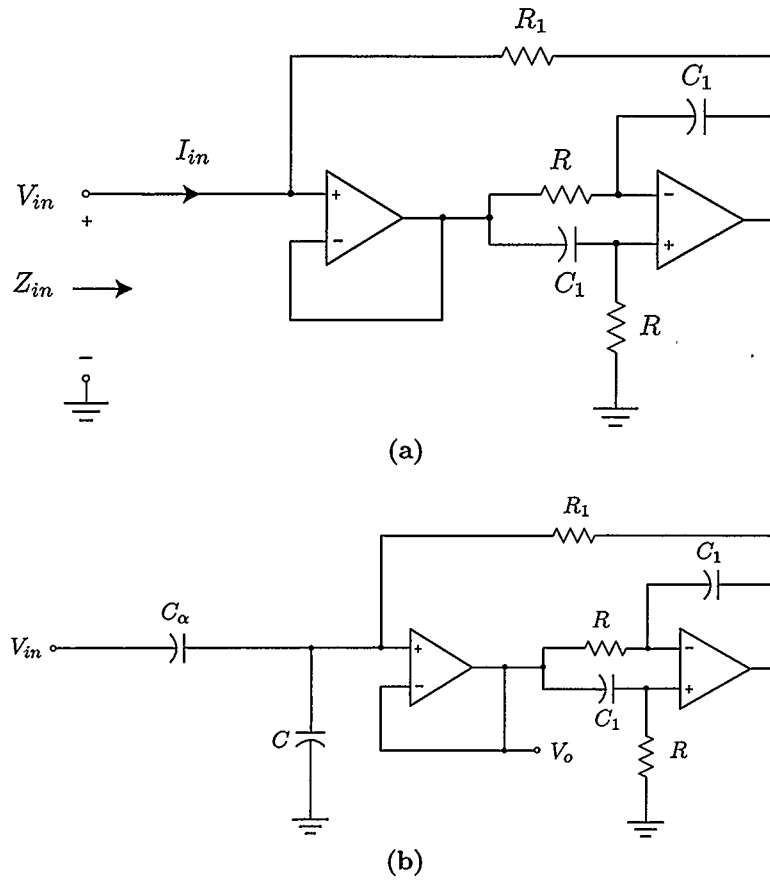


**Figure B.1:** Grounded inductor whose input impedance is  $Z_{in} = RR_1C_1s$  used in second order Type II inductor-based asymmetric-slope band-pass filter and (b) Possible realization of the Type II asymmetric-slope band-pass filter realizing (1.7).

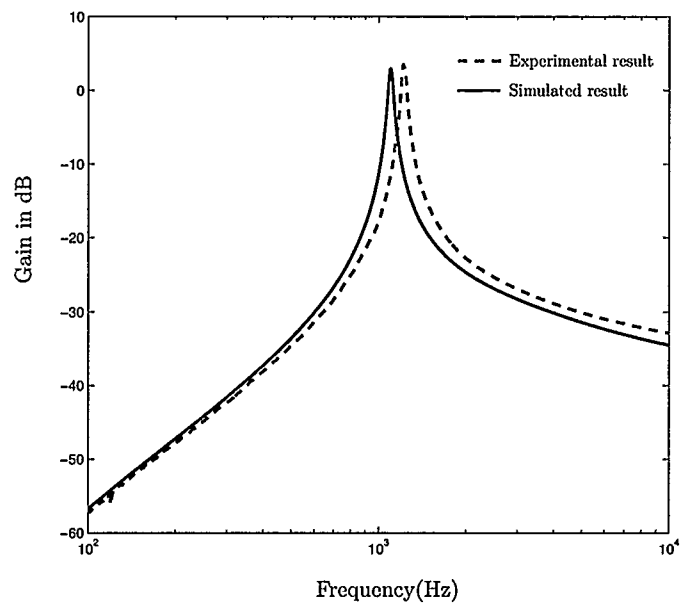


**Figure B.2:** SPICE and experimental results of the filter in Figure B.1(b).

## APPENDIX C

### Percentage Variability of Center Frequency and Quality Factor for Type I FDNR-Based Filter

The Matlab codes to generate Figures 4.11(a) and 4.11(b) for the Type I FDNR-based circuit are provided below. These codes were used to find the percentage variability of  $\Delta\omega_o/\omega_o$  and  $\Delta Q/Q$  versus  $\alpha$  and  $a$  for  $b = 1$  and  $\omega_t = 1000\omega_o$ .

```

close all;clear all;clc;
points=6001;
b=1;
N=10;
alpha_a=(linspace(0.05,N,N))/N;
aa=(linspace(0.05,N,N))/N;
for l=1:size(alpha_a,2)
for k=1:size(aa,2)
    a=aa(k);
    alpha=alpha_a(l);
% Solve for the exact wo according to equation (2.3) and (2.4) of the
thesis.
f = @(y)2*y + alpha*(y - log(b*exp(y) + a*exp(2*y)*cos(alpha*pi/2)));
zo = fzero(f,0.05);
wo = exp(zo/alpha); % Ideal wo based on a and b and the ideal equation.

wt=1000*wo; % opamp Gain Bandwidth Product. Typically much greater than wo

tau = 100/wt; % Experimental

w=logspace(-2,log10(wt),points);
s=j*w;
Hsn = 2*wt*a*tau*(s+s.^2*tau+wt)./(2*s.^(-alpha+3)*wt*tau+2*tau^2*s.^(-alpha+2)*wt*b+2*tau^2*s.^(-alpha+3)*b+2*tau^2*wt*a*s.^2+2*tau^2*s.^3*a+2*s.^(-alpha+4)*tau+2*s.^(-alpha+2)*b*tau+2*s.^(-alpha+3)+2*wt*a*tau*s.+s.^(-alpha)*wt^2*b*tau+2*a*tau*s.^2+wt^2*a*tau+s.^(-alpha+2)*wt^2*tau+2*s.^(-alpha+1)*wt*b*tau+2*s.^(-alpha+2)*wt);
Mag=20*log10(abs(Hsn));

% Find the frequency at which the maximum occurs in the Magnitude plot
[Y,Index]=max(Mag);
wo_new=w(Index); % Find the frequency at which we get the peak mag result
wo;
Percentage_change(l,k) = (wo_new - wo)*100/wo;

end
end

surf(alpha_a,aa,Percentage_change);
grid on
axis square
ylabel('a');
xlabel('\alpha');
zlabel('Percentage Change');
max(max(Percentage_change))
min(min(Percentage_change))

```

Figure C.1: The Matlab Code used to find the percentage variability of  $\Delta\omega_o/\omega_o$  shown in Figure 4.11(a).

```

close all;clear all;clc;
points=10001;
b=1;
N=10;
alpha_a=(linspace(0.05,N,N))/N;
aa=(linspace(0.05,N,N))/N;
for l=1:size(alpha_a,2)
for k=1:size(aa,2)
    a=aa(k);
    alpha=alpha_a(l);
    % Solve for the exact wo according to equation (2.3) and (2.4) of the
    % thesis.
    f = @(y)2*y + alpha*(y - log(b*exp(y) + a*exp(2*y)*cos(alpha*pi/2)));
    zo = fzero(f,0.05);
    wo = exp(zo/alpha); % Ideal wo based on a and b and the ideal equation.

    wt=1000*wo; % opamp Gain Bandwidth Product. Typically much greater than wo
    tau = 100/wt; % Experimental

    w=logspace(-2,log10(wt),points);
    s=j*w;
    Hsn = 2*wt*a*tau*(s+s.^2*tau+wt)./(2*s.^(-alpha+3)*wt*tau+2*tau^2*s.^(-k
alpha+2)*wt*b+2*tau^2*s.^(-alpha+3)*b+2*tau^2*wt*a*s.^2+2*tau^2*s.^3*a+2*s.^k
(-alpha+4)*tau+2*s.^(-alpha+2)*b*tau+2*s.^(-alpha+3)+2*wt*a*tau*s.^(-k
alpha)*wt^2*b*tau+2*a*tau*s.^2+wt^2*a*tau+s.^(-alpha+2)*wt^2*tau+2*s.^(-k
alpha+1)*wt*b*tau+2*s.^(-alpha+2)*wt);
    magdb=20*log10(abs(Hsn));
    [maxgaindb,Index]=max(magdb);
    wo_new=w(Index); % Find the frequency at which we get the peak mag result

    % This section finds the Q of the magnitude response for the nonideal TF
    w1 = spline(magdb(1:Index-1),w(1:Index-1),(maxgaindb-3.01));
    w2 = spline(magdb(Index+1:points),w(Index+1:points),(maxgaindb-3.01));
    w0_amp = pchip(magdb,w,(maxgaindb));
    Q_inter = w0_amp/abs(w1 - w2);

    % This sections looks at the ideal Transfer function and computes the Ideal
    % Q
    Hs=2*s.^alpha*a./(b+s.^alpha*a+s.^2);
    Magideal=20*log10(abs(Hs));
    [maxdb,Indx]=max(Magideal);
    w1Ideal = spline(Magideal(1:Indx-1),w(1:Indx-1),(maxdb-3.01));
    w2Ideal = spline(Magideal(Indx+1:points),w(Indx+1:points),(maxdb-3.01));

    Q_ideal = wo/abs(w1Ideal - w2Ideal);
    Percentage_Change(l,k) = (Q_inter - Q_ideal)*100/Q_ideal;

end
end
surf(alpha_a,aa,Percentage_Change)
grid on
axis square
ylabel('a');
xlabel('\alpha');
zlabel('Percentage Change');

```

Figure C.2: The Matlab Code used to find the percentage variability of  $\Delta Q/Q$  shown in Figure 4.11(b).

## APPENDIX D

### Non-ideal Transfer Function of Type I MAB-based Circuit

Examining the MAB based circuit of Figure 2.18(b), reveals that there are no complex zeroes in its non-ideal transfer function. The transfer function is of order  $s^6$  in the integer terms and  $s^{6+\alpha}$  in the fractal terms as shown in the Figure D.1.

```

> restart;
> soln:=solve({Vx=A1*(Va-Vb),
(Vin-Va)/R5 + (Vo-Va)/R6=0,
(Vz-Vb)/R4 + (Vx-Vb)/R3=0,Vy=A2*Vm,
(Vx-Vm)/R1+(Vy-Vm)*C1*s=0,Vz=A3*Vn,
(Vy-Vn)/R2+(Vz-Vn)*C2*s=0,
(Vz-Vp)*Ca*s^alpha+(Vo-Vp)/Ra=0,
Vo=A4*Vp},{Vin,Vo,Va,Vb,Vx,Vy,Vz,Vm,Vn,Vp}):Node analysis for the circuit
>
> assign(soln):R3:=c*R4:R5:=d*R6:C1:=tau1/R1:C2:=tau2/R2:Ca:=tau/Ra:
> Hs1:=Vo/Vin:Hs1:=collect(Hs1,s):
> Hsideal:=limit(Hs1,A1=infinity):
Hsideal:=limit(Hsideal,A2=infinity):Hsideal:=limit(Hsideal,A3=infinity):Hsi
> Hsideal:=- (tau*(1+c)*s^alpha)/(tau1*tau2*(1+d)*s^2+d*tau[alpha]*(1+c)*s^al
pha+c*(d+1));The ideal transfer function

$$H_{sideal} := - \frac{\tau(c+1)s^\alpha}{\tau_1 \tau_2 (1+d)s^2 + d\tau_\alpha (c+1)s^\alpha + c(1+d)}$$

> A1:=wt/s:A2:=wt/s:A3:=wt/s:A4:=wt/s:
>
> Hsn1:=algsubs(c=b*tau1*tau2,Hsn):Hsn1:=algsubs(d=a*tau1*tau2/(tau+tau1*tau
2*(b*tau-a)),Hsn1):The non-ideal transfer function
>

$$H_{sn1} := \left( \frac{(\tau + \tau_1 \tau_2 b \tau - \tau_1 \tau_2 a) s^\alpha \omega^4}{-s^{(\alpha+4)} \tau \tau_1^2 \omega \tau_2} \right) / \left( -s^{(\alpha+4)} \tau \tau_2^2 \omega \tau_1 b \tau_1 + \tau_1^2 \tau_2^2 s^{(\alpha+4)} \tau \omega^2 b \right. \\
- s^{(\alpha+4)} \tau \tau_1^2 \omega \tau_2 \\
+ (1 - \omega \tau_1 \tau_2 - \tau_1 \omega \tau_1 - 2 \tau_1^2 \omega \tau_2 b \tau_2 - 2 \omega \tau_1 \tau_2^2 b \tau_1 + b \tau_1 \tau_2 + 3 \tau_1^2 \tau_2^2 \omega \tau_2 b) s^4 + (\omega \tau_1^2 \\
\tau_1^2 b \tau_2 - \omega \tau_1^2 \tau_1 + 2 \tau_1 \tau_2 \omega \tau_1^3 - \omega \tau_1^2 \tau_2 - \omega \tau_1 b \tau_1 \tau_2 + \omega \tau_1^2 \tau_2^2 b \tau_1 - \tau_1^2 \tau_2^2 \omega \tau_1^3 b) s^3 \\
- \omega \tau_1^4 b \tau_1 \tau_2 + (\tau_2 - 2 \tau_1 \tau_2 \omega \tau_1 + \tau_2^2 b \tau_1 + \tau_1^2 b \tau_2 - 3 \tau_1^2 \tau_2^2 \omega \tau_1 b + \tau_1) s^5 \\
- \omega \tau_1^4 s^\alpha \tau_1 \tau_2 a + \tau s^{(\alpha+4)} + (\tau_1^2 \tau_2^2 b + \tau_1 \tau_2) s^6 + s^{(5+\alpha)} \tau \tau_2^2 b \tau_1 \\
+ \tau s^{(\alpha+1)} \omega \tau_1^3 b \tau_1 \tau_2 + s^{(5+\alpha)} \tau \tau_1^2 b \tau_2 - 2 \tau_1^2 \tau_2^2 s^{(5+\alpha)} \tau \omega \tau_1 b + \tau s^{(\alpha+4)} b \tau_1 \tau_2 \\
+ \tau_1^2 \tau_2^2 s^{(6+\alpha)} \tau b - s^{(3+\alpha)} \tau \omega \tau_1^2 \tau_1 - s^{(3+\alpha)} \tau \omega \tau_1^2 \tau_2 - \tau_1 \tau_2 s^{(\alpha+4)} \tau \omega \tau_1^2 \\
+ \omega \tau_1^3 s b \tau_1 \tau_2 + \tau_1 \tau_2 s^{(6+\alpha)} \tau - \tau_1 \tau_2^2 s^{(5+\alpha)} \tau \omega \tau_1 \\
+ (-\tau_1 \tau_2 \omega \tau_1^4 + \omega \tau_1^3 \tau_1 + \omega \tau_1^3 \tau_2 - \omega \tau_1^2) s^2 + \tau_1 \tau_2 s^{(3+\alpha)} \tau \omega \tau_1^3 + s^{(5+\alpha)} \tau \tau_1 \\
+ s^{(5+\alpha)} \tau \tau_2 + \tau s^{(3+\alpha)} \omega \tau_1 \left. \right)$$

>

```

Figure D.1: The non-ideal transfer function of Type I MAB based circuit of Figure 2.18(b).

## APPENDIX E

### Non-ideal Transfer Function of Type I Inductor-based Circuit

The non-ideal transfer function for the Type I inductor-based asymmetric-slope band-pass filter of Figure 2.20 is of order  $s^5$  in the integer terms and  $s^{5+\alpha}$  in the fractal terms as shown in Figure E.1.

```

> restart;
> soln:=solve({
  (Vin-Vx)*C2*s+(Vy-Vx)/R=0,
  Vy=A*(Vx-Vz),
  (Vp-Vz)/R1+(Vy-Vz)*C1*s=0,
  Vp=A*(Vx-Vm),
  (Vn-Vm)/R3+(Vp-Vm)/R2=0,
  Va=A*(Vo-Vn),
  (Va-Vb)/R1+(Vd-Vb)*C1*s=0,
  Vd=A*(Vo-Vb),
  (Vm-Vn)/R3+(Va-Vn)/R2=0,
  (Vo-Vd)/R+Vo*Ca*s^alpha=0}, {Vin, Vx, Vy, Vz, Vp, Vm, Vn, Va, Vb, Vd, Vo}):Node analysis
for the circuit
> assign(soln):
> Hs:=Vo/Vin:
> Hs1:=collect(Hs,s):A:=wt/s:C2:=c/R:R1:=tau1/C1:R3:=tau3*R2:Ca:=C2*d/c:Hs1:
=collect(Hs1,s):
> Hsn:=simplify(Hs1):
> Hsn1:=algsubs(d=1/tau1/tau3/a,Hsn):
> Hsn1:=algsubs(c=1/tau1/tau3/b,Hsn1):Hsn1:=simplify(Hsn1):Hsn1:=collect(Hsn
1,s);The non-ideal transfer function of the circuit
Hsn1 := (wt^3 s^alpha tau1 tau3 a) / ((tau3^2 tau1 a + 2 tau1 tau3 a + 2 tau1^2 tau3^2 wt a + 2 tau1^2 wt tau3 a + tau1^3 tau3^3 a b
+ 2 tau1^3 tau3^2 a b) s^4 + (2 tau1^2 tau3 a + tau1^2 tau3^2 a) s^5 + wt s^(2+alpha) tau3^2 tau1 b
+ 3 tau1 tau3 wt^2 s^(alpha+3) + 2 s^(4+alpha) + (wt^3 tau1 tau3 a + 2 wt^2 tau1^2 tau3^2 a b) s
+ (tau1^3 tau3^3 wt a b + tau3^3 tau1^2 a b + 2 tau1^2 tau3^2 a b + tau1^2 tau3^2 wt^2 a + tau3^2 wt tau1 a) s^3
+ wt^3 s^alpha tau1 tau3 b + 2 tau1 s^(5+alpha) + s^(4+alpha) tau3 + 2 wt s^(alpha+3) + wt^3 s^(2+alpha) tau3 tau1
+ 3 s^(4+alpha) tau3 tau1 wt + 2 s^(4+alpha) tau1^2 tau3 b + tau3^2 s^(alpha+3) tau1 b + 2 s^(alpha+3) tau1 tau3 b
+ s^(4+alpha) tau1^2 tau3^2 b + tau1 s^(5+alpha) tau3 + 4 s^(4+alpha) tau1 wt + 2 wt^2 tau1 s^(alpha+3) + 2 tau3 wt s^(alpha+3)
+ wt^2 s^(2+alpha) tau3 - 2 wt s^2 tau1^2 tau3^2 a b + 2 tau1^2 wt s^(alpha+3) tau3 b + wt^2 s^(2+alpha) tau3^2 tau1^2 b
+ 2 tau3^2 wt tau1^2 s^(alpha+3) b)

```

Figure E.1: The non-ideal transfer function of Type I Inductor based circuit of Figure 2.20.

## APPENDIX F

### Non-ideal Transfer Function of Type II MAB-based Circuit

The non-ideal transfer function for the Type II MAB-based asymmetric-slope band-pass filter of Figure 2.22(b) is of order  $s^6$  in the integer terms and  $s^{6+\alpha}$  in the fractal terms as shown in Figure F.1.

```

> restart;
> soln:=solve({Vx=A1*(Vin-Vb),
(Vo-Vb)/R4+(Vz-Vb)/R5+(Vx-Vb)/R3=0,
Vy=-A2*Vm,
(Vx-Vm)/R1+(Vy-Vm)*C1*s=0,
Vz=-A3*Vn,
(Vy-Vn)/R2+(Vz-Vn)*C2*s=0,
Vo=-A4*Vp,
(Vy-Vp)*Ca*s^alpha+(Vo-Vp)/Ra=0},{Vin,Vo,Va,Vb,Vx,Vy,Vz,Vm,Vn,Vp}):
> assign(soln):R3:=c*R4;R4:=d*R5/c:C1:=tau1/R1:C2:=tau2/R2:Ca:=tau/Ra:
> Hs1:=Vo/Vin:
> Hsideal:=limit(Hs1,A1=infinity):Hsideal:=limit(Hsideal,A2=infinity):Hsidea
l:=limit(Hsideal,A3=infinity):Hsideal:=limit(Hsideal,A4=infinity):
> Hsideal:=collect(Hsideal,s);The ideal transfer function

$$H_{sideal} := \frac{(\tau s^\alpha \tau_2 c + \tau s^\alpha d \tau_2 + \tau s^\alpha \tau_2) s}{\tau_1 \tau_2 s^2 + \tau s^\alpha \tau_2 c s + d}$$

> A1:=wt/s:A2:=wt/s:A3:=wt/s:A4:=wt/s:
> Hsn1:=algsubs(d=b*tau1*tau2,Hsn):Hsn1:=algsubs(c=a*tau1/tau,Hsn1):
> Hsn1:=collect(Hsn1,s);The non-ideal transfer function

$$H_{sn1} := \frac{((1 + \tau_2 \omega \tau + \tau_2 s) \omega^3 \tau s^{(\alpha+1)} (\tau_1 \tau + b \tau_1 \tau_2 \tau + \tau)) / ((\tau_1^2 \tau_2^2 b \tau + \tau_1 \tau_2 \tau + \tau_1^2 \tau_2 a) s^6 + \omega \tau^2 s^{(3+\alpha)} + (\tau_1^2 a + \tau_1^2 b \tau_2 \tau + \tau_2 \tau + 4 \tau_1 \tau_2 \omega \tau + \tau_2^2 a \tau_1 + 3 \tau_1^2 \tau_2^2 \omega b \tau + \tau_2^2 b \tau_1 \tau + 3 \tau_1^2 \tau_2 \omega a + \tau_1 \tau) s^5 + (\omega \tau^2 \tau + \omega \tau^3 \tau_2 \tau + \omega \tau^4 \tau_1 \tau_2 \tau + \omega \tau^3 \tau_1 \tau) s^2 + \tau_1^2 \tau_2^2 s^{(6+\alpha)} \tau^2 b + \tau_1^2 \tau_2^2 s^{(\alpha+4)} \omega \tau^2 b + (3 \tau_1^2 \tau_2 \omega \tau^2 a + \tau + 2 \tau_2^2 \omega b \tau_1 \tau + 3 \tau_2^2 \omega \tau + 3 \tau_1^2 \tau_2^2 \omega b \tau + 2 \tau_1^2 \omega b \tau_2 \tau + b \tau_1 \tau_2 \tau + 3 \tau_1 \omega \tau + 2 \tau_2 \omega a \tau_1 + 2 \tau_1^2 \omega a + a \tau_1 + 6 \tau_1 \tau_2 \omega \tau^2) s^4 + (\tau_2 \omega \tau^2 a \tau_1 + \omega b \tau_1 \tau_2 \tau + 2 \omega \tau + \tau_1^2 \omega \tau^2 a + \tau_1^2 \omega \tau^2 b \tau_2 \tau + 3 \tau_1 \omega \tau^2 \tau + \omega a \tau_1 + \tau_2^2 \omega \tau^2 b \tau_1 \tau + \tau_1^2 \tau_2^2 \omega \tau^3 b \tau + 3 \tau_2 \omega \tau^2 \tau + \tau_1^2 \tau_2 \omega \tau^3 a + 4 \tau_1 \tau_2 \omega \tau^3 \tau) s^3 + \omega \tau^2 \tau_1 \tau^2 s^{(3+\alpha)} + \tau_1^2 \omega \tau^2 s^{(\alpha+4)} b \tau_2 + 2 \tau_1^2 \tau_2^2 s^{(\alpha+5)} \omega \tau^2 b + \tau^2 s^{(\alpha+4)} b \tau_1 \tau_2 + \tau_1^2 \tau^2 s^{(\alpha+5)} b \tau_2 + \tau_2^2 \tau^2 s^{(\alpha+5)} b \tau_1 + \omega \tau^3 \tau^2 s^{(\alpha+1)} b \tau_1 \tau_2 + \tau_2^2 \omega \tau^2 s^{(\alpha+4)} b \tau_1 + \tau_1 \tau_2 s^{(3+\alpha)} \omega \tau^3 \tau^2 + 3 \tau_1 \tau_2 s^{(\alpha+4)} \omega \tau^2 \tau^2 + 3 \tau_1 \tau_2 s^{(\alpha+5)} \omega \tau^2 + 2 \tau_1^2 \tau_2 s^{(\alpha+5)} \omega \tau a \tau + \tau_1^2 \tau_2 s^{(\alpha+4)} \omega \tau^2 a \tau + \omega \tau^3 s^{(\alpha+2)} \tau_2 a \tau_1 \tau + \tau_2 \omega \tau s^{(\alpha+4)} a \tau_1 \tau + \omega \tau^3 s^{(\alpha+1)} a \tau_1 \tau + \tau_2 s^{(\alpha+5)} a \tau_1 \tau + \tau_1^2 \tau_2 s^{(6+\alpha)} a \tau + \tau_1^2 \omega \tau s^{(\alpha+4)} a \tau + \tau_1 \tau^2 s^{(\alpha+5)} + \tau_2 \tau^2 s^{(\alpha+5)} + \omega \tau^4 b \tau_1 \tau_2 \tau + \omega \tau^3 s b \tau_1 \tau_2 \tau + s^{(\alpha+1)} \omega \tau^4 \tau_2 a \tau_1 \tau + \tau^2 s^{(\alpha+4)} + \omega \tau^2 \tau_2 \tau^2 s^{(3+\alpha)} + \tau_1 \tau_2 s^{(6+\alpha)} \tau^2 + 2 \tau_2 \omega \tau^2 s^{(\alpha+4)} + 2 \tau_1 \omega \tau^2 s^{(\alpha+4)} + \tau_1^2 s^{(\alpha+5)} a \tau + s^{(\alpha+4)} a \tau_1 \tau)$$


```

Figure F.1: The non-ideal transfer function of Type II MAB based circuit of Figure 2.22(b).